

Combined thermochemical energy storage and heat transformation for industrial waste heat recovery

Von der Fakultät für Energie-, Verfahrens- und Biotechnik der Universität Stuttgart zur Erlangung der Würde einer Doktor-Ingenieurin (Dr.-Ing.) genehmigte Abhandlung

Vorgelegt von

Jana Stengler

aus

Hameln

Hauptberichter: Prof. Dr. rer. nat. habil. André Thess

Mitberichter: Prof. Dr. rer. nat. habil. Burak Atakan

Tag der mündlichen Prüfung: 26. November 2020

Institut für Gebäudeenergetik, Thermotechnik und Energiespeicherung (IGTE)

2021

Contents

Nomenclature	5
Kurzfassung	7
Abstract	9
1 Introduction	11
1.1 Technology overview	13
1.1.1 Thermal energy storage	13
1.1.2 Chemical heat pumps and thermochemical heat transformation	16
1.1.3 Steam-based reaction systems	21
1.1.4 Packed-bed storage reactor designs	23
1.2 Research objectives	25
1.3 Methods	27
1.3.1 Experimental material characterization	27
1.3.2 Experimental proof-of-concept	28
1.3.3 Numerical analysis of the potential and the limitations of the storage design	29
2 Publications	31
2.1 Paper I: Pre-study	34
2.2 Paper II: Proof-of-concept	46
2.3 Paper III: Material characterization	60
2.4 Paper IV: Performance analysis	74

Contents

3 Discussion and Conclusions	93
3.1 Discussion	93
3.2 Application scenarios	97
3.2.1 TES without effective temperature gradient	98
3.2.2 TES combined with a thermal upgrade	99
3.2.3 Operation as high-temperature heat pump	101
4 Summary	103
Bibliography	107

Nomenclature

Greek letters

α	heat transfer coefficient, W/(m ² K)
ϵ	coefficient of performance
η	efficiency

Latin letters

$\Delta_C H$	standard molar enthalpy of condensation, kJ/mol
$\Delta_E H$	standard molar enthalpy of evaporation, kJ/mol
$\Delta_R H$	standard molar enthalpy of reaction, kJ/mol
p	pressure, Pa
p^+	reference pressure, Pa
T	absolute temperature, K
Q	thermal energy, J
W	work, J

Indices

en	energetic
ex	exergetic
g	gas
l	liquid
s	solid

Nomenclature

Abbreviations

CHP	chemical heat pump
DLR	Deutsches Zentrum für Luft- und Raumfahrt e.V.
FEM	finite element method
HE	heat engine
HP	heat pump
HT	heat transformation
PCM	phase change material
TES	thermal energy storage
TGA	thermogravimetric analysis

Kurzfassung

Thermische Energie ist nicht gleich thermische Energie: Insbesondere das Temperaturniveau, auf dem beispielsweise Abwärme aus industriellen Prozessen zur Verfügung steht, entscheidet darüber, ob diese Energie direkt als Prozessenergie reintegriert werden kann oder ungenutzt an die Umgebung abgegeben wird. Eine weitere Einschränkung ist die zeitliche Kopplung zwischen Wärmeangebot und Wärmenachfrage. Diese kann über den Einsatz thermischer Energiespeicher aufgelöst werden, wobei jedoch der Speichervorgang die thermische Energie in Bezug auf ihr Temperaturniveau abwertet und so zu Exergieverlusten führt.

Im Rahmen dieser Arbeit wurde ein thermochemischer Energiespeicher entwickelt, der auf der umkehrbaren chemischen Reaktion von Strontiumbromid-Anhydrat zu Strontiumbromid-Monohydrat beruht. Die Phasenumwandlung zwischen An- und Monohydrat ermöglicht einen Speicherbetrieb im Temperaturbereich von etwa 150 °C bis ca. 300 °C, der insbesondere für die Nutzung industrieller Abwärme interessant ist. Dabei kann die Temperaturabwertung zwischen Beladung und Entladung mittels der sogenannten „thermochemischen Wärmetransformation“ kompensiert werden: Hebt man den Gasdruck zwischen Beladung und Entladung des Speichers an, so wird die thermische Energie bei höherer Temperatur freigesetzt als sie zuvor eingekoppelt wurde. Thermodynamisch entspricht dieses System der Kopplung eines Energiespeichers mit einer thermisch betriebenen Wärmepumpe.

Für das thermochemische Reaktionssystem $\text{SrBr}_2/\text{H}_2\text{O}$ wurden die druckabhängigen Reaktionstemperaturen der Hydratations- und Dehydratationsreaktion experimentell untersucht sowie aus thermogravimetrischen Messungen eine empirische Beschreibung der Reaktionsrate abgeleitet. Der experimentelle

Kurzfassung

Funktionsnachweis der Wärmetransformation wurde im Temperaturbereich von 180 °C (Beladetemperatur bei 1 kPa Wasserdampfdruck) und 280 °C (Entladetemperatur bei 560 kPa Wasserdampfdruck) im 1 kW-Maßstab mit einem skalierbar entwickelten Reaktorkonzept erbracht.

Die Betriebscharakteristik des Speichermoduls wurde experimentell und numerisch analysiert, um die Vorgänge im Reaktor auch quantitativ zu erklären: Mittels einer experimentell validierten Simulationsstudie wurde zunächst die maßgebliche Limitierung der thermischen Leistung des Speichers durch den Wärmedurchgang nachgewiesen. Anschließend wurde mittels einer Sensitivitätsstudie gezeigt, dass zum Zeitpunkt der Maximalleistung der größte Beitrag an der Grenzfläche zwischen Feststoffschüttung und Wärmeübertragerwand entsteht – und nicht, wie vielfach für andere Festbettgeometrien angenommen, innerhalb der porösen Feststoffschüttung.

Die vorliegende Arbeit erbringt damit neben dem Funktionsnachweis für das thermochemische Referenzsystem die notwendigen Grundlagen für detaillierte Potentialanalysen verschiedener industrieller Speicher- und Wärmetransformationsanwendungen sowie die Optimierung der Speicherintegration.

Abstract

To quantify the value of thermal energy as an “energy currency”, it needs more than solely the energy’s amount given in Joules: the temperature level at which, for example, excess heat is available from industrial processes determines whether this thermal energy can directly be re-integrated as process heat or is emitted to the ambient as waste heat. A further limitation is the temporal coupling of heat supply and heat demand. The latter can be resolved by using thermal energy storage systems, which, however, further “downgrade” the thermal energy in terms of its temperature level, and hence, lead to exergy losses. In this thesis, a thermochemical energy storage system was developed based on the reversible chemical reaction of strontium bromide anhydrate to strontium bromide monohydrate. The phase transition from the anhydrous to the monohydrated phase allows for storage operation in the temperature range from 150 °C to 300 °C, which is particularly interesting for industrial applications. The temperature downgrade between charging and discharging can be compensated by means of the so-called “thermochemical heat transformation”: if the gas pressure is raised between charging and discharging, the stored thermal energy is released at a higher temperature compared to its transfer to the storage. Thermodynamically, this system corresponds to the coupling of an energy storage with a thermally driven heat pump.

For the thermochemical reaction system $\text{SrBr}_2/\text{H}_2\text{O}$, the pressure-dependent reaction temperatures of the hydration and dehydration reaction were experimentally investigated, and an empirical description of the reaction rate was derived from thermogravimetric measurements. The experimental proof-of-concept was performed with an effective thermal upgrade from 180 °C (charging temperature

Abstract

at 1 kPa steam pressure) to 280 °C (discharging temperature at 560 kPa steam pressure), using a reactor concept scalable for large industrial applications. The operating characteristics of the storage module were experimentally and numerically studied to quantitatively explain the performance-dominating processes in the storage reactor. By means of the experimentally validated simulation study, the limitation of the storage module's thermal performance by heat transfer was proven. Subsequently, a thermal sensitivity study was executed, which shows that at the moment of maximum thermal power, the major contribution is attributed to the interface between the porous bulk and the heat exchanger wall - and not, as it is often assumed for other packed-bed storage geometries, within the porous medium.

In addition to the proof-of-concept, the present study provides the necessary fundamentals for detailed potential analyses of various industrial thermal energy storage and heat transformation applications and the optimization of the storage integration.

1

Chapter 1

Introduction

Even in most optimistic future energy scenarios, where energy is generated solely from unlimited renewable resources such as solar and wind energy, the supply with energy – electrical energy or thermal energy – will not be free of effort and cost. Hence, reasonable and cost-efficient energy usage, process intensification and waste heat recovery will remain subjects for optimization in the industrial and the private sectors. This will even more be the case during the transition phase towards the above-mentioned scenario, with fossil energy sources still playing a substantial role. Given this background, the present thesis is dedicated to the development of a thermal energy storage (TES) in the temperature range from 150 °C to 300 °C, which allows for an additional thermal upgrade of the stored energy by up to 100 K. Its operation principle is based on a gas-solid reaction between strontium bromide and water vapor as thermochemical working pair. By using waste heat for steam supply, the storage system can be applied to increase energy efficiency in industrial processes.

To date, 50% of the global final energy consumption covers the supply with thermal energy for industrial processes, space and water heating in buildings, and agriculture [1]. Although currently heat is the number one energy end-use, in future energy scenarios, electrical energy is expected to play an increasingly important role on both the source and sink side due to intensified power genera-

1 Introduction

tion from renewables [1]. Despite the predicted trend towards electricity-based energy networks, there are many cases where energy is needed in the form of process heat, and, at the same time, excess energy is released in form of waste heat. In these cases, electrical energy storage might be a too costly option for increased energy efficiency via energy storage. Such scenarios, which can be identified e.g. in pulp and paper industries and chemical process industries, illustrate the potential of TES as an energy and cost-saving option for increasing energy efficiency. To date, there is substantial room for improvement: in the European Union member states alone, approximately 100 TWh of waste heat in the temperature range from 100 °C to 200 °C are emitted to the environment every year [2]. Yet, this is only a third of the total industrial waste heat potential: in the temperature level from 200 °C to 500 °C, industrial processes emit about 78 TWh per year, and 124 TWh per year at temperatures higher than 500 °C. Summed up over the whole relevant temperature range, the amount of industrial waste heat corresponds to 16.7% of the total industrial energy consumption for the supply of process heat, or 9.5% of the total industrial energy consumption [2].

At the same time, thermal energy storage presents an extra challenge compared to electrical energy storage: In contrast to electrical energy, the value of thermal energy is not only defined by its amount (e.g., given in kWh), but also by its “exergetic quality”, namely, by its temperature level. Therefore, when storing thermal energy e.g. in sensible or latent TES, we face the following situation: due to at least two necessary heat transfer steps, i.e. charging and discharging, the temperature of the heat discharged from the TES will inevitably be lower than the charging temperature – dissipation to the surroundings due to insufficient insulation etc. not even considered. Hence, the discharged thermal energy loses in exergetic value (temperature level), and therefore also in terms of its economic value. TES will therefore only be an economically reasonable option in cases where the discharge temperature is not too low for direct re-integration. A way for implementing a TES with no or even positive temperature differences between the charging and the discharging temperature is provided by

thermochemical energy storage, where thermal energy is stored in the form of the reaction enthalpy of a reversible reaction, e.g. of a gas-solid-reaction. The concentration of the gas determines the reaction temperature, and hereby allows for varying the charging and discharging temperatures of the TES.

Concluding from these considerations, the objective of this work is the development of a thermochemical energy storage which allows a maximum of flexibility in terms of its temperature operation range for charging and discharging, and hence, an optimal “thermal upgrade” range. In view of later industrial applications, where steam is a common heat transfer fluid and also waste heat carrier, a steam-based thermochemical reaction system is chosen for keeping the option of direct steam utilization.

1.1 Technology overview

In the following, the state-of-the-art of different technological aspects of this thesis will be given. This includes fundamentals on the different TES technologies, the thermodynamics of thermochemical heat transformation and chemical heat pumps, and a literature review of steam-based thermochemical reaction systems and corresponding storage designs. Based on this technology overview, the specific research objectives of this thesis will be deduced in Section 1.2. Finally, the introducing chapter will be concluded by a discussion on the experimental and numerical methods used within the present work in Section 1.3.

1.1.1 Thermal energy storage

From the three basic technologies for TES, sensible, latent and thermochemical TES, the first one is relatively simple to use and has been commonly utilized by mankind since the pre-industrial age (e.g., in the form of tiled stoves for heating). However, for certain industrial applications, the latter two technologies have several advantages, such as the possibility of charging and discharging at

1 Introduction

a constant temperature. In the case of latent TES, thermal energy is stored in form of the melting enthalpy of a phase change material (PCM). Not a physical, but a chemical phase change is the fundamental principal of thermochemical TES: thermal energy is stored in form of the reaction enthalpy of a reversible chemical reaction, hence, in the form of chemical potential. This way, latent and thermochemical TES allow for higher energy storage densities compared to sensible energy storage in fluids or solids [3], [4], [5].

One of the challenges in both of these technologies is the heat transfer in the solid phase, since solid salts as well as bulk phases of salt granules or powders typically feature thermal conductivities below $1 \text{ W}/(\text{m}\cdot\text{K})$ [6], [7]. A general target of optimized storage designs is to provide large specific powers without increasing the temperature gradient required to transfer thermal energy from the application to the TES and reverse. Thus, in order to achieve high exergetic efficiencies in the storage process, the storage's overall heat transfer coefficient needs to be maximized.

Starting with the storage material selection and optimization for both latent and thermochemical TES, there is significant research work done along these lines, namely, on the enhancement of the effective thermal conductivity of the solid phase [8], [9], [5]. Different approaches are discussed, e.g. the mixing with highly-conductive additives such as copper and graphite [10], [6], and the implementation of heat transfer structures such as foams or fins as highly conductive matrices [11], [12], [13]. Another approach to control the thermal power of the TES is pursued with active concepts, i.e. the transport of the storage material through a heat exchanger unit for discharging and charging. Different concepts are being investigated, such as rotating drum concepts [14] or batch-wise operation concepts [15] in the case of latent TES.

In the context of thermochemical energy storage, different moving bed reactors (e.g. high-temperature TES based on metal oxides [16] and calcium oxide [17], [18], low-temperature TES with strontium bromide hexahydrate [19]) and fluidized bed systems, e.g. for calcium oxide [20], are being investigated. These concepts uncouple the thermal power of the storage from its capacity, and hence,

1.1 Technology overview

allow for constant powers during charging and discharging. However, their operation requires additional auxiliary energy. For both, latent and thermochemical TES, the above-mentioned active concepts are still in the stage of development.

Compared to latent TES, thermochemical TES adds some additional complexity to the storage design and process integration since it involves two reacting phases, e.g. a gas and a solid phase. Therefore, not only heat transfer aspects have to be addressed during the design of the storages, but also the mass transfer of the fluid reactant to and from the solid reactive phase. In both latent and thermochemical TES, the temperature of the phase change is determined by the concentrations of the different components. In latent TES, the concentration of salts in binary or ternary salt mixtures defines the melting temperature and thus, the necessary charging temperature [3]. The same is true for thermochemical systems, but with one important difference: here, the concentration of the reactants can be adjusted during the charging, storing, and discharging phases. For example, in gas-solid reactions, the concentration of the gas can easily be varied by its pressure. Hence, the temperature of the chemical phase change – the equilibrium temperature of the reversible chemical reaction – can be controlled. Summing up, the higher complexity and (presumably) higher costs compared to sensible or latent TES might pay off in the case of thermochemical TES, if the feature of controlling the reactants' concentrations can be used in a way that allows for higher energy efficiency. This efficiency gain may be driven by the flexibility in terms of the temperature operation range of the storage, and/or the option of discharging the storage at higher temperatures compared to charging, which in the present work is referred to as thermochemical heat transformation or thermal upgrade. It allows compensating for the temperature gradient needed to transfer thermal energy to and from the TES, and hence, enables increased exergy efficiencies.

In Fig. 1.1, the schematic operation principle of the thermochemical TES and heat transformer is illustrated using the example of steam-based reaction systems: in the charging phase (a), thermal energy is transferred to the hydrated solid material, which decomposes into the dry solid and the gas. The gas is

1 Introduction

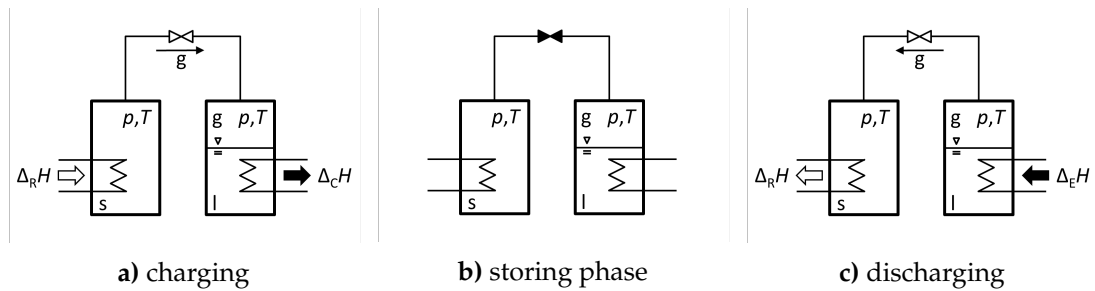


Figure 1.1: Operation principle of the thermochemical energy storage and heat transformer. Here, a gas-solid reaction with condensable gas (e.g. steam or ammonia) is chosen as thermochemical system. Note that during the storing phase (b, valve closed), the temperature and pressure set points can be adjusted so that the subsequent discharge process runs at different conditions compared to the charging process.

condensed in the second vessel, with the system pressure being controlled by the condenser temperature. The valve connecting the two vessels is closed in the storing phase (b), and, accordingly, pressures and temperatures in the systems can be changed independently. To start the discharging phase, thermal energy is introduced into the evaporator, with the evaporator temperature hence determining the overall system pressure as soon as the valve between the two vessels is opened. The exothermic reaction starts with the solid taking up the gas, and the reaction enthalpy is discharged from the TES.

1.1.2 Chemical heat pumps and thermochemical heat transformation

Basically, heat transformation processes can be thermodynamically described as a coupled heat engine and heat pump process. Within the literature, some authors distinguish between “synproportionation” processes, such as heat pumps, and “disproportionation” processes, referring to the above-mentioned heat transformation [21], [22]. Within the latter, different types of processes can be distinguished with regard to the number of temperature levels and number of

1.1 Technology overview

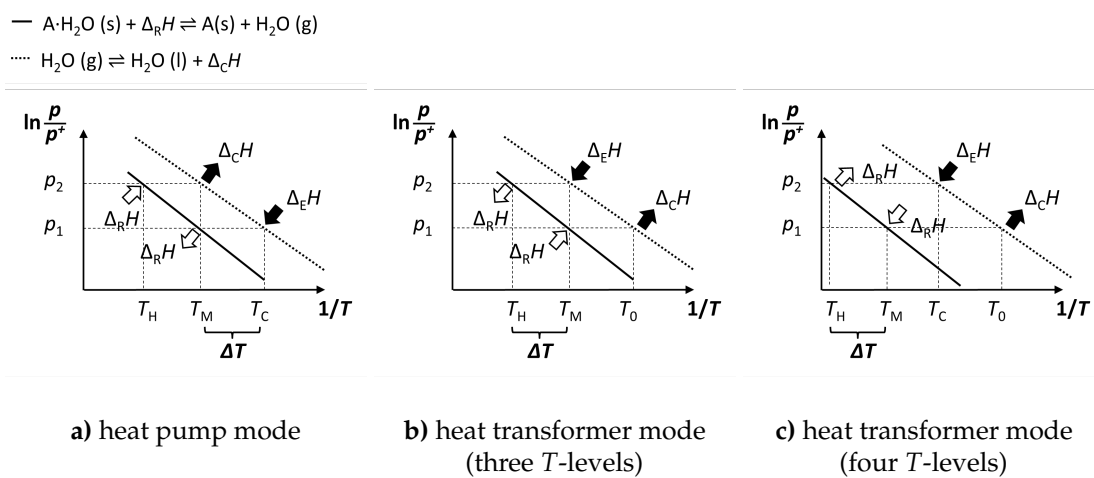


Figure 1.2: Classification of chemical heat pump and heat transformation processes, with ΔT indicating the process-specific thermal upgrade. a) Thermally driven chemical heat pump (CHP) for the thermal upgrade of low-temperature waste heat. In contrast to the heat transformation processes, here, a high-temperature heat source is required. b) Heat transformation (HT): thermal upgrade of low-temperature waste heat. For instance, the operation of this 3-level heat transformation process was demonstrated by Richter et al. based on calcium chloride dihydrate [24]. c) Heat transformation: thermal upgrade of high-temperature process heat, driven by low-temperature waste heat. This 4-level process is the operation mode of the present work, since the equilibrium lines of the chosen gas-solid reaction and the vapor-liquid equilibrium of water lie further apart.

gas-solid working pairs [23]. The classification used in the present work is described in Fig.1.2, which illustrates how a thermally driven chemical heat pump (CHP) or heat transformation (HT) processes could be operated via a gas-solid reaction. Here, the gaseous reactant is specified to steam, with the vapor-liquid equilibrium being displayed in the Van't Hoff diagram, see Fig.1.2 (also referred to as Clapeyron diagram [23]).

While Fig. 1.2a depicts the chemical heat pump mode, Fig. 1.2b and c illustrate heat transformation processes with three and four temperature levels, respectively. In the chemical heat mode, the heat pump (HP) transfers thermal energy from a reservoir of low temperature T_C to a heat sink of medium temperature

1 Introduction

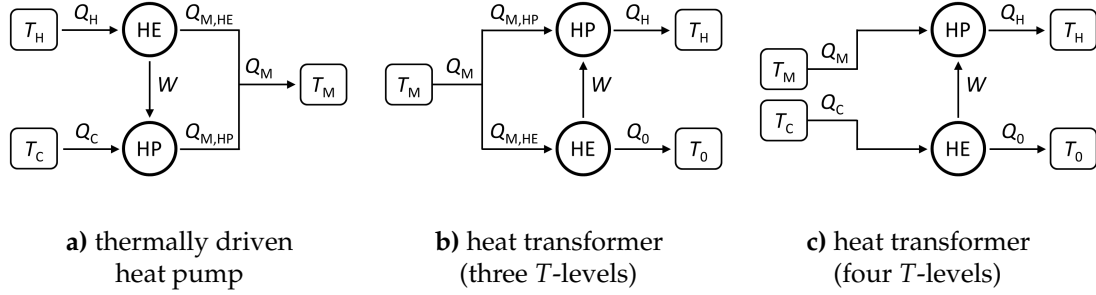


Figure 1.3: Definition the chemical heat pump and heat transformation processes based on the heat pump and heat engine Carnot cycles.

T_M . The required technical work is supplied from the heat engine (HE) operating between the reservoir at high temperature T_H and the medium temperature heat sink T_M . In the heat transformation process with three temperature levels (Fig. 1.2b), the HE operates between the medium temperature reservoir T_M and the ambient T_0 , with the technical work driving the HP between T_M and T_H . In the four-level process (Fig. 1.2c), the HP operates at a higher absolute temperature level (T_M and T_H), compared to the HE (T_0 and T_C). Fig. 1.3 gives the thermodynamic description of the three different energy upgrade processes. Based on the respective combinations of the Carnot machines, the coefficient of performance of the chemical heat pump, ϵ_{CHP} , and the energy efficiency of the heat transformation process, η_{HT} , are derived from an energy balance:

$$\epsilon_{\text{CHP}} = \frac{Q_M}{Q_H} = 1 + (\epsilon - 1)\eta = \frac{1 - T_C/T_H}{1 - T_C/T_M} \quad (1.1)$$

$$\eta_{\text{HT}} = \frac{Q_H}{Q_M + Q_C} = \frac{\epsilon\eta}{1 + (\epsilon - 1)\eta} = \frac{1 - T_C/T_0}{T_M/T_H - T_C/T_0} \quad (1.2)$$

Here, η corresponds to the energy efficiency of the heat engine, and ϵ to the heat pump's coefficient of performance. Eq. (1.2) gives the efficiency of the four-level HT process. The efficiency of the three-level HT process can either be obtained from Eq. (1.2) with $T_C = T_M$, or from the reciprocal of Eq. (1.1).

1.1 Technology overview

The detailed evaluation of these different concepts with regard to their application-relevant efficiencies depends on their integration. For instance, to judge the cost-relevant energy efficiency of the heat transformation process, it needs to be clarified if the thermal energy needed for providing the gaseous reactant at higher pressures can be supplied for by waste heat, or demands additional heating effort.

However, e.g. due the occurrence of a thermal hysteresis between the endothermic and the exothermic reaction, real thermochemical systems suffer from entropy production, and thus, exergy losses. The entropy production in non-ideal systems, e.g. caused by the temperature gradients occurring due to the heat transfer steps required for charging and discharging a TES system, is accounted for in an exergy efficiency analysis. For instance, the exergy efficiency of the heat transformer is expressed by the ratio of exergy transformed by the process and the input exergy [25], [26]:

$$\eta_{\text{ex}} = \frac{Q_{\text{H}}(1 - T_0/T_{\text{H}})}{Q_{\text{M}}(1 - T_0/T_{\text{M}}) + Q_{\text{C}}(1 - T_0/T_{\text{C}})}. \quad (1.3)$$

In steam-based heat transformer systems, Q_{C} corresponds to the energy needed to supply steam as reactant in the chemical reaction at the steam pressure (or evaporation temperature T_{C} , respectively) needed for running the discharge reaction at the temperature T_{H} . Q_{M} is the thermal energy transferred to the TES during charging, and Q_{H} is the energy released during discharging the TES. For exemplary application scenarios, energy and exergy efficiencies of the developed combined TES and heat transformer will be given in Section 3.2.

While various literature studies describe the development of heat pumps based on gas-solid reactions (Fig. 1.2a) [23], [27], [28], fewer studies are published on the actual implementation of single or multi-step heat transformation processes (Fig. 1.2b and c, respectively). For instance, Willers et al. describe a two-stage heat transformer based on metal hydrides, which was operated with 130 – 135 °C heat source and 190 – 200 °C heat sink temperatures [29]. Note that due to the usage of three different metal alloys as reactive solids in their multi-stage experimental

1 Introduction

scheme, the corresponding van't Hoff diagram features three phase transitions, and is therefore more complex than displayed in Fig. 1.2b. The prototype was reported to operate with a maximum thermal upgrade of 70 K. A specific power output of 30 W/kg of metal hydride was demonstrated, with a total hydride mass of 210 kg distributed in six thermochemical reactors.

The operation of a single-stage heat transformer (Fig. 1.2b) based on ammonia salts between 150 °C and 200 °C is reported by Haije et. al [30]. The 1 kW prototype is assembled from six stacked units, each containing 1.8 kg of sorbent (lithium chloride or magnesium chloride, total weight of 12 kg per unit). Due to the safety regulations for the operation with pressurized ammonia (2 MPa), the total mass of the storage was about 100 kg, thus being a major drawback of the prototype [31]. However, in a techno-economic feasibility study, the economic potential of the ammonia/salt heat transformation process for waste heat recovery was described as promising [32].

Based on two ammonia salts and the vapor-liquid equilibrium of ammonia as a third phase transition, Wu et al. investigated a two-stage heat transformer process operating with four temperature levels (Fig. 6c, again multi-stage) [33]. Their prototype was operated in the range from 96 °C (condenser temperature 25 °C) to 161 °C (evaporator temperature 60 °C) with a maximum thermal upgrade by 65 K. The storage contained approximately 8 kg of strontium chloride and magnesium chloride. However, no information on the thermal power of the prototype is revealed.

At DLR, Richter et al. investigated a single-stage heat transformer (Fig. 1.2b) based on the hydration and dehydration reaction of calcium chloride [24]. A prototype was operated with an effective thermal upgrade from 130 °C charging temperature (2 kPa condenser pressure) to 165 °C discharging temperature (75 kPa evaporator pressure). The maximum thermal power achieved was approximately 450 W. The prototype contained 0.7 kg of calcium chloride dihydrate, hence, the specific thermal power of the storage design was significantly higher than in the other concepts mentioned above (peak: 640 W/kg hydrated salt).

Overall, the storage required approximately 1.5 h each for charging and discharging. Thus, the average thermal power based on the total storage capacity was 100 W or 140 W/kg hydrated salt.

As it can be seen from the examples above, it is quite challenging to achieve effective thermal upgrades of several tens of Kelvins, often requiring multi-stage concepts or the use of large pressure differences. A remarkably large temperature lift from 80 °C to 170 °C was achieved by Lubis et al. with a two-stage absorption heat transformer operated with a lithium bromide-water solution [34]. However, for the targeted application range of the present work (150 °C – 300 °C), there is no demonstration of a heat transformer reported in literature to the author's knowledge.

1.1.3 Steam-based reaction systems

Regarding the later integration into applications, choosing steam as gaseous reactant in the thermochemical working pair has advantages due to its common usage in the industrial sector. Other common gaseous reactants are ammonia, hydrogen, oxygen, but also carbon dioxide [23]. A lot of research on steam-based reaction system has been done in the context of low-temperature energy storage, e.g. for seasonal storage applications for residential buildings [35]. Some of the discussed salts form more than one hydrate phase, with the different hydrate levels appearing in different pressure and temperature ranges. One example of such a salt is strontium bromide, which forms a hexahydrate at temperatures below approximately 70 °C, and a monohydrate phase, which decomposes into the anhydrous salt and steam at temperatures of around 150 °C [36], [37]. The reversible reaction from the monohydrate to the hexahydrate salt is investigated for low-temperature TES in open storage concepts, i.e. storages operated with humid air open towards the environment [38], [39].

For the targeted temperature range of 150 °C to 300 °C, few steam-based reaction systems are described in literature [40], [41], [42]. One basic criterion for the material selection for TES and heat transformation applications is the reversibility

1 Introduction

of the chemical reaction in terms of a thermal hysteresis between the endothermic and the exothermic reaction [43]. The occurrence of a thermal hysteresis is reported for salt hydrate reactions at low temperatures [44], [45], but also e.g. for metal oxides at reaction temperatures above 600 °C [46]. With regard to its implications for the TES application, a thermal hysteresis occurring in a thermochemical reaction system is comparable to subcooling effects in PCM [47], [48]. If the thermal hysteresis between the endothermic and the exothermic reaction is large, e.g. 50 K or more, it may be impossible to achieve an effective thermal upgrade. In this case, a large fraction of the available pressure difference is already required to reach even the same reaction temperatures for charging and discharging, or, more extremely, the necessary charging temperatures exceed the desired discharge temperatures. For instance, magnesium oxide was excluded due to the large thermal hysteresis appearing between the hydration of the oxide and the dehydration of the hydroxide. Although magnesium oxide is a potential candidate for thermochemical TES and for the operation of a chemical heat pump, the thermal hysteresis inhibits its feasibility for thermochemical heat transformation [49].

Another material selection criterion is cycle stability. For instance, the hydration of calcium sulfate to its hemihydrate and the dehydration of the latter were reported to be subject to significant degradation within the first ten reaction cycles [42].

These considerations have led to the selection of $\text{SrBr}_2/\text{SrBr}_2 \cdot \text{H}_2\text{O}$ as reference reaction system in the present work. The salt showed promising properties in an experimental screening based on thermogravimetric analysis measurements [42]. Two major disadvantages are associated with the usage of strontium bromide as thermochemical TES material: firstly, the corrosiveness to steel, in particular in very humid atmosphere close to the dissolution of the salt [50], and, secondly, high prices of approximately 50 USD per kg [51]. This is mainly related to the very low worldwide production of approximately 300 kg SrBr_2 hexahydrate per year. However, it is expected that costs decrease to approximately 3.55 USD per kg for the synthesis of strontium bromide from strontium carbonate [51].

1.1 Technology overview

Similarly, in the context of low-grade heat recovery applications, an analysis on the cost-reduction potential in simplified production process resulted in a cost estimation of 700 – 2,100 € per ton of SrBr₂ [52].

In the later course of the present work, the organic salt calcium oxalate, CaC₂O₄, was reported to be a highly potential candidate for thermochemical TES and heat transformation [53]. Another promising candidate could be the mineral parascholzite, CaZn₂(PO₄)₂·2H₂O [54]. Both calcium oxalate and parascholzite can be operated in a very similar temperature and pressure range as strontium bromide.

Please note that sorption systems, such as zeolites, were excluded from the material screening. However, in principle, operating heat transformation processes is possible with zeolites, provided that highly temperature-stable sorbents are used, which at the same time are able to take up water at high temperatures and pressures, and do not require high regeneration temperatures. In this context, it also needs to be considered that zeolites are not characterized by a monovariant equilibrium, but instead, their phase diagram changes with the concentration of the absorbed substance in the sorbent [55]. Hence, the sorption enthalpy changes with the state of charging and discharging, respectively, which is not favorable for the targeted heat transformation process.

1.1.4 Packed-bed storage reactor designs

Concerning the operation of the gas-solid reaction in a storage reactor, there are various design concepts published for thermochemical TES based on salt hydrates. A basic distinction is made between open and closed systems [56], [57], e.g. the open [58] and closed [24] operation of a TES and heat transformer based on calcium chloride dihydrate. In this context, the terms open and closed refer to the gas atmosphere in the storage. Open steam-based reactor systems are characterized by the operation with mixed steam/air atmosphere, e.g. dry air from the environment for charging and humid exhaust air for discharging. In contrast, a thermochemical reactor system is defined as closed when no gas

1 Introduction

exchange with the atmosphere is enabled. In the case of steam-based reaction systems, the water emerging from the reacting bulk phase during charging is condensed in a separate vessel. Operating a thermochemical TES under vacuum conditions during charging and with overpressures during discharging allows for a larger effective thermal upgrade than compared to the open operation due to the higher gas concentration difference.

As in the present work, higher temperature levels are addressed compared to the above-mentioned studies on strontium bromide hexahydrate operated in open storage systems [39], [37], steam pressures need to be raised accordingly. Hence, closed storage concepts operated with pure steam are more eligible. Usually, packed-bed thermochemical reactors are designed as tube bundle heat exchangers, with the reactive material on tube side [24] or shell side [59], or plate heat exchangers [60], [61]. Finned-tube heat exchangers, such as they are widely investigated for latent TES [12], [62], [63], are less common in thermochemical storage concepts, although they are promising with regard to high specific thermal powers [4], [30], [64], [65], [66]. A general challenge in these designs is providing not only sufficient heat transfer, but also sufficient gas mass transfer to and into the porous bulk. This is increasingly important if the storage is operated under vacuum conditions in steam-based systems, since the steam density decreases with the pressure. Particularly during charging, this leads to higher steam velocities and pressure losses in the packed bed. With these multiple requirements, there is a lack of packed-bed reactor designs allowing for high-specific thermal powers at low pressures, but explicitly consider easy scalability for large industrial applications. Among others, scalability considerations should include the often time-consuming procedures of filling the reactive material into the reaction chamber, and also the reduction of the overall thermal mass of the storage reactor system.

For instance, Schmidt et al. developed a packed bed thermochemical reactor operated with calcium oxide on a 10 kW scale [67]. A peak power of 7.5 kW was experimentally demonstrated, which corresponds to a specific thermal power of 375 W/kg hydroxide. For comparison, Richter et al. reached a maximum

specific thermal power of 640 W/kg hydrated salt with the tube-bundle heat exchanger design [24], [68]. Drawbacks of both of the concepts investigated by Richter and Schmidt are the high thermal masses of the thermochemical storage: approximately 10 kg steel mass in the case of the calcium chloride heat transformer (14 kg steel per kg hydrated salt), and 145 kg steel mass in the case of the calcium oxide energy storage (7 kg steel per kg hydroxide). These numbers demonstrate that although the concepts show promising results on lab-scale, a scale-up of the storage design for industrial applications is hardly reasonable.

1.2 Research objectives

The research objectives of the present thesis are based on the state-of-the-art of thermochemical energy storage and heat transformation with $\text{SrBr}_2/\text{H}_2\text{O}$ as described in the previous chapter. They can be grouped into two leading research questions, which will be further detailed in the following:

Is $\text{SrBr}_2/\text{H}_2\text{O}$ a suitable reaction system for TES and heat transformation under conditions relevant for industrial applications, i.e., 150 °C – 300 °C?

This research question particularly includes the investigation of pressure-temperature correlations for the hydration and dehydration reaction, and the identification of a possibly occurring thermal hysteresis. This is necessary in order to identify suitable storage operation parameters in terms of charging/discharging pressures and temperatures. Furthermore, the effective reaction rates need to be determined since they give the maximum specific thermal power of the TES (a detailed analysis on the physical reaction mechanisms is not within the scope of this work). In contrast to the expected specific thermal power, the energy density can be estimated from literature data on the reaction enthalpy. At last, cycle stability over a large number of cycles is a necessary prerequisite for any industrial storage application. This also includes microscopic and macroscopic transformations within the reactive bulk phase, such as agglomeration.

1 Introduction

Additionally, in the present work, the focus is set on the development of a storage design which features high specific thermal powers (kW/m^3) rather than a high energy storage density (kWh/m^3). In contrast to the existing work on $\text{SrBr}_2/\text{H}_2\text{O}$ with focus on long-term storage applications, the present work is motivated by target applications in industrial waste heat recovery, e.g. for the continuous thermal upgrade of waste heat for direct process re-integration. These go along with a high cycling frequency and very specific re-integration demands (e.g. process heat temperatures and thermal powers), so that the specific properties of thermochemical TES compared to sensible and latent TES are more likely to pay off the increased effort. This leads to the second research question:

How can a thermochemical storage unit be designed to provide high specific thermal powers as well as easy scalability for large industrial applications?

Usually, the low thermal conductivity of loose bulks of salt hydrates is regarded as the bottleneck for high-power applications, as in many cases, the heat transfer, and not the reaction kinetics or the mass transfer rates are limiting the thermal power of thermochemical TES systems. Within this work, the questions shall be answered on how a packed-bed storage cell can be designed in order to cope with the low thermal conductivity of the reactive medium by the use of highly-conductive heat transfer structures. At the same time, the chosen design shall be transferable to industrial applications, which means that, amongst other properties, it must be robust with respect to macroscopic changes in the bulk phase. Apart from these hands-on research objectives, the performance-dominating aspects need to be quantitatively understood in order to identify optimization potentials. This research objective closely relates to the question concerning which internal processes will be performance-dominating for the storage operation in an industrial application scenario. However, even if the above-mentioned storage characteristics allow giving some first remarks on the storage's benefits in different application scenarios, the quantitative evaluation of suitable application scenarios, e.g. based on the determination of energetic and exergetic efficiencies, is out of scope of this work.

To sum up, the present work involves the investigation of a thermochemical energy storage and heat transformer along the path from the fundamental characterization of the thermochemical working pair towards the demonstration of the technology in a lab-scale storage unit under application-relevant operation conditions, and ends with the overall storage performance analysis. The different methods which were used in the experimental and numerical studies are briefly described in the following.

1.3 Methods

Since details on the different experimental setups and the numerical simulation tool are given in the journal publications associated with this thesis, this section gives a broader overview over the methods used. Alongside, the corresponding journal contributions are briefly introduced.

1.3.1 Experimental material characterization

Starting point of the characterization of $\text{SrBr}_2/\text{H}_2\text{O}$ as reference thermochemical reaction system was a previous study based on thermogravimetric analysis (TGA) measurements. This study indicated that the anhydrous strontium bromide salt reacts with water vapor in a reversible chemical reaction, with the cycle stability demonstrated for ten hydration/dehydration cycles [42]. Following up on this first study, the detailed characterization of the $\text{SrBr}_2/\text{H}_2\text{O}$ reaction system was conducted by two different experimental approaches in the present work.

Firstly, two commercial thermogravimetric analysis (TGA) devices were used for high-resolution reaction conversion measurements under defined temperature and pressure conditions. The mass of the sample in these experiments was small (approximately 15 mg), which allowed for the determination of the effective rate of reaction. The atmosphere in the sample chamber, which was open to the ambience, was set by controlling the volumetric flows of steam as reactive gas

1 Introduction

and nitrogen as purge gas. Secondly, a specifically designed lab-scale setup with approximately 1 kg sample mass was implemented, mainly dedicated to identify the temperature range of the chemical reaction if operated under pure steam atmosphere and pressures up to approximately 150 kPa. The test infrastructure to operate the storage cell, i.e. the thermal infrastructure and steam supply, was adopted from a previous research project on thermochemical energy storage and heat transformation based on calcium chloride [24]. Apart from the measurement of the bulk temperatures and the steam pressure, the reaction conversion was monitored via a level indicator installed in the evaporator/condenser.

Based on the geometry of the measurement cell, a simplified numerical model of the discharging process was implemented and compared to experimental data. The main objective of this work was to prepare the implementation of a more advanced numerical model for a complex reactor design. The results are summarized in two journal contributions: **I. Pre-study**, which contains experimental data on the hydration reaction temperatures from the lab-scale storage cell and the results on the basic numerical study, and **III. Material characterization**. The latter includes empirical correlations on the pressure-dependent reaction temperatures of both the hydration and the dehydration reaction from the lab-scale setup, along with the analysis of the cycle stability over 100 cycles determined via TGA measurements. The manuscript concludes with empirical models on the hydration and dehydration reaction rates, which were determined from TGA measurements under varying temperatures and water vapor partial pressures.

1.3.2 Experimental proof-of-concept

In parallel to the experimental work on the material characterization, the preparations for the experimental proof-of-concept were started based on the results of the pre-study. A lab-scale infrastructure to provide steam as reacting gas and a thermal infrastructure to charge and discharge the storage under application-relevant operation conditions was designed, constructed, and brought into op-

eration. With the setup, steam-based storage modules with thermal powers up to approximately 5 kW can be investigated. The challenge of implementing such a test infrastructure is the operation with steam in a broad pressure range, from vacuum to high pressures in a closed system (1 kPa – 600 kPa). Hence, air tightness and large pipe diameters are required, along with heater systems to prevent condensation. For safe operation of the pressure equipment in a broad temperature range, the setup was designed for maximum heat transfer fluid temperatures of 320 °C in the storage module, and 170 °C in the evaporator. Within the present thesis, a 1 kW prototype of a scalable storage module was developed and experimentally characterized in terms of its thermal performance. This prototype contained 5 kg of the reactive material. In contrast to the lab-scale setup used for the material characterization experiments, this 1 kW prototype is designed to achieve high specific thermal powers. It is equipped with temperature probes within different positions in the bulk phase and the heat transfer fluid circuit. Apart from that, the thermal powers transferred between the heat transfer fluid and the storage module and the reaction conversion were experimentally determined. The latter was obtained from the measurement of the fluid level in the evaporator/condenser. The experimental results of the 1 kW prototype have been published in paper **II. Proof-of-concept**. This paper contains the results from the above-mentioned setup through a broad range of charging and discharging temperatures and powers, with the main objective being the investigation of the storage's application range.

1.3.3 Numerical analysis of the potential and the limitations of the storage design

Due to the complex geometry of the storage design, the performance characteristics of the storage module cannot be described satisfyingly in an analytical way. Hence, a numerical model based on the finite element method (FEM) was implemented for the purpose of a quantitative analysis on the performance-dominating aspects. The numerical model of the proof-of-concept reactor design

1 Introduction

contains the empirical reaction rate models, which were obtained from the TGA measurements, and the correlations on the pressure-dependent reaction temperatures derived from the 1 kg-measurement cell. The model validation was performed by the comparison of the simulation results with the experimental data obtained with the 1 kW prototype. It was proven that the thermal performance of the storage module is mainly determined by the heat transfer rates. The results of this study are summarized in the manuscript **IV. Performance analysis**. This journal contribution concludes with a thermal sensitivity study, which aims at the quantitative investigation of the different contributors to the overall performance characteristics of the storage. It was shown that the most important contributor is not the low thermal conductivity of the reactive bulk phase, but the heat transfer from the bulk to the heat exchanger wall. Based on the discussion of the heat transfer limitation and the results of the simulation studies, design guidelines for the layout of large-scale storages are proposed.

2

Chapter 2

Publications

This thesis is based on the work published in the following journal contributions:

I. Pre-Study

Jana Stengler, Julius Weiss, Marc Linder (2019): Analysis of a Lab-Scale Heat Transformation Demonstrator Based on a Gas-Solid Reaction. *Energies*, 12, 2234. DOI: 10.3390/en12122234.

Contribution declaration: main author, conduction of the experimental work and data evaluation.

This paper was invited to the *Energies* Special Issue "Selected Papers from Heat Power Cycles Conference 2018", after the original paper was published in the conference proceedings. It represents the progress of the project at an early stage. In contrast, the three following papers were completed in short sequence during the last year and can therefore be considered as a rather consistent trilogy.

2 Publications

II. Proof-of-concept

Jana Stengler, Marc Linder (2020): Thermal energy storage combined with a temperature boost: An underestimated feature of thermochemical systems. *Applied Energy*, 262, 114530. DOI: 10.1016/j.apenergy.2020.114530.

Contribution declaration: main author, conduction of the experimental work (except for the SEM imaging) and data evaluation.

III. Material characterization

Jana Stengler, Inga Bürger, Marc Linder (2020): Thermodynamic and kinetic investigations of the SrBr₂ hydration and dehydration reactions for thermochemical energy storage and heat transformation. *Applied Energy*, 277, 115432. DOI: 10.1016/j.apenergy.2020.115432.

Contribution declaration: main author, experimental work and data evaluation.

IV. Performance analysis

Jana Stengler, Inga Bürger, Marc Linder (2021): Performance analysis of a gas-solid thermochemical energy storage using numerical and experimental methods. *International Journal of Heat and Mass Transfer*, 167, 120797. DOI: 10.1016/j.ijheatmasstransfer.2020.120797.

Contribution declaration: main author, experimental work, numerical model implementation and data evaluation.

Additionally, parts of this project have been published in the following contributions to international conferences:

Jana Stengler, Eva Fischer, Julius Weiss, Marc Linder (2018): Experimental Results of a 1 kW Heat Transformation Demonstrator based on a Gas-Solid Reaction. Heat Powered Cycles Conference 2018, Sept. 16.-19., 2018, Bayreuth, Germany.

Jana Stengler, Marie Gollsch, Julius Weiss, Marc Linder (2018): Porous media for thermochemical energy storage: experimental investigation on structural changes of reactive materials. InterPore 2018, May 14.-17., 2018, New Orleans, USA.

Jana Stengler, Torsten Ascher, Marc Linder (2017): High temperature thermochemical heat transformation based on SrBr_2 . 12th IEA Heat Pump Conference 2017, May 14.-18., 2017, Rotterdam, Netherlands.

Jana Stengler, Marius Drexler, Marc Linder (2017): Waste Heat Driven Thermochemical Heat Transformation based on a Salt Hydrate. International Renewable Energy Storage Conference IRES 2017, March 14.-16., 2017, Düsseldorf, Germany.

Jana Stengler, Margarethe Richter, Marc Linder (2016): Thermochemical energy storage and heat transformation based on SrBr_2 : generic reactor concept for validation experiments. Materials Science and Engineering (MSE) 2016, Sept. 27.-29., 2016, Darmstadt, Germany.

2 Publications

2.1 Paper I: Pre-study

This article was published in *Energies*, 12, 2234, Copyright MDPI (2019).
<https://www.mdpi.com/1996-1073/12/12/2234>

Article

Analysis of a Lab-Scale Heat Transformation Demonstrator Based on a Gas–Solid Reaction †

Jana Stengler * , Julius Weiss and Marc Linder

German Aerospace Center (DLR), Institute of Engineering Thermodynamics, 70569 Stuttgart, Germany; julius.weiss@ise.fraunhofer.de (J.W.); marc.linder@dlr.de (M.L.)

* Correspondence: jana.stengler@dlr.de; Tel.: +49-711-6862-8238

† The original paper was presented in: Stengler, J., Fischer, E., Weiss, J., Linder, M. Experimental Results of a 1 kW Heat Transformation Demonstrator based on a Gas–Solid Reaction. Riehl, R., Preißinger, M., Eames, I., Tierney, M., Eds. In Proceedings of the Heat Powered Cycles Conference 2018, Bayreuth, Germany, 16–19 September 2018. ISBN: 978-0-9563329-6-7.

Received: 27 April 2019; Accepted: 5 June 2019; Published: 12 June 2019



Abstract: Heat transformation based on reversible chemical reactions has gained significant interest due to the high achievable output temperatures. This specific type of chemical heat pump uses a reversible gas–solid reaction, with the back and forward reactions taking place at different temperatures: by running the exothermic discharge reaction at a higher temperature than the endothermic charge reaction, the released heat is thermally upgraded. In this work, we report on the experimental investigation of the hydration reaction of strontium bromide (SrBr_2) with regard to its use for heat transformation in the temperature range from 180 °C to 250 °C on a 1 kg scale. The reaction temperature is set by adjusting the pressure of the gaseous reactant. In previous experimental studies, we found the macroscopic and microscopic properties of the solid bulk phase to be subject to considerable changes due to the chemical reaction-. In order to better understand how this affects the thermal discharge performance of a thermochemical reactor, we combine our experimental work with a modelling approach. From the results of the presented studies, we derive design rules and operating parameters for a thermochemical storage module based on SrBr_2 .

Keywords: heat transformation; thermochemical reaction; chemical heat pump; thermal upgrade; gas–solid reaction

1. Introduction

Thermochemical reactions, for example reversible reactions between a gas and a solid, have been widely discussed in literature in the context of thermal energy storage. Compared to latent or sensible energy storage technologies, thermochemical systems offer significantly higher energy storage densities [1]. Another key feature of thermochemical energy storage is the possibility to control the charge and discharge temperatures by adjusting the concentration of the reactants: if the gas pressure is increased in a gas–solid reaction system, the reaction temperature rises. This effect can be used to transform thermal energy from a lower temperature level to a higher temperature level, the so-called heat transformation or chemical heat pump [2,3]. Different thermodynamic heat transformation and chemical heat pump processes have been discussed in the literature, and a number of studies have been published that clearly highlight the potential of heat transformers for the reduction of low-enthalpy waste heat in industrial processes [4,5]. Although there are several lab-scale setups proposed with different gas–solid working pairs, no technical implementation of a thermochemical heat transformer on an industrial scale has been reported [6–8]. Regarding suitable gas–solid reactive couples, there is a broad spectrum of chemical reactions discussed, e.g., ammonia-, hydrogen- or steam-based working pairs, covering a wide range of operating temperatures [9].

The basic concept of heat transformation generally requires three temperature levels and two pressure stages (see Figure 1a, with water vapor being the gaseous reactant). For providing the reaction enthalpy ($\Delta_R H$) of the endothermic reaction as well as for supplying the evaporation enthalpy of the gaseous component ($\Delta_V H$), waste heat at a temperature of T_{waste} is used. During the charging process, the emerging vapor is condensed at ambient temperature (T_{ambient}). In our work, we follow a different approach to achieve thermal upgrade at a higher absolute temperature level. As depicted in Figure 1b, the heat transformation process described in this work requires four temperature stages: the two upper ones are related to the later application process, and the two lower ones are used for thermal compression of the gaseous reactant. The lowest temperature level (condensation at ambient temperature T_{ambient}) is needed for vapor removal from the reaction chamber in order for the endothermic reaction to reach complete turnover at a low pressure (p_{low}). Hence, the chemical reaction takes place at a low reaction temperature ($T_{\text{low val.}}$), and the thermochemical storage is charged by low-value process heat. During the exothermic discharging process, low-temperature waste heat is used for providing steam at a higher pressure (p_{high}) for running the chemical reaction. The available waste heat temperature defines the vapor pressure and, thus, determines the maximum thermal upgrade of the released high-value process heat.

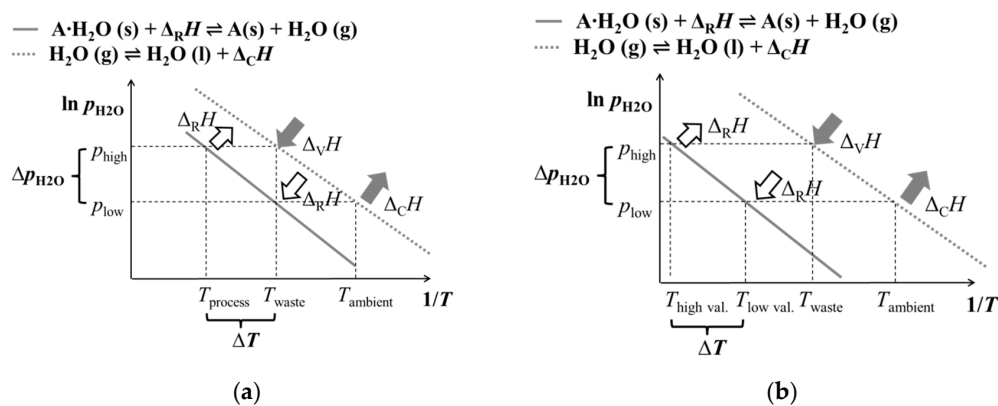
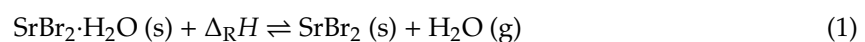


Figure 1. Van't Hoff diagrams of generic water vapor-solid reactions combined with the vapor-liquid equilibrium of the gaseous reactant. Depending on the chosen gas-solid working pair, two modes of operation are possible: (a) thermal upgrade of low temperature waste heat (T_{waste} to T_{process}) and (b) thermal upgrade of high-temperature process heat ($T_{\text{low val.}}$ to $T_{\text{high val.}}$) driven by low-temperature waste heat (operation concept of this work).

With this approach, we are able to re-use low-temperature waste heat as a driving source for high-temperature heat pump processes. Depending on the chosen gas-solid working pair, the operating temperatures of the heat pump process can be adapted to a specific application.

In a first study, we identified the hydration and dehydration reaction of strontium bromide (SrBr_2) as a potential candidate for thermochemical heat transformation in the temperature range above 150°C [10]. The non-toxic inorganic salt forms anhydrous, monohydrate, and hexahydrate phases and, prior to our study, it has been discussed in literature exclusively in the context of low-temperature energy storage for seasonal storage applications [11,12]. For achieving low temperatures required in seasonal storage applications, the chemical reaction is limited to the phase change from the monohydrate phase to the hexahydrate phase, which occurs at temperatures of 50°C to 80°C . The reaction temperatures can be increased significantly by limiting the phase change from the anhydrous to the monohydrate phase, which is the focus of our work:



This reversible gas-solid reaction takes place at temperatures of 150°C or higher, which is very interesting for industrial heat transformation applications as it exceeds the working range of conventional heat pumps. Although the reaction is chemically reversible and cycle stability was

experimentally demonstrated for 10 dehydration/re-hydration reaction cycles in thermogravimetric analysis (TGA) experiments, a thermal hysteresis of 22 K was reported in TGA measurements conducted at a water vapor partial pressure of 5 kPa [10].

The van't Hoff equation provides a first assumption of the correlation between the vapor pressure and reaction temperature based on the standard molar enthalpy and entropy of reaction:

$$\log(p/p^+) = \frac{\Delta_{\text{R}}S}{\mathbf{R}} - \frac{\Delta_{\text{R}}H}{\mathbf{R}T}, \quad (2)$$

with \mathbf{R} being the universal gas constant, and the reference pressure $p^+ = 10^3$ hPa. From standard molar enthalpy and entropy of formation given in the NBS Tables [13], the reaction enthalpy and entropy is calculated as $\Delta_{\text{R}}H = 71.98$ kJ/mol and $\Delta_{\text{R}}S = 143.93$ J/(mol·K), respectively.

For confirming the $p(T)$ -correlation, we developed a method for obtaining data from experiments on a 1 kg scale [14]. In the experimental study, we observed that the exothermic reaction from the anhydrous phase to the monohydrate takes place at around 229 °C when water vapor is supplied at a pressure of 70 kPa. This value is higher than the reaction temperature expected from the van't Hoff Equation (2), which returns a temperature of 217 °C for the same vapor pressure. During the dehydration process at a vapor pressure of 6.5 kPa, a minimum temperature of 190 °C was found. Calculated from Equation (2), this vapor pressure corresponds to a reaction temperature of 159 °C. Evidently, the van't Hoff Equation (2) does not give an exact estimation of the correlation between vapor pressure and reaction temperature. However, this correlation is required for further investigations of the heat transformation operation conditions with the SrBr₂/H₂O working pair, and therefore needs to be experimentally determined.

When opening the reaction chamber after having conducted 11 dehydration/re-hydration cycles with different reaction conditions, we detected agglomeration effects in the bulk. Even though this was observed consistently during the series of experiments, the changes in the bulk structure did not affect the reaction dynamics of the thermochemical reactor. Based on the results of these investigations, we see very high potential in the SrBr₂/H₂O working pair for achieving a thermal upgrade of 50 K or more in a single-stage heat transformation process with only one working pair. Therefore, our current work is focused on the investigation of experimental operation conditions and reaction chamber designs that allow for heat transformation in a temperature range of 180 °C to 250 °C at high thermal powers.

2. Materials and Methods

To charge the storage system, thermal energy is transferred indirectly to the solid bulk material via a heat transfer fluid. In the course of the endothermic chemical reaction, the gaseous reactant escapes from the powder bulk and must be separated from the solid phase: the emerging steam is condensed in a separate heat exchanger in order to keep the pressure low and thus to reach complete reaction turnover. In this work, we focus on the thermal discharge process, which starts when water vapor is introduced into the reaction chamber. The thermal energy released by the subsequent chemical reaction is transferred from the powder bulk to the heat transfer fluid. For vapor generation, we use a tube bundle heat exchanger. In order to calculate the reaction conversion, it is equipped with a level indicator measuring the amount of water being consumed during the chemical reaction.

In general, there are three main processes that affect the thermal performance of a thermochemical reactor: vapor mass transfer into the solid bulk phase, heat transfer from the solid bulk phase to the heat transfer fluid, and the rate of the chemical reaction at the given operation conditions. To qualify how the physical and chemical properties of the reactive material affect the thermal performance of a thermochemical reactor and to quantify these local effects in order to identify potential bottlenecks, we included the relevant physical processes during the chemical reaction in a model based on the finite element method (FEM). For numerical calculations, we used solvers from the Comsol Multiphysics® simulation software (Stockholm, Sweden). The validity of the simulation studies is verified by comparison with experimental data from a packed bed thermochemical reactor.

For the validation reactor, a rectangular reaction chamber configuration with indirect heat transfer was chosen. The heat exchanger consisted of two single-embossed pillow plates that were mounted back to back and were equally flowed through by heat transfer fluid (HTE, Purity™ FG Heat Transfer Fluid (Petro-Canada Lubricants Inc., Mississauga, Ontario, Kanada)) at a constant rate of 2 kg/min. The heat exchanger plates formed a 290 mm × 225 mm × 20 mm volume filled with 1,050 g of SrBr₂·H₂O (resulting packed bed height: 205 mm). From the top and the bottom of the reaction chamber, water vapor was introduced into the reactive bulk. Metal filters with a mesh size of 5 μm kept the packed bed in position and minimized undesired release of powder into the pipework of the test setup. The thermochemical reactor was equipped with a pressure sensor and several temperature probes that monitored the solid bulk's temperature at different positions within the fixed bed. During the experiment, the temperature of the heat transfer fluid was kept at a constant value. A schematic drawing of the setup is depicted in Figure 2.

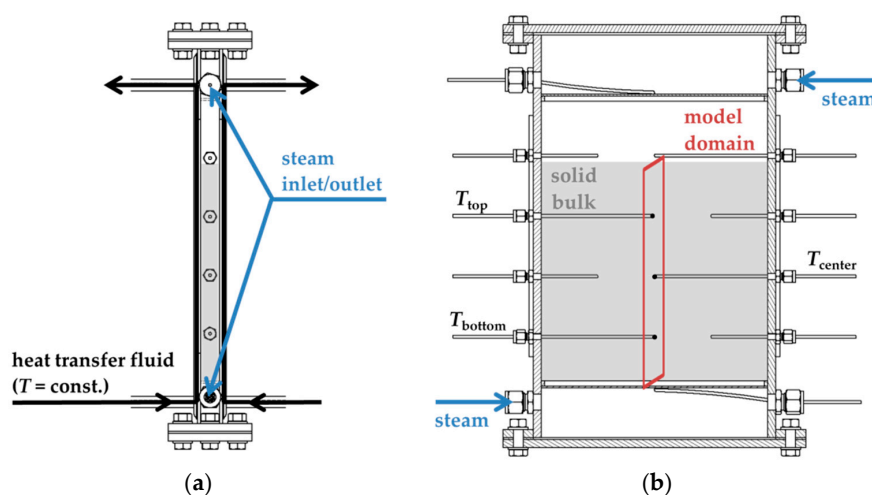


Figure 2. Schematic reactor geometry used for both modelling as well as experimental studies: (a) side view and (b) front view.

As 2D-model domain, we chose a cross-section through the center of the solid bulk volume. For model implementation, the solid phase was assumed to be a homogenous porous medium. Material properties were assessed by the means of literature data or own measurements and calculations. A summary is given in Table 1.

Table 1. Chemical and physical properties of the SrBr₂/H₂O reaction system.

Category	Parameter	Value	Reference
solid properties	density SrBr ₂	4216 kg/m ³	literature data [15]
	density SrBr ₂ ·H ₂ O	3911 kg/m ³	linear interpolation between SrBr ₂ and SrBr ₂ ·6H ₂ O densities from [15]
	heat capacity SrBr ₂	75.35 J/(mol·K)	literature data [13]
	heat capacity SrBr ₂ ·H ₂ O	120.9 J/(mol·K)	literature data [13]
bulk properties (SrBr ₂ and SrBr ₂ ·H ₂ O)	bulk porosity (SrBr ₂ ·H ₂ O)	0.71	experimentally determined for this specific reactor setup
	permeability	1·10 ⁻¹⁰ m ²	literature data on SrBr ₂ ·H ₂ O [16]
	thermal conductivity λ _{eff}	0.2–0.6 W/(m·K)	assumption based on data on SrBr ₂ ·H ₂ O [16]
hydration reaction (SrBr ₂ to SrBr ₂ ·H ₂ O)	enthalpy of reaction Δ _R H	71.98 kJ/mol	calculated from literature data on enthalpy of formation [13]
	entropy of reaction Δ _R S	143.93 J/(mol·K)	calculated from literature data on entropy of formation [13]
	effective rate coefficient k _{eff}	1.6·10 ⁻³ 1/s	fit to experimental data from isothermal thermogravimetric analysis (TGA) measurements at 68.8 kPa (unpublished)
	pressure term exponent n	2	

Movement of the solid is neglected, and the porosity is set to a constant value during the reaction. Furthermore, a change in bulk volume or bulk permeability is not yet considered. The gas phase, which consists of pure water vapor with ideal gas properties, penetrates the porous media according to Darcy's law. Local thermal equilibrium is assumed between the gas and the solid phase. As the temperature differences within the observed volume are very small, heat radiation does not play a significant role and is therefore neglected.

Boundary conditions concerning heat and mass transfer in the relevant model domain are depicted in Figure 3. It is assumed that the overall heat transfer coefficient $k_{\text{solid-HTF}}$ from the powder bed to the heat transfer fluid is determined by the heat transfer coefficient on the HTF side of the pillow plate heat exchanger. This value is calculated from the correlations on forced convection in planar gaps given in the VDI Heat Atlas [17] for laminar fluid flow. Assuming the pillow plates as planar gap with 1.5 mm gap width and a HTF flow rate of 2 kg/min result in $k_{\text{solid-HTF}} = 365 \text{ W}/(\text{m}^2 \cdot \text{K})$.

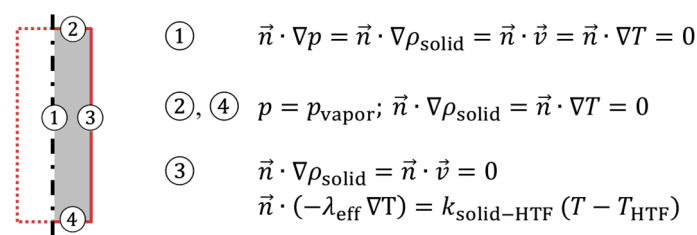


Figure 3. Boundary conditions for heat and mass transfer in the 2D model domain (see Figure 2) with \vec{v} being the Darcy flux and \vec{n} the normal vector.

The exothermic hydration reaction is implemented as a heat source with a first order rate law,

$$\frac{dX}{dt} = k_{\text{eff}} \cdot (1 - X) \cdot \left(\frac{p}{p_{\text{R,Hyd}}(T)} - 1 \right)^n, \quad (3)$$

with X being the reaction conversion and p the water vapor (partial) pressure. The effective rate coefficient k_{eff} and the pressure term exponent n given in Table 1 were fitted to isothermal TGA experiments (temperature range 186 °C to 212 °C) at a partial vapor pressure of 68.8 kPa.

In these measurements, it is observed that the effective reaction rate decelerates with increasing temperature, as the equilibrium pressure increases with increasing temperature, thus shifting the system closer to the thermodynamic equilibrium. This rate-diminishing effect is modelled by the last term in Equation (3), and generally prevents any thermal runaway. The temperature-dependent water vapor pressure $p_{\text{R,Hyd}}(T)$ of the hydration reaction can be obtained from thermodynamic data on the reaction enthalpy and reaction entropy (van't Hoff line), as described by Equation (2), or from experimental correlations. Extending the reaction rate model to larger temperature and pressure ranges will be part of our future work.

3. Results

We conducted several sets of experiments. Within the series, the vapor pressure and, accordingly, the temperature of the heat transfer fluid varied: as strontium bromide forms a hexahydrate phase ($\text{SrBr}_2 \cdot 6\text{H}_2\text{O}$) at high vapor pressures or low temperatures, respectively, the preheat temperature of the anhydrous solid must be raised for high vapor pressures in order to ensure the exclusive formation of $\text{SrBr}_2 \cdot \text{H}_2\text{O}$. Up to 15 dehydration/re-hydration cycles were performed in a row with one batch of reactive material. Afterwards, the reactor was refilled with a fresh batch of $\text{SrBr}_2 \cdot \text{H}_2\text{O}$. The vapor pressure was varied from 18 kPa up to 145 kPa, and the discharge temperature was set in a range of 132 °C to 210 °C. The maximum temperature measured at the central position in the packed bed during the hydration reaction is plotted against the set vapor pressure in Figure 4. All experiments considered, the highest maximum temperature was 256 °C at 144 kPa vapor pressure.

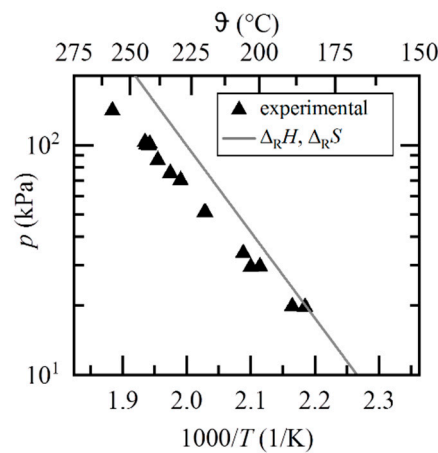


Figure 4. Van't Hoff plot for the hydration reaction: experimental data and correlation based on thermodynamic data ($\Delta_R H$, $\Delta_R S$ calculated from literature data on enthalpy and entropy of formation [13]).

The data points shown in Figure 4 reveal that the measured temperature values clearly exceed the temperatures derived from thermodynamic data, especially for high pressures. For this reason, a linear regression of the experimental data points was calculated to model the temperature dependency of the water vapor pressure $p_{R,Hyd}$ of the hydration reaction in the FEM simulation:

$$\log(p_{R,Hyd}/\text{hPa}) = 8.84 - 3.02 \cdot \frac{10^3}{T/\text{K}}. \quad (4)$$

This correlation was also used in the reaction rate model described in Equation (3).

The simulation study results are compared with the results of the prior described experiments, with the measured pressure curve being defined as input variable for the simulation. In Figure 5a, the temperature progression at different positions within the solid bulk is shown for a discharge temperature of 209.5 °C and a vapor pressure of 70 kPa (corresponding to 90 °C evaporation temperature). The graph includes the results of two simulation studies with varying bulk thermal conductivity λ_{eff} . The increase in temperature indicates that the exothermic reaction is in progress. As the reaction approaches complete conversion to the monohydrate, the temperature in the solid bulk begins to decrease. Evidently, temperature progression in the experimental setup is not homogenous within the bulk phase: at the lowest temperature measuring point (T_{bottom}), a lower maximum temperature is observed. We assume that this effect is caused by macroscopic inhomogeneities within the porous medium, such as cracks, which may affect the temperature measurement. In the simulation study, the temperatures trends at the three positions proceeded identically, which is why only the temperature at the central position of the reactor (T_{sim}) is depicted in Figure 5a. The jumps occurring the temperature curves (e.g., at 1.3 h experimental time) are caused by a sudden increase in pressure due to condensation/evaporation in the setup. The pressure increase leads to a higher reaction temperature in the solid bulk. As the measured pressure curve was used as input parameter for the simulation study, the same effect occurs in the numerical study. In the case of the lower bulk thermal conductivity ($\lambda_{eff} = 0.2 \text{ W}/(\text{m}\cdot\text{K})$), maximum temperatures in the simulation were about 7 K lower than in the experiment. In addition, the temperature in the simulation study dropped to its initial value after 3.5 h, whereas in the experiment it was not possible to measure a complete temperature drop even after four hours. In the study with increased bulk thermal conductivity ($\lambda_{eff} = 0.6 \text{ W}/(\text{m}\cdot\text{K})$), temperatures dropped to the initial value after two hours.

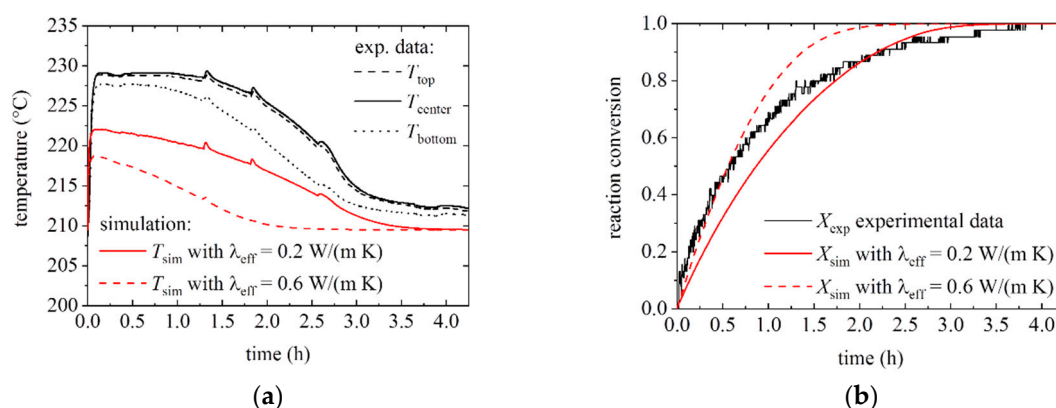


Figure 5. Experimental and simulation results for 209.5 °C discharge temperature and 90 °C evaporation temperature. The simulation study is based on the pressure curve measured in the experiment. (a) Temperature profile and (b) reaction conversion.

In Figure 5b, the reaction conversion is depicted for both the simulation as well as the experiment, where the turnover is calculated from the fluid level measurement. In the initial study with $\lambda_{eff} = 0.2$ W/(m·K), the experimental yield is higher than the simulation result up to a turnover of roughly 85%. Afterwards, the progress of the experimental turnover decelerates for high reaction yields, and full turnover is achieved about 20 min later in the experiment than in the corresponding simulation study. Increasing the thermal conductivity of the bulk phase to $\lambda_{eff} = 0.6$ W/(m·K) leads to significantly shorter discharging times.

4. Discussion

Although the model does not reproduce the experiments quantitatively due to the uncertainty of the input parameters (in particular, the parameters of the reaction rate model and macroscopic inhomogeneities), it allows for the qualitative observation and identification of the factors having the greatest influence on the progression of the hydration reaction and thus on the discharge of the storage module.

From the observation that the simulated temperature curves perfectly overlap for the three different positions within the fixed bed, the conclusion can be drawn that mass transport within the bulk material does not lead to a limitation for the given hydration reaction conditions. This is an important finding for the design of suitable reactor geometries. Still, this effect should be further analyzed regarding the lower absolute pressures and gas densities during the charging process of the thermochemical reactor.

The influence of low bulk thermal conductivities on the reaction turnover curve and, hence, the reactor's overall performance was numerically studied. Increasing the effective thermal conductivity from 0.2 to 0.6 W/(m·K) (f.e. by adding highly conductive additives such as aluminum) reduces the total discharging time by 40% in the simulation study (3.5 h versus 2.1 h for 99% reaction conversion). This is equivalent to a 1.7 times higher average thermal power. According to the experimental results of the generic reactor geometry presented in this work, we recommend a maximum heat transport distance of 10 mm for the design of high-power thermochemical reactors based on SrBr₂/H₂O. Furthermore, the effective thermal conductivity of the bulk could be increased by adding highly conductive inert additives or by the integration of heat conducting structures.

The FEM simulation developed in this work can be used as design tool for the layout of high-power reactor geometries. We assume that the following modifications of the first model can improve the prediction quality of the simulation: firstly, the mathematical model of the reaction rate over-estimates the rate at higher yields. Therefore, the development of an advanced reaction rate model is a subject of our ongoing work. Secondly, the solid bulk is not a homogenous porous medium; therefore, slower reaction progress can occur locally, which is not considered in the model. Moreover, in further

experimental work, we found that the macroscopic and the microscopic properties of the solid bulk material change considerably due to the chemical reaction: the primary particles agglomerated, which was already observed in the experiments described above, and the overall volume of the porous bulk increased after several dehydration/re-hydration cycles [18]. The observed structural changes could also affect the bulk thermal conductivity and thus have an effect on the long-term thermal performance of the storage reactor.

From the thermodynamic point of view, a discharging temperature of 250 °C is feasible with the reaction system $\text{SrBr}_2/\text{H}_2\text{O}$. To achieve this high reaction temperature, steam must be supplied with a pressure of approx. 140 kPa or higher. This requires waste heat temperatures of at least 110 °C for vapor generation. At the same time, the discharging temperature must not be too low: as strontium bromide forms a hexahydrate phase ($\text{SrBr}_2 \cdot 6\text{H}_2\text{O}$) at high vapor pressures or low temperatures, respectively, the minimum discharge temperature must be raised for high vapor pressures in order to ensure the exclusive formation of $\text{SrBr}_2 \cdot \text{H}_2\text{O}$.

Taking the reaction kinetics into account, a minimal temperature difference of 10 K or more between the reaction temperature and the temperature of the heat transfer fluid could be required in case the chemical reaction decelerates considerably close to the thermodynamic equilibrium. This would significantly decrease the thermal power of the storage reactor, or limit the maximum possible discharge temperature. Quantifying the required temperature difference for high reaction rates is part of our ongoing work.

5. Conclusions

In a previous study based on thermogravimetric experiments performed on a mg scale, we identified strontium bromide (SrBr_2) as a promising candidate for thermochemical heat transformation [10]. The work presented here is focused on the investigation of the exothermic hydration reaction from the anhydrous SrBr_2 to its monohydrate phase on a 1 kg scale. Our objective is the identification of suitable operation conditions that allow for heat transformation with output temperatures in the range of 180 °C to 250 °C. Our key findings are as follows:

- The working pair $\text{SrBr}_2/\text{H}_2\text{O}$ allows discharging temperatures up to 250 °C when water vapor is supplied at 110 °C (f.e. driven by low-temperature waste heat);
- Vapor mass transfer in the porous bulk phase does not limit the thermal discharging performance in the analyzed reactor setup;
- The low effective thermal conductivity of the fixed reactive bed is a potential bottleneck for high-power thermochemical storage and heat transformation modules.

Based on the experimental results and the conclusions of our simulation studies presented here, we are currently developing a reactor setup that allows for high specific thermal powers, and which is easily scalable for industrial applications. To increase the effective thermal conductivity of the bulk phase, we are using heat conducting structures made from aluminum. Further design considerations include a minimum pressure loss on the vapor side and a reaction chamber design that is robust with respect to changes of the bulk's macroscopic structure. With this design, we expect to achieve specific thermal powers of minimum 0.25 kW per kg of SrBr_2 . Future work will include investigations with our new test facility, allowing for heat transformation with thermal powers up to 5 kW and output temperatures of up to 320 °C. In particular, quantifying the required temperature difference between the solid's reaction temperature and the discharge temperature, ensuring high reaction rates and, thus, high thermal powers, will be part of our future work.

Author Contributions: All authors contributed to this work by collaboration: conceptualization, experimental investigation, and simulation, J.S.; simulation and validation, J.W.; project supervision, M.L. J.S. is the main author of this manuscript. All authors revised and approved the publication.

Funding: This research was funded by the German Federal Ministry for Economic Affairs and Energy (BMW, "Bundesministerium für Wirtschaft und Energie"), "TheSan" project (03ET1297A).

Conflicts of Interest: The authors declare no conflict of interest. The funders had no role in the design of the study; in the collection, analyses, or interpretation of data; in the writing of the manuscript; or in the decision to publish the results.

Nomenclature

The following abbreviations are used in this manuscript:

eff	effective
exp	experimental
FEM	finite element method
g	gas
H ₂ O	water
HTF	heat transfer fluid
Hyd	hydration
l	liquid
R	reaction
s	solid
sim	simulation
SrBr ₂	strontium bromide
TGA	thermogravimetric analysis

The following Latin variables are used:

$\Delta_C H$	standard molar enthalpy of condensation, J/mol
$\Delta_R H$	standard molar enthalpy of reaction, J/mol
$\Delta_V H$	standard molar enthalpy of evaporation, J/mol
$\Delta_R S$	standard molar entropy of reaction, J/(mol·K)
k_{eff}	effective reaction rate coefficient, 1/s
$k_{\text{solid-HTF}}$	Solid-to-HTF heat transfer coefficient, W/(m ² ·K)
n	pressure term exponent
p	water vapor pressure, Pa
p^+	reference pressure, 10 ³ hPa
R	universal gas constant, 8.3145 J/(mol·K)
T	temperature, K
X	yield of reaction

The following Greek variables are used:

λ_{eff}	thermal conductivity, W/(m·K)
ρ	density, kg/m ³

References

1. Aydin, D.; Casey, S.P.; Riffat, S. The latest advancements on thermochemical heat storage systems. *Renew. Sustain. Energy Rev.* **2015**, *41*, 356–367. [[CrossRef](#)]
2. Wongsuwan, W.; Kumar, S.; Neveu, P.; Meunier, F. A review of chemical heat pump technology and applications. *Appl. Therm. Eng.* **2001**, *21*, 1489–1519. [[CrossRef](#)]
3. Cot-Gores, J.; Castell, A.; Cabeza, L.F. Thermochemical energy storage and conversion: A-state-of-the-art review of the experimental research under practical conditions. *Renew. Sustain. Energy Rev.* **2012**, *16*, 5207–5224. [[CrossRef](#)]
4. Spoelstra, S.; Haije, W.G.; Dijkstra, J.W. Techno-economic feasibility of high-temperature high-lift chemical heat pumps for upgrading industrial waste heat. *Appl. Therm. Eng.* **2002**, *22*, 1619–1630. [[CrossRef](#)]
5. Chan, C.W.; Ling-Chin, J.; Roskilly, A.P. A review of chemical heat pumps, thermodynamic cycles and thermal energy storage technologies for low grade heat utilisation. *Appl. Therm. Eng.* **2013**, *50*, 1257–1273. [[CrossRef](#)]
6. Wu, S.; Li, T.X.; Yan, T.; Wang, R.Z. Experimental investigation on a novel solid-gas thermochemical sorption heat transformer for energy upgrade with a large temperature lift. *Energy Convers. Manag.* **2017**, *148*, 330–338. [[CrossRef](#)]

7. Willers, E.; Groll, M. Two-stage metal hydride heat transformer. *Int. J. Hydrogen Energy* **1999**, *24*, 269–276. [[CrossRef](#)]
8. Haije, W.G.; Veldhuis, J.B.J.; Smeding, S.F.; Grisel, R.J.H. Solid/vapour sorption heat transformer: Design and performance. *Appl. Therm. Eng.* **2007**, *27*, 1371–1376. [[CrossRef](#)]
9. Yu, Y.; Zhang, P.; Wu, J.; Wang, R. Energy upgrading by solid–gas reaction heat transformer: A critical review. *Renew. Sustain. Energy Rev.* **2008**, *12*, 1302–1324. [[CrossRef](#)]
10. Richter, M.; Habermann, E.-M.; Siebecke, E.; Linder, M. A systematic screening of salt hydrates as materials for a thermochemical heat transformer. *Thermochim. Acta* **2017**, *659*, 136–150. [[CrossRef](#)]
11. Mauran, S.; Lahmidi, H.; Goetz, V. Solar heating and cooling by a thermochemical process. First experiments of a prototype storing 60 kW h by a solid/gas reaction. *Sol. Energy* **2008**, *82*, 623–636. [[CrossRef](#)]
12. Marias, F.; Neveu, P.; Tanguy, G.; Papillon, P. Thermodynamic analysis and experimental study of solid/gas reactor operating in open mode. *Energy* **2014**, *66*, 757–765. [[CrossRef](#)]
13. Wagman, D.D.; Evans, W.H.; Parker, V.B.; Schumm, R.H.; Halow, I.; Bailey, S.M.; Churney, K.L.; Nuttal, R.L. The NBS Tables of Chemical Thermodynamic Properties. Selected Values for Inorganic and C1 and C2 Organic Substances in SI Units. *J. Phys. Chem. Ref. Data* **1982**, *18*, 1807–1812. [[CrossRef](#)]
14. Stengler, J.; Ascher, T.; Linder, M. High temperature thermochemical heat transformation based on SrBr₂. In Proceedings of the 12th IEA Heat Pump Conference, Rotterdam, The Netherlands, 15–18 May 2017.
15. Perry, D.L. *Handbook of Inorganic Compounds*, 2nd ed.; Taylor & Francis: Boca Raton, FL, USA, 2011; ISBN 1439814619.
16. Michel, B.; Neveu, P.; Mazet, N. Comparison of closed and open thermochemical processes, for long-term thermal energy storage applications. *Energy* **2014**, *72*, 702–716. [[CrossRef](#)]
17. Stephan, P.; Kabelac, S.; Kind, M.; Mewes, D.; Schaber, K.; Wetzel, Th. (Eds.) *VDI-Wärmeatlas*, 11th ed.; Springer: Berlin/Heidelberg, Germany, 2013; ISBN 978-3-642-19981-3.
18. Stengler, J.; Gollsch, M.; Weiss, J.; Linder, M. Porous media for thermochemical energy storage: Experimental investigation on structural changes of reactive materials. Presented at the InterPore Conference 2018, New Orleans, LA, USA, 14–17 May 2018.



© 2019 by the authors. Licensee MDPI, Basel, Switzerland. This article is an open access article distributed under the terms and conditions of the Creative Commons Attribution (CC BY) license (<http://creativecommons.org/licenses/by/4.0/>).

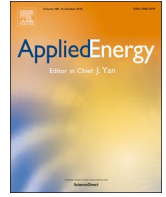
2.1 Paper I: Pre-study

2 Publications

2.2 Paper II: Proof-of-concept

This article was published in *Applied Energy*, 262, 114530,
Copyright Elsevier (2020).

<https://www.sciencedirect.com/science/article/abs/pii/S0306261920300428>



Thermal energy storage combined with a temperature boost: An underestimated feature of thermochemical systems

Jana Stengler*, Marc Linder

Institute of Engineering Thermodynamics, German Aerospace Center (DLR), Pfaffenwaldring 38-40, 70569 Stuttgart, Germany

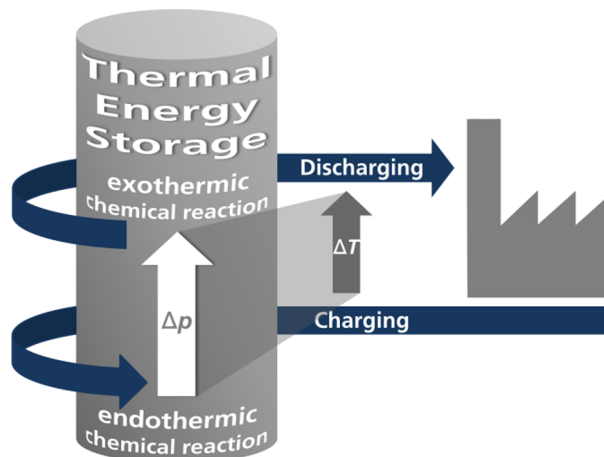


HIGHLIGHTS

- Experimental study on thermal energy storage combined with heat transformation.
- Strontium bromide and water vapor as thermochemical working pair.
- 1 kW thermal power and 100 K temperature boost demonstrated.
- Temperature lift adjustable from 180 °C to 280 °C by steam pressure variation.
- Scalable and modular storage design.

GRAPHICAL ABSTRACT

Operation principle of thermochemical energy storage with combined temperature boost: by increasing the gas pressure before running the exothermic discharging reaction, the stored thermal energy is released at a higher temperature compared to the endothermic charging reaction.



ARTICLE INFO

Keywords:

Thermal energy storage
Thermochemical heat transformation
Thermal upgrade
Strontium bromide
Waste-heat recovery
Energy efficiency

ABSTRACT

The scientific community largely agrees on both the potential of as well as the need for thermal energy storage (TES) in energy-efficient industrial processes. However, state-of-the-art TES technologies (latent or sensible) have one unsolved issue in common: whenever thermal energy is transferred, e.g. between the heat transfer fluid in an industrial application and the TES, the temperature of the transferred heat decreases. Consequently, even if TES systems perfectly de-couple the temporal correlation between the availability of excess heat, and, e.g., the demand for process heat, the stored heat cannot directly be re-integrated in the same process due to the temperature loss caused by two heat transfers.

Here, we report on the development of a thermochemical TES system based on the reversible gas-solid reaction of strontium bromide with water vapor as a reference reaction system. This concept allows for an increase in the temperature of the stored energy without additional process steps, and thereby for a full compensation of the thermal downgrade. The temperature lift is adjustable by variation of the steam pressure, and hence can be adapted to various industrial applications. For example, we charged the storage at 180 °C (1 kPa steam pressure) and discharged it at 280 °C (560 kPa steam pressure), effectively using the module as a heat transformer in addition to the storage function. We present a scalable TES design operating on a 1 kW-scale with 30 min charging and discharging times and an optional temperature boost of up to 100 K.

* Corresponding author.

E-mail address: jana.stengler@dlr.de (J. Stengler).

<https://doi.org/10.1016/j.apenergy.2020.114530>

Received 10 October 2019; Received in revised form 8 January 2020; Accepted 12 January 2020

0306-2619/ © 2020 Elsevier Ltd. All rights reserved.

Nomenclature*Abbreviations*

E/C-unit	evaporator/condenser-unit
HTF	heat transfer fluid
PCM	phase change material
SEM	scanning electron microscope
TES	thermal energy storage

Indices

0	initial conditions
I, II	storage cell I, II
A, C	temperature sensor position A, C
av	averaged
cond	condensation
evap	evaporation
norm	normalized
th	thermal
X	based on reaction conversion

Latin variables

c_p	heat capacity, kJ/(kg·K)
ΔH_R	standard molar reaction enthalpy, kJ/mol
m	mass, kg
\dot{m}	mass flow, kg/s
M	molar mass, g/mol
p	pressure, kPa
P	thermal power, kW
Q	energy, kJ
t	time, s
T	absolute temperature, K
X	reaction conversion

Greek variables

Φ	error contributing to propagation of measurement uncertainties
ϑ	temperature, °C

1. Introduction

The pulp and paper industry is a classic example of an energy-intensive business with a huge potential for waste-heat recovery: its process heat demand in the 100 °C to 500 °C range corresponds to 6% of the European Union member states' overall industrial energy consumption [1]. At the same time, approximately 20 TWh of waste heat between 100 °C and 200 °C are emitted to the ambient every year [2]. If this excess heat was fully recovered, the energy-efficiency with regard to process heat could be improved by almost 10% [1].

Reintegration of such low-grad waste heat as process heat by means of thermal upgrading is the first driving force behind our work. There are different approaches to achieve this, for example with heat pumps of different working principles (e.g. compression or absorption [3]), or, still at the stage of development, adsorption-based or thermochemical heat transformation [4,5]. The operation principle of thermochemical heat transformers is based on reversible chemical reactions, e.g. reactions between a solid and a gas, such as the dehydration and rehydration reaction of salt hydrates. The chemical reaction proceeds along a monovariant equilibrium. Hence, an increased concentration (or pressure) of the gaseous reactant leads to a higher reaction temperature as compared to the same reaction performed at lower pressures. In general, there's a broad spectrum of chemical reactions discussed in literature, e. g. ammonia-, hydrogen- or steam-based thermochemical working pairs for different thermodynamic cycles [6] and applications [7]. On milligram-scale, there are several studies available investigating working materials for chemical heat pumps and thermal energy storage, e.g. systematic screenings of binary inorganic salts [8] or mineral salts [9], and detailed investigations of a variety of salts, such as magnesium oxide [10] or calcium oxalate [11]. Likewise, in the context of low-temperature TES, a lot of effort has been done to identify suitable storage materials, not only with respect to their thermodynamic properties [12], but also with regard to the material costs [13]. Fewer investigations are published on actual heat transformer reactor designs capable of handling gas-solid reactions on a somewhat larger scale [14] (e.g. two-stage heat transformer based on metal hydrides [15], heat transformer based on the hydration and dehydration reaction of calcium chloride [16], ammonia-based heat transformer with calcium chloride [17] or manganese and strontium chloride [18]). However, these heat transformer designs aim at providing a continuous thermal upgrade of low-temperature waste heat, and are not applicable for storing thermal energy with large capacities, which is another requirement for waste-

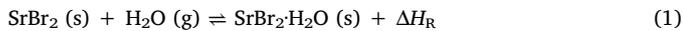
heat recovery in batch processes such as in chemical industries.

Therefore, besides the thermal upgrade, thermal energy storage with high storage capacities and thermal throughputs is the second starting point of our research: while sensible energy storage technology is already well established on industrial scale, e.g. in the form of regenerative heat exchangers, latent energy storage technology is catching up. Higher energy storage densities and constant charging and discharging temperatures are the major advantages of thermal energy storage based on phase change materials (PCM) [19]. Due to the poor thermal conductivity of most PCM storage materials in their solid state, the main drawback associated with latent energy storages is the discharging performance, which is found to be the bottleneck for high-power applications [20,21]. Thus, a lot of effort is spent on increasing the solids' effective thermal conductivity, either by modifying the PCM itself, e.g. by adding highly conductive (nano-) particles such as graphite or copper [22,23], encapsulation [24] or by introducing heat conducting foams or fins [25,26].

Still, regardless of the chosen storage technology, one issue remains unsolved: the temperature of the transferred heat decreases due to the temperature gradient necessary for driving the heat flux. As a consequence, the discharging temperature of thermal energy storages will necessarily be lower than the charging temperature. This effect cuts back plenty of use cases for thermal energy storage. Concluding from these considerations, we combine the approach of thermal energy storage in the 160 °C to 300 °C temperature range with heat transformation based on a thermochemical working pair. While the main performance indicator for storage devices is a high specific storage density (e.g. given in kWh/m³), the key indicator of heat transformer systems is related to their specific power level (e.g. given in kW/m³). A thermochemical storage with combined heat transformation obviously needs to address both aspects. Unfortunately, these are partly contradictory as high thermal throughputs require large heat exchangers, which limits the specific storage density, and increases the specific costs.

Here, we present a thermochemical storage design which is generally suitable for a broad range of gas-solid reactions, and aims at high performances in respect to storage density and thermal power. Despite the generic design, we limited our experimental studies to the use of strontium bromide (SrBr₂) and water vapor as reference thermochemical working pair. Prior to our work, the reaction of strontium bromide monohydrate (SrBr₂·H₂O) with water vapor has been investigated in the context of low-temperature TES at 90 °C maximum, e.g. for seasonal storage applications [27–29]. Michel et al. report a

specific thermal power of 2 W/kg of hydrated salt ($\text{SrBr}_2 \cdot 6\text{H}_2\text{O}$); the total hydrated salt mass was 400 kg [28]. In contrast to these studies, we operate the reaction system at significantly higher temperatures by limiting the chemical reaction to the reaction from the anhydrous phase to the monohydrate salt:



For example, at 144 kPa steam pressure, a hydration temperature of 256 °C was observed when no thermal power was discharged from the reactive system [30]. The dehydration and rehydration reactions were reported to be reversible for at least 10 reaction cycles [8]. With the standard molar reaction enthalpy of 71.98 kJ/mol [31] and a solid density of 4216 kg/m³ (anhydrous SrBr_2 , 247.428 g/mol [32]), the reaction system $\text{SrBr}_2/\text{H}_2\text{O}$ promises a high storage density of 291 kJ/kg or 102 kWh/m³ (anhydrous phase; 70% porosity considered). For comparison, the energy density of phase change materials proposed for latent TES in a similar temperature range (210 °C to 270 °C) varies from 100 kJ/kg to 380 kJ/kg [33].

2. Experimental

2.1. Design considerations

Easy scalability for large industrial applications with both high storage capacities and thermal powers was the general target of our design considerations. Two dominating aspects were therefore considered: firstly, the mass transfer of steam into the packed-bed storage material, and, secondly, the heat transfer between the storage material and the heat transfer fluid.

Different than in sensible or latent TES, the transport of the reactive gas (here: steam) needs to be accounted for in the design of thermochemical TES. In particular under partial vacuum conditions, mass transfer limitations within the bulk volume are an issue for two reasons: Firstly, the existence of a large pressure drop within the solid bulk phase might slow down the chemical reaction, for example, if the gaseous reactant is not removed from the solid fast enough during the endothermic charging reaction. Secondly, a higher gas concentration (or gas pressure) in the bulk phase leads to a higher local reaction temperature, and thereby decreases the gradient to the heat transfer fluid (HTF). Thus, poor mass transfer within the bulk prevents not only high thermal powers, but can also reduce the potential for large temperature boosts. Our design features minimized mass transport distances in the solid bulk phase in combination with large filter areas to achieve minimal pressure loss on the vapor side.

The second aspect is a commonality of thermochemical and latent TES: the low thermal conductivity of the solid bulk phase is a bottleneck for high-power storages. Fopah-Lele et al. found effective thermal conductivities in the range of 0.3–1.3 W/(m·K) for different salt hydrate packed beds (e.g. strontium bromide, calcium chloride) [34]. In addition, structural changes of the bulk material, e.g. by sintering due to reaction cycling, may alter the effective thermal conductivity. In our storage design, the thermal throughput is enhanced by heat transfer structures, which can also handle potential structural changes of the reactive material. Heat conducting fins made from aluminum are chosen that were originally designed for latent thermal energy storages [35]. Thereby, a low conductivity of the porous bulk has a minor effect on the effective thermal conductivity of the fixed bed. Fig. 1 shows the storage module filled with the reactive material and wrapped by stainless steel filter fabric. When operated with SrBr_2 , the storage cells feature a specific storage density of approximately 75 kWh/m³.

Design of the storage module. In order to ensure tight thermal contact, the extruded axial fins are mounted with steel clips on the heat exchanger's central tube ($\varnothing 17.2 \times 2.3$ mm, stainless steel 1.4404), see Fig. 1b. In the largest compartment of the aluminum structure, the maximum distance between two surfaces is 10 mm. The fin fraction is 17 vol%,

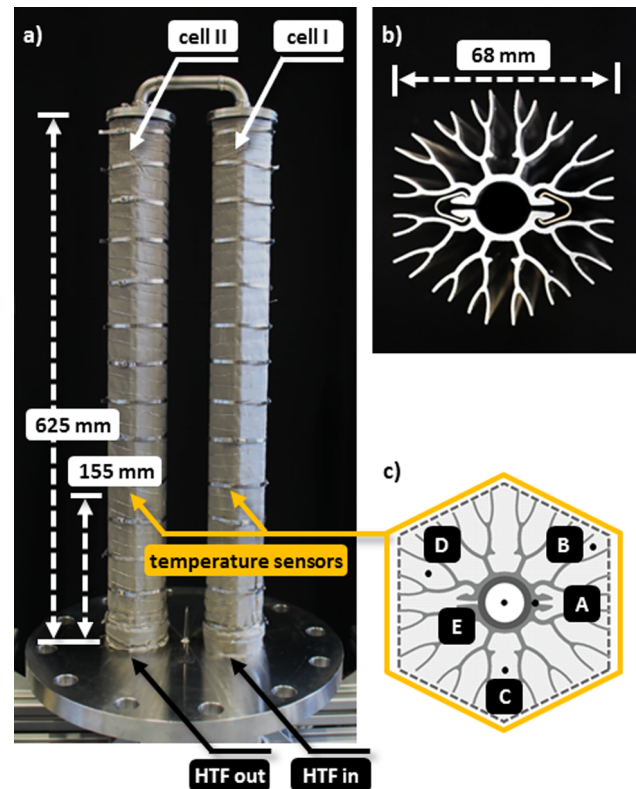


Fig. 1. Prototype of the scalable thermochemical storage module. (a) Lab-scale module consisting of two cells I and II, with in total 1.25 m of finned tube filled with 4.7 kg of the reactive material strontium bromide and wrapped with stainless steel filter tissue, (b) cross-section of the extruded aluminum fins prepared to be mounted on the heat transfer fluid (HTF) tube with steel clips, and (c) positions of the temperature sensors in the porous bulk (A–D) and in the HTF (E) at the height level indicated by the yellow arrows.

resulting in a void volume of 0.0033 m³/m tube length. The mass of the fins (aluminum 6060) is 1.915 kg/m. The spaces between the fins are filled with the granular storage material, and, to keep the packed bed in position, the finned tube is wrapped with two layers of metallic filter fabric (stainless steel 1.4404, mesh size 25 μm , specific weight 0.16 kg/m²). The geometry results in a specific filter area of 0.24 m²/m tube length. The lab-scale setup consists of 1.25 m of finned tube divided into two cells. The filter fabric is attached onto the fins by stainless steel cable ties and wire. Temperature sensors are mounted at four different positions within the solid bulk (Fig. 1c, positions A–D). They are placed symmetrically in the two cells. The heat transfer fluid temperatures are measured at the overall inlet and outlet of the storage module. In addition, there are temperature probes installed in the heat transfer fluid tube at the same height as the temperature sensors in the bulk phase (position E in Fig. 1c).

Reactive material. The bromide salt is commercially available in its hexahydrate phase (strontium bromide hexahydrate, 99% purity, particle size 0.2–1.25 mm; CAS 7789-53-9, abcr GmbH). It was dried at a temperature of 70 °C in order to obtain the monohydrate salt, which is easily pourable. By means of a funnel, the storage cells were filled from the top as evenly as possible. In total, the two storage cells contained a storage material mass of 5.059 kg monohydrate salt, corresponding to 3.772 kg anhydrous salt per meter of the storage cell. Based on a $\text{SrBr}_2 \cdot \text{H}_2\text{O}$ solid density of 3911 kg/m³, the effective bulk porosity is 0.68. As no literature data on the monohydrate's solid density was available from literature, this value is calculated from a linear interpolation between the known densities of $\text{SrBr}_2 \cdot 6\text{H}_2\text{O}$ (2386 kg/m³) and SrBr_2 (4216 kg/m³) [32]. Hence, when operated with SrBr_2 , the storage cells feature a specific storage density of approximately 75 kWh/m³ or 0.3 kWh/m cell length.

2.2. Performance characterization

Our characterization setup is designed for the investigation of steam-based thermochemical storage modules in the pressure range from 1 kPa to 0.6 MPa abs. and a maximum charging/discharging temperature of 320 °C (Fig. 2). It consists of four major components: the thermochemical storage module, the thermal infrastructure for operation with a heat transfer fluid (HTF), and two evaporator/condenser-units (E/C-units) for steam supply and condensation. A detailed flow scheme of the experimental setup can be found in Fig. 2a. From the HTF flow rate (\dot{m}_{HTF}) and heat capacity ($c_{p,\text{HTF}}$), and the temperature difference between inlet and outlet (ΔT_{HTF}), the effective thermal power P_{th} of the storage module is calculated. Steady-state thermal losses are considered in terms of the temperature difference ΔT_0 between the inlet and outlet of the HTF before the start of the experiment:

$$P_{\text{th}} = \dot{m}_{\text{HTF}} \cdot c_{p,\text{HTF}} \cdot (\Delta T_{\text{HTF}} - \Delta T_0). \quad (2)$$

The amount of water released or consumed by the reaction during the charging and discharging process, m_{Reaction} , is determined from the fluid level in the E/C-units, which is measured by an optical level indicator. Besides, the pressure-dependent mass of steam released to the dead volume of the pipework and the storage module (m_{Offset}) is accounted for in the calculation of the reaction conversion X :

$$X = \frac{m_{\text{Reaction}}(t) - m_{\text{Offset}}}{m_{\text{H}_2\text{O},\text{total}}}. \quad (3)$$

The total mass of steam required for full reaction conversion, $m_{\text{H}_2\text{O},\text{total}}$, is obtained from the amount of reactive material contained in the storage module.

Besides the determination of P_{th} from the heat transferred to the HTF, the thermal power P_X consumed or released by the chemical reaction is calculated from the reaction conversion based on the level measurement:

$$P_X = \frac{dX}{dt} \cdot Q_{\text{total}}, \quad (4)$$

with the total amount of energy Q_{total} being defined by the molar amount of storage material and the standard molar enthalpy of reaction:

$$Q_{\text{total}} = \frac{m_{\text{SrBr}_2\text{-H}_2\text{O}}}{M_{\text{SrBr}_2\text{-H}_2\text{O}}} \cdot \Delta H_R. \quad (5)$$

Conversely, the reaction conversion X_{th} is calculated from the thermal power P_{th} by integration:

$$X_{\text{th}} = \int_0^t \frac{P_{\text{th}}(t)}{Q_{\text{total}}} dt. \quad (6)$$

For typical operation parameters ($\dot{m}_{\text{HTF}} = 0.27 \text{ kg/s}$, 250 °C, $\Delta T = 1.0 \text{ K}$, $c_{p,\text{HTF}} = 2.66 \text{ k/(kg}\cdot\text{K)}$), the maximum error in the thermal power P_{th} is approximately $\pm 110 \text{ W}$ (relative error $\approx 10\text{--}20\%$), and is dominated by the error of the temperature measurement ($\pm 75 \text{ W}$). In contrast, the reaction conversion X can be determined with a relatively high accuracy of ± 0.02 for the smaller E/C-unit I (± 0.12 in case of E/C-unit II, which has a large ratio of fluid volume to level change). All relevant setup parameters, sensor specifications, and measurement uncertainties are given in Tables 1 and 2 in the Appendix A, as well as the details on the analysis of the maximum error propagation.

Before the start of every experiment, the storage module is preheated to the desired charging/discharging temperature until isothermal conditions are reached. Before the start of a hydration experiment, the storage module is evacuated to a pressure of approximately 0.5 kPa abs. to remove both residual water vapor as well as inert gases.

Design of the test setup. All steam-containing pipework of the setup (nominal diameter DN50) is equipped with a backing heater system to prevent condensation. A thermostat operated with thermal oil is used to introduce thermal energy into the reactive material for charging, and to discharge thermal power during the exothermic process. The E/C-units are built from tube bundle heat exchangers (heat transfer fluid (HTF) on shell-side); the fluid level is measured in a bypass tube. The two units differ in their diameter: the “smaller” unit (E/C-I) has a fluid volume to level change ratio of 1 ml/mm, whereas the “larger” unit (E/C-II) has a ratio of 10 ml/mm. Compared to E/C-I, unit E/C-II is designed for higher evaporation and condensation rates, and larger steam capacities. The pressure in the E/C-units is controlled by the HTF temperature on the shell-side of the heat exchanger. As soon as the ball valve between the E/C-unit and the storage module is opened, the chemical reaction starts. The charging/discharging process is regarded to be completed when the temperatures in the solid phase are constant. Afterwards, the ball valve is closed, and the E/C-unit is set to 25 °C in order to remove steam remaining in the pipework by condensation inside the E/C-unit.

Data acquisition and processing. The measurement data are recorded every 2 s. When calculating the amount of water released or consumed by the reaction from the fluid level, the temperature dependency of the liquid density is taken into account. As the level indicator shows noise due to condensation on the measurement rod in particular during the discharging experiments, the data on the reaction conversion X is smoothed with a 60-point moving average smoothing function before it is further processed. The same smoothing procedure is performed with the

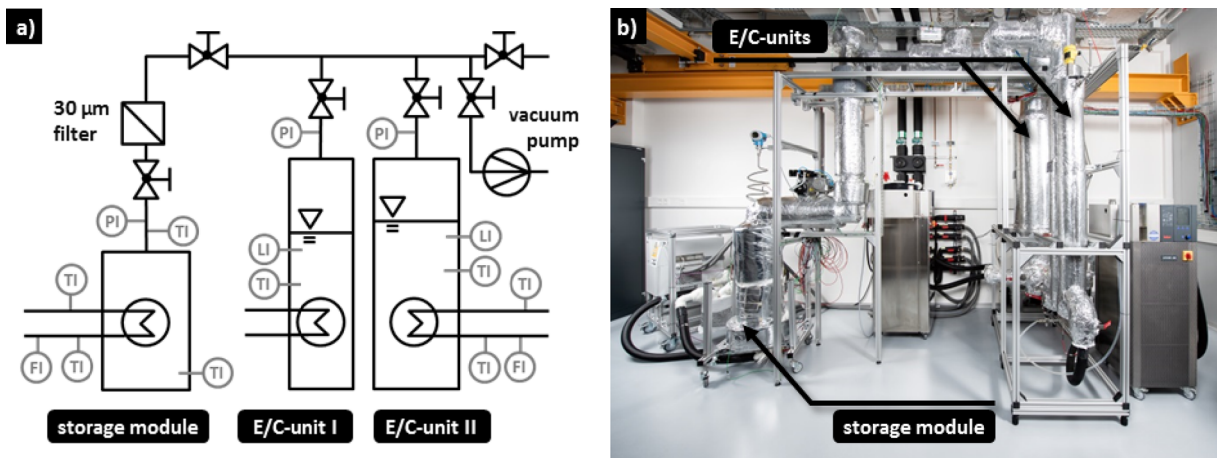


Fig. 2. Experimental setup with steam supply and thermal infrastructure. The evaporator/condenser-units (E/C-units, tube bundle heat exchangers) can be operated in a temperature range from 5 °C to 160 °C, and thus supply steam as reaction gas with pressures up to 0.6 MPa. A thermal oil circulation system serves as thermal infrastructure for the storage module and allows for running the thermochemical reaction at 320 °C maximum. (a) Flow scheme with measurement instrumentation (FI: flow indicator, LI: level indicator, PI: pressure indicator, TI: temperature indicator). (b) Photograph of the test rig ©German Aerospace Center (DLR).

thermal power curves P_{th} , with the exception of the thermal power P_x (120-points moving average smoothing due to higher noise level). Averaged power values (Fig. 5) are calculated for 0–50% reaction conversion (normalized to a value of 1 for every experiment). The dX/dt data points are averaged in the range from 10 to 50% of the normalized reaction conversion in order to avoid measurement artefacts caused by fluctuations of the liquid level right after the start of the experiment.

3. Results and discussion

A series of 34 charging/discharging experiments was performed under variation of several operation parameters (charging/discharging temperature, mass flow of HTF, condenser/evaporator temperature, E/C-unit I/II). Here, a selection of the results is presented, focusing on the investigation of different charging and discharging temperatures as well as the cycling performance. A summary of all discussed measurements is given in Table 3 (charging experiments) and Table 4 (discharging experiments) in the Appendix A.

3.1. “Isothermal” storage mode

First, we discuss the storage system performance when operating it with no effective gradient between the charging and the discharging temperature, i.e., when the steam pressure is adapted to compensate for the storage’s internal gradients necessary for heat transfer.

The results from an experiment with 231 °C charging temperature are given in Fig. 3a. At $t = 0$ min experimental time, the ball valve connecting the condenser and the storage module is opened to initiate the reaction, and the pressure in the storage module drops to approximately 5 kPa. As the endothermic dehydration reaction starts, the temperatures in the bulk

phase drop steeply to a minimum temperature of 187 °C. The overall time for fully charging the storage (i.e. the solid temperatures reach their start value) is approximately 40 min, with the temperatures in cell II showing a temporal delay of several minutes. We assume this to be caused by the axial temperature decrease in the HTF. This effect should be taken into account when designing the HTF infrastructure in case of upscaling.

The thermal power P_{th} transferred from the HTF reaches a peak value of 1 kW. Integration over the entire measurement time gives a total energy amount of 1283 kJ transferred from the HTF, which is equivalent to 94% of the energy amount required for full reaction conversion. This value closely agrees with the maximum reaction conversion calculated from the level measurement in the condenser, $X_{max} = 0.96$, which corresponds to full reaction conversion within the measurement accuracy. The thermal power P_x , which is derived from the rate of reaction dX/dt , indicates a similar trend within the experimental limitations.

The results of a corresponding discharging process at a HTF temperature of 231 °C are depicted in Fig. 3b. Before starting the hydration reaction, the storage module was evacuated to remove all remaining water vapor and inert gases. Afterwards, steam was supplied at a pressure of approximately 150 kPa. With the opening of the valve ($t = 0$ min), pressure rises rapidly and the exothermic reaction starts. After reaching a peak value of 252 °C, temperatures in the solid bulk phase start to fall again, and reach their initial value after approximately 60 min. The total transferred energy corresponds to 82% of the expected energy release, or 18% thermal losses, respectively. Therefore, the reaction conversion X_{th} calculated from the thermal power transferred to the HTF is normalized to a value of 1 in Fig. 3b for better comparison. The curve shows close agreement with the reaction conversion based on the water consumption from the evaporator’s reservoir, which indicates a good quality of the measurement data.

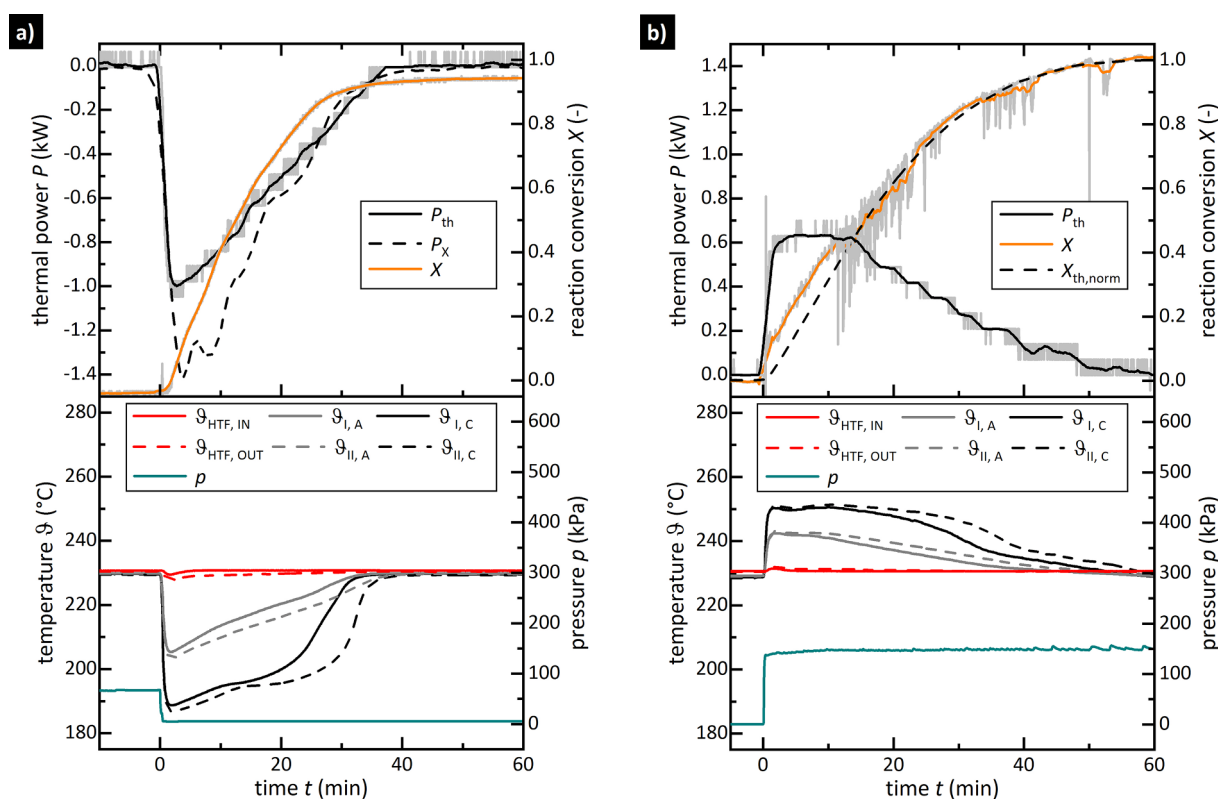


Fig. 3. Isothermal storage mode. The upper part of the panel contains the thermal power of the storage module and the conversion of the chemical reaction. The data on P_{th} and X are smoothed with a 60-points moving average smoothing function; the raw data are plotted in grey. In the lower panel, the temperature progression at different positions (right at the surface of the HTF tube (A), in the reactive bulk phase (C) of cell I and II) as well as the heat transfer fluid temperatures are plotted along with the pressure measured in the storage module. (a) Charging experiment at 231 °C HTF temperature and 5 kPa steam pressure. The upper part of the graph includes the thermal power P_x calculated from the rate of reaction dX/dt . (b) Discharging experiment with 231 °C HTF temperature and 150 kPa steam pressure. For comparison, the upper part of the graph includes the normalized reaction conversion $X_{th,norm}$, which is calculated from the thermal power P_{th} .

Summing up, the thermochemical storage module can be charged and discharged at a constant temperature of 231 °C. The internal temperature gradients occurring when heat is transferred between the HTF and the storage module can be fully compensated by increasing the pressure from 5 kPa to 150 kPa, therefore allowing for TES without any thermal downgrade of the stored energy.

3.2. "Thermal upgrade" storage mode

If the steam pressure difference between the charging and the discharging process is further increased, it is possible to over-compensate the internal gradient of the storage system, and, thus, to gain a positive effective overall temperature difference between the charging and the discharging temperature. Here, the minimum and maximum pressures are limited by the experimental setup (minimal condensation and maximum evaporation temperatures). In a later application, these limits will be given by the lowest available cooling temperature and the maximum steam pressure (e.g., supplied by waste heat or solar-thermal energy).

Lowering the steam pressure to 1 kPa allows reducing the charging temperature to 179 °C, which is demonstrated in the experiment displayed in Fig. 4a. The maximum thermal power P_{th} is reduced to approximately -270 W, which goes along with 4.5 h charging time. Again, the match with the "chemical" power $P_{X,av} = -250$ W is very close ($P_{X,av}$ is based on the mean effective reaction rate of $1.85 \cdot 10^{-4}$ 1/s, averaged over 10–50% of the maximum reaction conversion). However, integration of the thermal power P_{th} gives a total of only 846 kJ transferred from the HTF, which is equivalent to 62% of the expected value, while the reaction conversion based on the level measurement was 94% in this experiment. This indicates that the power measurement accuracy suffers for low absolute powers.

Fig. 4b displays the results of a hydration experiment performed with a discharging temperature of 281 °C and a steam pressure of 560 kPa. Noticeably, the temperatures measured in the reactive

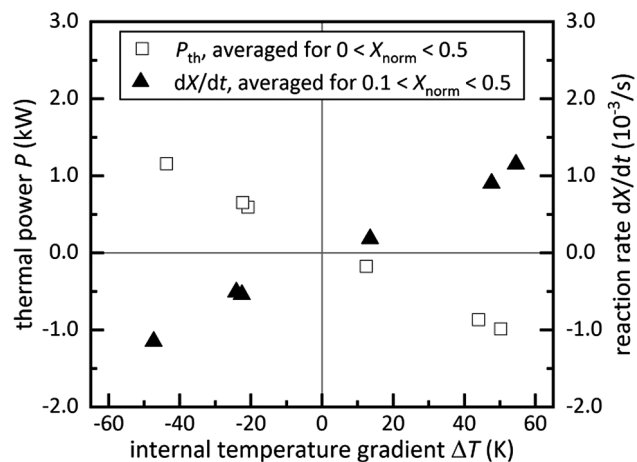


Fig. 5. Thermal performance characteristics of the storage module. The average thermal power P_{th} transferred from/to the HTF is plotted as a function of the maximum internal temperature difference occurring during the chemical reaction (left axis) and the corresponding effective rate of reaction dX/dt , which is derived from the reaction conversion calculated based on the level measurement (right axis). Each data point corresponds to one experiment from Figs. 3, 4 and 8 in the Appendix A. The dX/dt data from discharging experiments ($\Delta T < 0$ K) have been multiplied by -1 for a better overview. Both relevant performance indicators, thermal power and effective reaction rate, scale linearly with the maximum temperature difference between the HTF and the reactive bulk phase. Large internal temperature gradients enable a fast reaction with high thermal powers, but at the downside of reduced effective thermal upgrade.

material (position C) show a plateau at 30 min experimental time and 287 °C, before they further decrease and reach their initial values after approximately 50 min. However, this does not affect the overall

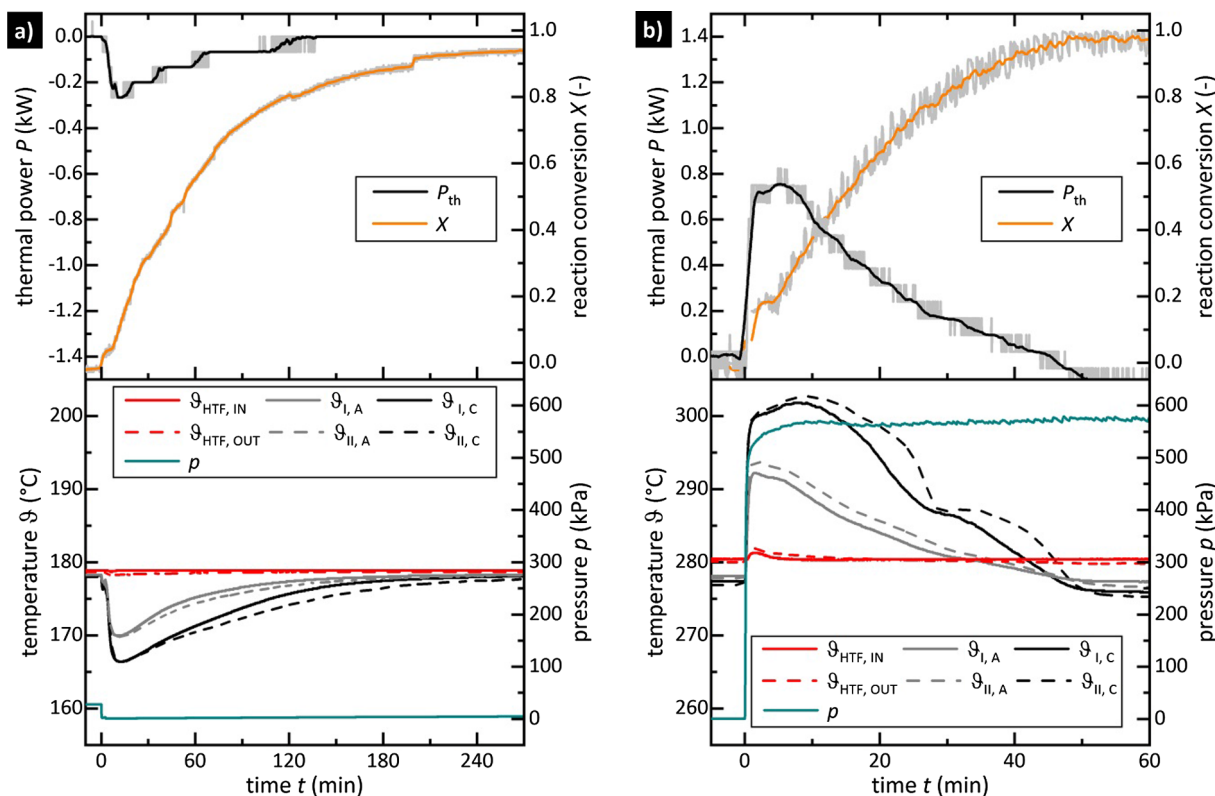


Fig. 4. Thermal upgrade storage mode. (a) Charging experiment at a minimum pressure of 1 kPa and 179 °C charging temperature. (b) Discharging experiment at maximum pressure of 560 kPa and 281 °C HTF temperature. Note that the temperature scales are shifted by a value of 100 K, which clearly illustrates the large thermal upgrade of 102 K for these operation parameters.

reaction or the thermal power transferred to the HTF. The thermal power reaches a maximum of 755 W, and the averaged power from start to 50% of the maximum reaction conversion is 650 W. Again, these numbers show close agreement with the “chemical” power calculated from the averaged reaction rate ($dX/dt_{\text{av}} = 5.1 \cdot 10^{-4}$ 1/s), which corresponds to a power of 695 W.

The experimental results demonstrate the vast operating range of the thermochemical energy storage. With the given experimental setup, an effective thermal upgrade of 102 K is achieved. We expect that in particular the discharging temperature can be further increased when steam can be supplied at higher pressures. On the other hand, we observed that the thermal power of the storage module correlates with the thermal gradient between the reactive solid and the heat transfer fluid. Therefore, we conclude that the storage can be discharged at lower pressures but the same discharging temperature (281 °C), but this will reduce the storage’s thermal power.

3.3. Key performance characteristics

In order to illustrate the relation between the thermal power and the potential thermal upgrade, which we consider as fundamental baseline for all application studies, we summarized all experiments into one master plot. In particular, the experimental series reveals that the thermal power of the storage module strongly depends on the internal gradient of the storage, i.e. the temperature difference between the temperature at which the chemical reaction is running (which is determined by the steam pressure) and the temperature of the HTF. From this, it follows that at constant pressure, higher thermal powers are reached when the charging temperature is increased, and the discharging temperature is decreased, respectively. The internal temperature gradient ΔT is assumed as the difference between the constant HTF

temperature and the minimum temperature in the reactive bulk measured during the endothermic process in case of charging experiments. For discharging, the temperature difference turns negative (constant discharge temperature minus maximum temperature in the reactive bulk).

In the analysis of the dependency of the thermal power on ΔT , we included additional experiments conducted with large internal temperature gradients (Fig. 8 in the Appendix A). The data points indicate a linear correlation (Fig. 5): large internal gradients lead to high thermal powers transferred to or from the HTF. The same effect is observed for the average rate of reaction, dX/dt . Note that the plot contains experimental data from a broad range of operation parameters, for example, steam pressure variations in the range from approximately 1 kPa to 560 kPa, which results in broadly varying conditions for steam mass transfer in the bulk phase. Therefore, from the clearly linear relationship between the internal temperature gradient and the storage’s thermal performance, we conclude that for the given storage design, the thermal power is limited by the effective heat transfer, and not by the steam mass transfer kinetics. With a similar argument, we exclude that the reaction kinetics determine the thermal performance of the storage, as no impact of the absolute temperature is seen in the results, even though the reaction rate is expected to be highly sensitive to both, temperature and steam pressure.

3.4. Cycling performance

While the already discussed operation temperatures, the specific thermal power, and the capacity of the storage module are the main features for the layout of industrial-scale TES, cycling stability is a mandatory prerequisite. Distinctive experiments with identical operation parameters were therefore repeated at the beginning and the end of the experimental series with a total of 34 charging/discharging cycles.

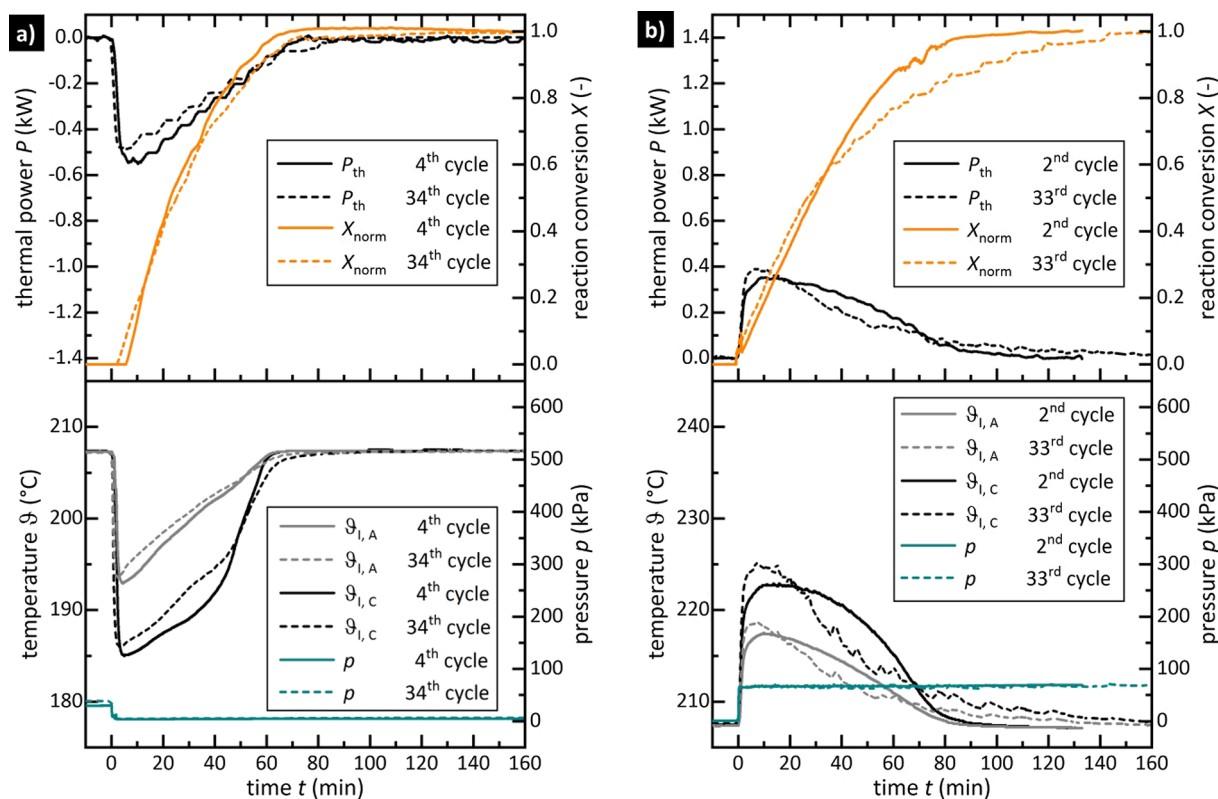


Fig. 6. Cycling performance. (a) Charging experiments with 208 °C HTF temperature and 5 kPa steam pressure. The plot compares results from the 4th and the 34th dehydration cycle. (b) Discharging experiment with 208 °C HTF temperature and 70 kPa steam pressure. The plot compares results of the 2nd and 33rd hydration cycle. In the later discharging experiment, the steam pressure was not perfectly constant, but it was observed to abruptly rise by approximately 10 kPa from time to time, which is considered an experimental artefact likely due to condensation in the setup. This led to a higher reaction temperature, which can also be observed as the “bumps” in the plotted temperature curves (33rd discharging cycle). For better comparison, the reaction conversion is normalized in these graphs.

Actually, a temporal delay is found when comparing the discharging process at the beginning and the end of the series (Fig. 6), with a short “overshoot” and then a longer “tail” of the reaction. However, and this is the important finding, no systematic degradation of the overall conversion or thermal power is found within the experimental measurement accuracy. E.g., we find an overall reaction conversion of 0.91 ± 0.12 and 0.81 ± 0.12 for the charging experiments (Fig. 6a, E/C unit II), and 1.02 ± 0.02 and 0.98 ± 0.02 for the discharging experiments (Fig. 6b, E/C unit I). In order to better understand the local effects causing the observed differences in the temperature curves, the storage cells were opened and the reactive bulk was investigated in more detail.

3.5. Macroscopic and microscopic particle morphology

After the 34 charging/discharging cycles, the storage module was cooled down to 70 °C, purged with ambient air, and opened. The filter tissue was intact, and there was no particle entrainment found in the pipework. Even though the stainless steel and also the aluminum surfaces darkened due to the thermal stress (maximum temperature of approximately 300 °C during the experimental series), no obvious corrosion effects were observed.

The two storage cells were opened by removing the filter tissue. The photographs in Fig. 7 show the top view onto the cross-section of a storage cell before (Fig. 7a) and after (Fig. 7d) the experimental study. The initially white crystals took a slightly brownish color. In both of the storage cells, the powder bed within the largest compartments of the aluminum fins had shrunk: the filling height in the four affected compartments was reduced by 55–80 mm. Even though at the top layer

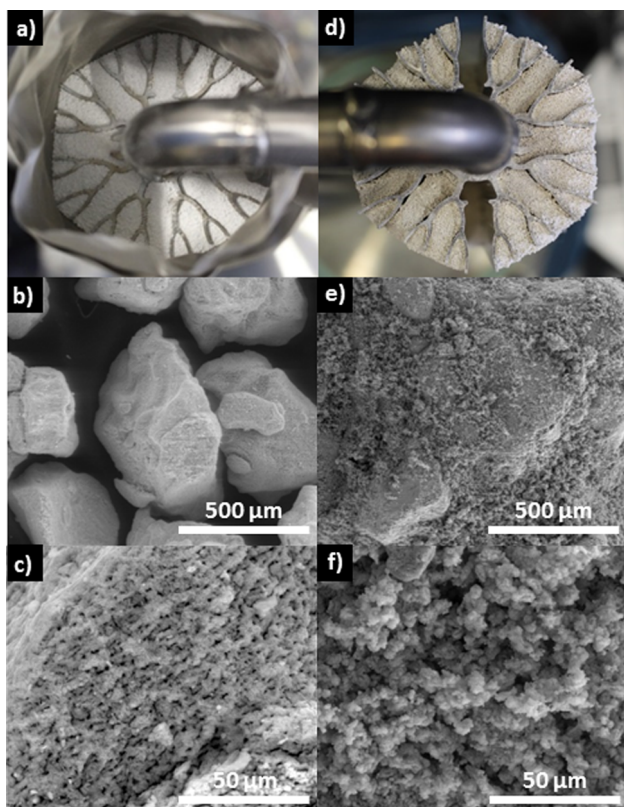


Fig. 7. Macroscopic and microscopic investigations of the bulk phase. (a) Storage cell filled with monohydrate salt before the start of the experimental series, (b and c) SEM images of the uncycled monohydrate granules. (d) Storage cell filled with monohydrate salt after 34 charging/discharging cycles, with the filter tissue completely removed. (e and f) SEM images of the agglomerated monohydrate phase obtained after 34 charging/discharging cycles. SEM images by courtesy of S. Afflerbach, University of Siegen.

of the solid bulk surface single loose particles can be seen, the bulk phase agglomerated into one large but apparently porous structure. Granules from the uncycled material and a fragment from the cycled agglomerates were analyzed by scanning electron microscopy (SEM, Fig. 7b, c and e, f).

In the large agglomerate, single primary granules can still be distinguished. Moreover, the surface of the now sintered particles appears more porous than the surface of the uncycled particles. From the SEM analysis we can confirm that the sintered solid structure is not dense, but still a permeable phase. We therefore conclude that the overall porosity remains on a similar level despite the sintering process, with only the typical size of particles and voids changing. Apart from that, we learned from the experimental series that the storage’s performance is not significantly affected by the altered bulk properties.

In Fig. 7d, several small gaps are visible between the bulk phase and the aluminum structure. This could lead to an additional heat transfer resistance between the solid phase and the aluminum fins, and thus be the root cause for the observed changes in the temperature profiles in Fig. 6b.

4. Conclusions

In this work, we present a thermochemical TES system that features an additional thermal upgrade of the stored energy along with high specific thermal powers, and the potential for large storage capacities due to its scalable design. This approach has a vast potential for implementation in industrial applications because it offers extreme flexibility in several aspects: The experimental study proves that the TES has a very large charging and discharging temperature range highly relevant for industrial processes (180–280 °C with strontium bromide (SrBr₂) and water vapor as reference thermochemical working pair). The hydration and dehydration reaction of the inorganic salt offers a high specific energy density of 291 kJ/kg (or 81 kWh/t), which is comparable to high-performance phase change materials in latent TES in a similar temperature range. For the storage module containing 4.7 kg of SrBr₂ (0.38 kWh capacity), thermal powers up to approximately 1.2 kW for charging and discharging have been demonstrated.

The dehydration and hydration reactions proceed along an equilibrium line, which means that the reaction temperatures can be adjusted by controlling the steam pressure. This effect can be used to perfectly match the charging and discharging temperatures to a specific storage application, even when those vary over time. Alternatively, this degree of freedom can be used to set an effectively larger temperature gradient between the storage material and the heat transfer fluid, which allows reducing the heat exchanger size without reducing the thermal power of the TES.

Our findings confirm that the thermal downgrade, which occurs in all TES systems due to the necessary heat transfers, can be compensated or even over-compensated by raising the discharging temperature, resulting in an effective thermal upgrade of the stored energy: the lab-scale storage module was charged at a minimum temperature of 179 °C, and discharged at a maximum temperature of 281 °C. This large effective thermal boost of more than 100 K is achieved by increasing the steam pressure from 1 kPa during the charging process to 560 kPa for discharging. For this purpose, it is necessary to supply water vapor as reaction gas to drive the exothermic discharging reaction, e.g. at temperatures at around 155 °C. The evaporation enthalpy could be provided by waste heat or solar-thermal energy. Depending on the application, the storage can either be operated as a batch system, or continuously with two alternating storage modules (e.g. for isothermal TES with high storage capacities or for TES with an effective thermal upgrade and large thermal powers, respectively).

The presented experiments reveal that for the given operation parameters, the storage’s thermal performance is determined by the heat transfer from the reactive material to the HTF or vice versa, and not by the reaction kinetics or the steam mass transport kinetics within the reactive bulk phase. Hence, although the physical processes during the charging and discharging phase are more complex in the thermochemical TES than in sensible or latent TES, the performance of the

thermochemical TES is controlled by heat transfer limitations, and therefore relatively easy to model. Also, the storage concept is not bound to the chosen reference material combination, and can be transferred to any other reaction system and temperature range, provided that the chemical reaction runs at a certain minimum rate. The chosen design of the storage module can easily be up-scaled to larger capacities and thermal powers, and, apart from that, existing optimization tools can be applied, e.g. for the improvement of the heat transfer structure in terms of enhanced thermal throughput.

Besides the performance characterization, we provide evidence for the cycle performance of the storage module: significant macroscopic changes in the reactive material were found to already occur during the first 34 charging/discharging cycles. One might expect them to have a major effect on the thermal performance of the storage (e.g. due to reduced steam mass transfer). However, the latter is not the case. We were able to demonstrate that these macroscopic changes actually do not affect the performance of the storage in the proposed design. This is a very important finding since it indicates the possibility to operate thermochemical materials (e.g. salt hydrates) without matrices, binders or any other technical means, which, on the one side, improve the material's applicability, but, on the other side, reduce the energy density and increase the material costs.

We thus lay down the necessary groundwork for the development of large-scale industrial TES modules. The demonstrated approach contributes to breaking the technological hurdle in the design of scalable high-performance thermochemical TES with combined temperature boost. This opens up new possibilities for TES applications to be industrially established, e.g. the waste-heat driven thermal upgrade of

process heat, and therefore can be a game changer in the efforts to increase energy efficiency in industrial processes.

CRediT authorship contribution statement

Jana Stengler: Data curation, Investigation, Methodology, Validation, Visualization, Writing - original draft. **Marc Linder:** Conceptualization, Funding acquisition, Supervision, Writing - review & editing.

Declaration of Competing Interest

The authors declare that they have no known competing financial interests or personal relationships that could have appeared to influence the work reported in this paper.

Acknowledgements

This research was partially funded by the German Federal Ministry for Economic Affairs and Energy (BMWi, "Bundesministerium für Wirtschaft und Energie"), "TheSan" project (03ET1297A). We gratefully acknowledge the support of Christian Brack, Torsten Ascher, Marius Drexler, Eva Fischer, and Moritz Wild during the conception, installation, and the commissioning of the test setup. Also, we thank Dr. Bernd Hachmann from F. W. Broekelmann Aluminiumwerk GmbH for providing the aluminum fins, and Dr. Sandra Afflerbach from the University of Siegen for providing the SEM images.

Appendix A

A.1. Experimental setup and measurement uncertainties

See [Tables 1 and 2](#).

Table 1
Setup specifications.

Parameter	Value	Uncertainty
E/C-I, ratio of fluid volume to level change	1.317 ml/mm	–
E/C-II, ratio of fluid volume to level change	10.364 ml/mm	–
dead volume of the storage vessel	0.036 m ³	± 0.001 m ³
SrBr ₂ ·H ₂ O mass contained in the storage	5.059 kg	± 0.001 kg

Table 2
Measurement equipment and uncertainties in the range of operation.

Sensor type	Instrument data	Measurement uncertainty
Temperature	Pt100, class A	± (0.15 °C + 0.002 θ/°C) ± 0.05 K digitization error
Pressure	piezo-resistive, Endress + Hauser, Cerabar S PMP71	± 0.025% full scale (0–600 kPa)
HTF mass flow	Coriolis, Wagner, RHM08	± 0.2% of the measured value
Fluid level	radar, Vega, VegaFlex 81	± 2 mm
Mass balance	electronic scale	± 0.001 kg

A.1.1. Propagation of measurement uncertainties

To estimate systematic errors, a propagation of measurement uncertainties was conducted for the thermal power P_{th} :

$$\Phi P_{th} = \left| \frac{\partial P_{th}}{\partial \dot{m}_{HTF}} \right| \Phi \dot{m}_{HTF} + \left| \frac{\partial P_{th}}{\partial c_{p,HTF}} \right| \Phi c_{p,HTF} + \left| \frac{\partial P_{th}}{\partial \Delta T} \right| \Phi \Delta T$$

It follows from Eq. (2):

$$\Phi P_{th} = c_{p,HTF} \cdot \Delta T \cdot \Phi \dot{m}_{HTF} + \dot{m}_{HTF} \cdot \Delta T \cdot \Phi c_{p,HTF} + \dot{m}_{HTF} \cdot c_{p,HTF} \cdot \Phi \Delta T$$

It is assumed that the heat capacity of the heat transfer fluid (*Purity FG Heat Transfer Fluid*), $c_{p,HTF}$, which is interpolated from the manufacturer's datasheet in the range of 150–320 °C, has an uncertainty of 5%. For typical operation parameters ($\dot{m}_{HTF} = 0.27$ kg/s, 250 °C, $\Delta T = 1.0$ K, $c_{p,HTF} = 2.66$ k/(kg·K)) and measurement uncertainties as given in Table 2, the error propagation results in ± 110 W maximal error, which corresponds to a relative uncertainty of $\pm 16\%$ in the determination of the thermal power. This error is primarily determined by the temperature measurement uncertainty (± 75 W), followed by the uncertainty of the HTF's heat capacity.

Correspondingly, a propagation of measurement uncertainties was conducted for the reaction conversion X :

$$\Phi X = \left| \frac{\partial X}{\partial m_{\text{Reaction}}} \right| \Phi m_{\text{Reaction}} + \left| \frac{\partial X}{\partial m_{\text{Offset}}} \right| \Phi m_{\text{Offset}} + \left| \frac{\partial X}{\partial m_{\text{H}_2\text{O}}} \right| \Phi m_{\text{H}_2\text{O}}$$

and with Eq. (3):

$$\Phi X = \frac{\Phi m_{\text{Reaction}}}{m_{\text{H}_2\text{O}}} + \frac{\Phi m_{\text{Offset}}}{m_{\text{H}_2\text{O}}} + X \cdot \frac{\Phi m_{\text{H}_2\text{O}}}{m_{\text{H}_2\text{O}}}$$

The different error terms were calculated for typical operation conditions and setup parameters given in Tables 1 and 2. It was assumed that the temperature measurement uncertainty causes an error in the determination of both the fluid density as well as the gas density, but that the temperature-dependent density correlations itself do not have any uncertainties (fluid density based on correlation in VDI heat atlas, chapter D3 [36], gas density based on ideal gas properties). The total error in the reaction conversion is determined by the following errors:

$$\begin{aligned} \Phi m_{\text{Reaction, E/C-unit I}} &= \pm 5.3 \text{ g} && (\text{E/C-unit I, } 25 \text{ }^\circ\text{C condenser temperature}) \\ \Phi m_{\text{Reaction, E/C-unit II}} &= \pm 41.4 \text{ g} && (\text{E/C-unit II, } 25 \text{ }^\circ\text{C condenser temperature}) \\ \Phi m_{\text{Offset}} &= \pm 0.5 \text{ g} && (\text{gas properties at } 200 \text{ }^\circ\text{C and } 100 \text{ kPa}) \\ \Phi m_{\text{H}_2\text{O,total}} &= \pm 0.1 \text{ g} \end{aligned}$$

For the smaller E/C-unit I, this results in a maximum error of $\Phi X_{\text{E/C-unit I}} = \pm 0.02$. For the larger E/C-unit II, the maximum error propagation results in an error of $\Phi X_{\text{E/C-unit II}} = \pm 0.12$. It is mainly determined by the large fluid volume/level change-ratio of the vessel geometry, and thus the high uncertainty of the fluid level measurement in E/C-unit II.

A.2. Additional experimental data and summary

A.2.1. Charging and discharging with large internal temperature gradients

See Fig. 8.

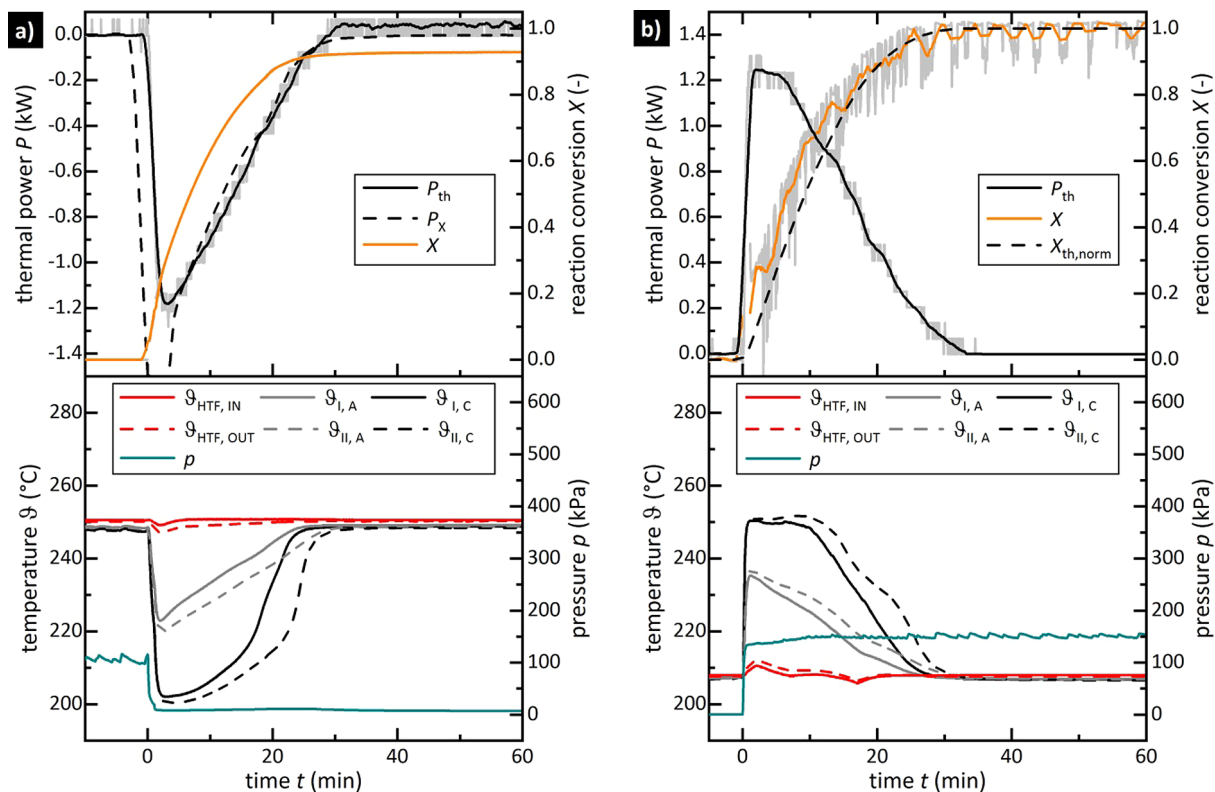


Fig. 8. Charging and discharging with large internal temperature gradients. (a) Charging experiment at 251 °C HTF temperature and 10 kPa steam pressure. The upper part of the graph also includes the thermal power P_x , which is calculated from the rate of reaction dX/dt . (b) Discharging experiment with 208 °C HTF temperature and 150 kPa steam pressure. For comparison, the upper part of the graph includes the normalized reaction conversion $X_{th, norm}$, which is calculated from the thermal power P_{th} .

A.2.2. Summary of discussed experimental data

See Tables 3 and 4.

Table 3

Summary of discussed charging experiments. The parameter T_{charge} corresponds to the constant HTF temperature before the start of experiment; T_{cond} is the temperature measured in the condenser's water reservoir. The given thermal power $P_{\text{th,av}}$ and reaction rate dX/dt_{av} are averaged in the range of 0–50% and, respectively, 10–50% of the maximum achieved reaction conversion.

T_{charge} °C	$p_{\text{H}_2\text{O}}$ kPa	T_{cond} °C	\dot{m}_{HTF} kg/min	E/C-unit	X_{max}	X_{th}	$P_{\text{th,av}}$ W	dX/dt_{av} $10^{-3}/\text{s}$	$T_{\text{solid,min}}$ °C	ΔT_{max} K	cycle no.	Fig.
207.9	5	25.3	0.240	II	0.91	0.87	−413	0.320	185.2	22.7	4	5
178.9	1	5.4	0.275	II	0.94	0.62	−177	0.185	166.4	12.5	11	4, 6
250.6	10	25.3	0.269	I	0.93	0.77	−987	1.150	200.3	50.3	22	8, 6
230.7	5	25.3	0.270	II	0.96	0.94	−867	0.905	186.7	44.0	25	3, 6
208.0	4	25.3	0.241	II	0.81	0.97	−465	0.389	183.7	24.3	34	5

Table 4

Summary of discussed discharging experiments. The parameter $T_{\text{disch.}}$ corresponds to the constant HTF temperature before the start of experiment; T_{evap} is the temperature measured in the evaporator's water reservoir. The given thermal power $P_{\text{th,av}}$ and reaction rate dX/dt_{av} are averaged in the range of 0–50% and, respectively, 10–50% of the maximum achieved reaction conversion.

$T_{\text{disch.}}$ °C	$p_{\text{H}_2\text{O}}$ kPa	T_{evap} °C	\dot{m}_{HTF} kg/min	E/C-unit	X_{max}	X_{th}	$P_{\text{th,av}}$ W	dX/dt_{av} $10^{-3}/\text{s}$	$T_{\text{solid,max}}$ °C	ΔT_{max} K	cycle no.	Fig.
207.9	67	90.4	0.118	I	1.02	0.89	318	0.313	223.8	−15.9	2	5
230.7	146	112.5	0.270	I	1.02	0.82	593	0.541	251.5	−20.8	13	3, 6
208.0	147	112.5	0.273	I	1.01	0.93	1156	1.150	251.7	−43.7	17	8, 6
280.5	561	157.7	0.264	I	0.98	0.67	650	0.506	302.7	−22.2	29	4, 6
208.0	66	90.4	0.117	I	0.98	0.90	345	0.275	226.4	−18.4	33	5

References

- Naegler T, Simon S, Klein M, Gils HC. Quantification of the European industrial heat demand by branch and temperature level. *Int J Energy Res* 2015;39:2019–30. <https://doi.org/10.1002/er.3436>.
- Papapetrou M, Kosmadakis G, Cipollina A, La Commare U, Micale G. Industrial waste heat: Estimation of the technically available resource in the EU per industrial sector, temperature level and country. *Appl Therm Eng* 2018;138:207–16. <https://doi.org/10.1016/J.APPLTHERMALENG.2018.04.043>.
- Brückner S, Liu S, Miró L, Radspieler M, Cabeza LF, Lävemann E. Industrial waste heat recovery technologies: An economic analysis of heat transformation technologies. *Appl Energy* 2015;151:157–67. <https://doi.org/10.1016/J.APENERGY.2015.01.147>.
- Chan CW, Ling-Chin J, Roskilly AP. A review of chemical heat pumps, thermodynamic cycles and thermal energy storage technologies for low grade heat utilisation. *Appl Therm Eng* 2013;50:1257–73. <https://doi.org/10.1016/J.APPLTHERMALENG.2012.06.041>.
- Spoelstra S, Haije WG, Dijkstra JW. Techno-economic feasibility of high-temperature high-lift chemical heat pumps for upgrading industrial waste heat. *Appl Therm Eng* 2002;22:1619–30. [https://doi.org/10.1016/S1359-4311\(02\)00077-7](https://doi.org/10.1016/S1359-4311(02)00077-7).
- Yu Y, Zhang P, Wu J, Wang R. Energy upgrading by solid-gas reaction heat transformer: A critical review. *Renew Sustain Energy Rev* 2008;12:1302–24. <https://doi.org/10.1016/j.rser.2007.01.010>.
- Wongsuwan W, Kumar S, Neveu P, Meunier F. A review of chemical heat pump technology and applications. *Appl Therm Eng* 2001;21:1489–519. [https://doi.org/10.1016/S1359-4311\(01\)00022-9](https://doi.org/10.1016/S1359-4311(01)00022-9).
- Richter M, Habermann E-M, Siebecke E, Linder M. A systematic screening of salt hydrates as materials for a thermochemical heat transformer. *Thermochim Acta* 2018;659:136–50. <https://doi.org/10.1016/j.tca.2017.06.011>.
- Afflerbach S, Trettin R. A systematic screening approach for new materials for thermochemical energy storage and conversion based on the Strunz mineral classification system. *Thermochim Acta* 2019;674:82–94. <https://doi.org/10.1016/J.TCA.2019.02.010>.
- Ishitobi H, Uruma K, Takeuchi M, Ryu J, Kato Y. Dehydration and hydration behavior of metal-salt-modified materials for chemical heat pumps. *Appl Therm Eng* 2013;50:1639–44. <https://doi.org/10.1016/j.applthermaleng.2011.07.020>.
- Knoll C, Müller D, Artner W, Welch JM, Werner A, Harasek M, et al. Probing cycle stability and reversibility in thermochemical energy storage – CaC₂O₄H₂O as perfect match? *Appl Energy* 2017;187:1–9. <https://doi.org/10.1016/j.apenergy.2016.11.053>.
- N'Tsoukpoe KE, Schmidt T, Rammelberg HU, Watts BA, Ruck WKL. A systematic multi-step screening of numerous salt hydrates for low temperature thermochemical energy storage. *Appl Energy* 2014;124:1–16. <https://doi.org/10.1016/j.apenergy.2014.02.053>.
- Donkers PAJ, Sögütoglu LC, Huinink HP, Fischer HR, Adan OCG. A review of salt hydrates for seasonal heat storage in domestic applications. *Appl Energy* 2017;199:45–68. <https://doi.org/10.1016/J.APENERGY.2017.04.080>.
- Cot-Gores J, Castell A, Cabeza LF. Thermochemical energy storage and conversion: A-state-of-the-art review of the experimental research under practical conditions. *Renew Sustain Energy Rev* 2012;16:5207–24. <https://doi.org/10.1016/j.rser.2012.04.007>.
- Willers E, Groll M. Two-stage metal hydride heat transformer. *Int J Hydrogen Energy* 1999;24:269–76. [https://doi.org/10.1016/S0360-3199\(98\)00058-5](https://doi.org/10.1016/S0360-3199(98)00058-5).
- Richter M, Bouché M, Linder M. Heat transformation based on CaCl₂/H₂O – Part A: Closed operation principle. *Appl Therm Eng* 2016;102:615–21. <https://doi.org/10.1016/j.applthermaleng.2016.03.076>.
- van der Pal M, Critoph RE. Performance of CaCl₂-reactor for application in ammonia-salt based thermal transformers. *Appl Therm Eng* 2017;126:518–24. <https://doi.org/10.1016/j.applthermaleng.2017.07.086>.
- Wu S, Li TX, Yan T, Wang RZ. Experimental investigation on a novel solid-gas thermochemical sorption heat transformer for energy upgrade with a large temperature lift. *Energy Convers Manag* 2017;148:330–8. <https://doi.org/10.1016/J.ENCONMAN.2017.05.041>.
- Sharma A, Tyagi VV, Chen CR, Buddhi D. Review on thermal energy storage with phase change materials and applications. *Renew Sustain Energy Rev* 2009;13:318–45. <https://doi.org/10.1016/J.RSER.2007.10.005>.
- Cabeza LF, Sole C, Castell A, Oro E, Gil A. Review of solar thermal storage techniques and associated heat transfer technologies. *Proc IEEE* 2012;100:525–38. <https://doi.org/10.1109/JPROC.2011.2157883>.
- Laing D, Bauer T, Breidenbach N, Hachmann B, Johnson M. Development of high temperature phase-change-material storages. *Appl Energy* 2013;109:497–504. <https://doi.org/10.1016/J.APENERGY.2012.11.063>.
- Khodadadi JM, Hosseinizadeh SF. Nanoparticle-enhanced phase change materials (NEPCM) with great potential for improved thermal energy storage. *Int Commun Heat Mass Transf* 2007;34:534–43. <https://doi.org/10.1016/J.ICHEATMASSTRANSFER.2007.02.005>.
- Lin Y, Jia Y, Alva G, Fang G. Review on thermal conductivity enhancement, thermal properties and applications of phase change materials in thermal energy storage. *Renew Sustain Energy Rev* 2018;82:2730–42. <https://doi.org/10.1016/J.RSER.2017.10.002>.
- Milián YE, Gutiérrez A, Grágeda M, Ushak S. A review on encapsulation techniques for inorganic phase change materials and the influence on their thermophysical properties. *Renew Sustain Energy Rev* 2017;73:983–99. <https://doi.org/10.1016/J.RSER.2017.01.159>.
- Dhaidan NS, Khodadadi JM. Improved performance of latent heat energy storage systems utilizing high thermal conductivity fins: A review. *J Renew Sustain Energy* 2017;9:034103. <https://doi.org/10.1063/1.4989738>.
- Tao YB, He Y-L. A review of phase change material and performance enhancement method for latent heat storage system. *Renew Sustain Energy Rev* 2018;93:245–59. <https://doi.org/10.1016/J.RSER.2018.05.028>.
- Mauran S, Lahmidi H, Goetz V. Solar heating and cooling by a thermochemical process. First experiments of a prototype storing 60 kW h by a solid/gas reaction. *Sol Energy* 2008;82:623–36. <https://doi.org/10.1016/j.solener.2008.01.002>.

- [28] Michel B, Mazet N, Neveu P. Experimental investigation of an innovative thermochemical process operating with a hydrate salt and moist air for thermal storage of solar energy: Global performance. *Appl Energy* 2014;129:177–86. <https://doi.org/10.1016/j.apenergy.2014.04.073>.
- [29] Fopah-Lele A, Tamba JG. A review on the use of SrBr 2·6H₂O as a potential material for low temperature energy storage systems and building applications. *Sol Energy Mater Sol Cells* 2017;164:175–87. <https://doi.org/10.1016/j.solmat.2017.02.018>.
- [30] Stengler J, Weiss J, Linder M. Analysis of a lab-scale heat transformation demonstrator based on a gas-solid reaction. *Energies* 2019;12:2234. <https://doi.org/10.3390/en12122234>.
- [31] Wagman DD, Evans WH, Parker VB, Schumm RH, Halow I, Bailey SM, et al. The NBS tables of chemical thermodynamic properties. Selected values for inorganic and C1 and C2 organic substances in SI units. *J Phys Chem Ref Data* 1982;11.
- [32] Perry DL. *Handbook of inorganic compounds*. 2nd ed. Boca Raton (USA): Taylor & Francis Group; 2011. <https://doi.org/10.1201/b10908>.
- [33] Maldonado J, Fullana-Puig M, Martín M, Solé A, Fernández Á, de Gracia A, et al. Phase change material selection for thermal energy storage at high temperature range between 210 °C and 270 °C. *Energies* 2018;11:861. <https://doi.org/10.3390/en11040861>.
- [34] Lele AF, N'Tsoukpoe KE, Osterland T, Kuznik F, Ruck WKL. Thermal conductivity measurement of thermochemical storage materials. *Appl Therm Eng* 2015;89:916–26. <https://doi.org/10.1016/j.applthermaleng.2015.06.077>.
- [35] Johnson M, Vogel J, Hempel M, Hachmann B, Dengel A. Design of high temperature thermal energy storage for high power levels. *Sustain Cities Soc* 2017;35:758–63. <https://doi.org/10.1016/j.scs.2017.09.007>.
- [36] VDI e.V. editor. *VDI-Wärmeatlas* 11th ed. Berlin, Heidelberg: Springer Vieweg; 2013. <https://doi.org/10.1007/978-3-642-19981-3>.

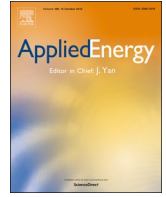
2.2 Paper II: Proof-of-concept

2 Publications

2.3 Paper III: Material characterization

This article was published in *Applied Energy*, 277, 115432,
Copyright Elsevier (2020).

<https://www.sciencedirect.com/science/article/abs/pii/S0306261920309442>



Thermodynamic and kinetic investigations of the SrBr₂ hydration and dehydration reactions for thermochemical energy storage and heat transformation

Jana Stengler*, Inga Bürger, Marc Linder

Institute of Engineering Thermodynamics, German Aerospace Center (DLR), Pfaffenwaldring 38-40, 70569 Stuttgart, Germany



HIGHLIGHTS

- SrBr₂/H₂O charging/discharging temperatures and reaction rates investigated.
- Experimental data from thermogravimetric analysis and lab-scale setup.
- Empirical rate models experimentally validated for 0–97 kPa, 150–210 °C.
- Cycle stability determined over 100 hydration/dehydration cycles.
- Crucial parameters for storage design and application feasibility studies given.

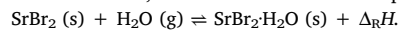
ARTICLE INFO

Keywords:

Thermochemical energy storage
Heat transformation
Strontium bromide
Thermodynamic equilibrium
Thermal hysteresis
Gas–solid reaction kinetics

ABSTRACT

The potential of thermochemical energy storage and heat transformation has been soundly highlighted in literature. For applications in the temperature range from approximately 150 °C to 300 °C, the inorganic salt strontium bromide, which reacts with water vapor in an exothermic reaction, is a promising candidate:



This chemical reaction offers a specific energy density of 291 kJ/kg SrBr₂ (or 81 kWh/t). The feasibility of a thermochemical energy storage and heat transformer based on the SrBr₂/H₂O working pair has already been successfully demonstrated on a 1 kW scale in a lab-scale storage unit. Here, we report on the steam pressure-dependent reaction temperatures of the dehydration and hydration reactions as well as the reaction rate and the cycle stability of the reactive system over 100 reaction cycles using thermogravimetric analysis. For distinct operating points, e.g. running the hydration reaction at 180 °C and 69 kPa, specific thermal powers up to 4 kW/kg SrBr₂ were experimentally determined. Running the dehydration reaction at 210 °C and 5 kPa steam pressure showed specific thermal powers of 2.5 kW/kg of SrBr₂·H₂O, thus proving the suitability of SrBr₂/H₂O as thermochemical working pair for high-power storage applications. Our results provide fundamental material-related data for the design of high-power reactor modules as well as for numerical studies on the potential of thermochemical energy storage and heat transformation based on SrBr₂/H₂O.

1. Introduction

The potential of thermochemical energy storage and heat transformation to increase the energy efficiency in industrial processes, and thereby to reduce the carbon footprint, is widely discussed in literature [1,2,3]. Various types of thermochemical working pairs are investigated for a wide range of operating temperatures, many of them based on gas–solid reactions. Several material screening studies focus on the criteria which gas–solid reactions need to fulfill in order to be

suitable candidates for thermochemical energy storage [4,5] and heat transformation applications in particular [6,7]. In short, the most relevant criteria for industrial applications are summarized as follows:

- reversible and cycle-stable reaction in the relevant temperature range,
- sufficient specific energy storage density (kWh/kg),
- high effective reaction rates which allow for large specific thermal powers (kW/kg),

* Corresponding author.

E-mail address: jana.stengler@dlr.de (J. Stengler).

<https://doi.org/10.1016/j.apenergy.2020.115432>

Received 9 February 2020; Received in revised form 3 June 2020; Accepted 24 June 2020

0306-2619/© 2020 Elsevier Ltd. All rights reserved.

Nomenclature*Greek letters*

ν	stoichiometric coefficient
ϑ	temperature, °C

Latin letters

A_0	pre-exponential factor, 1/s
$\Delta_R G$	Gibbs enthalpy of reaction, kJ/mol
$\Delta_R H^0$	standard molar enthalpy of reaction, kJ/mol
$\Delta_R S^0$	standard molar entropy of reaction, J/(mol·K)
E_a	activation energy, kJ/mol
$f(X)$	reaction model function
$h(p)$	pressure term
k	rate coefficient, 1/s
$k(T)$	Arrhenius term, 1/s
K_{fit}	reaction rate coefficient, 1/s
K_{eq}	equilibrium constant
m	mass, kg
n	pressure term exponent
p	pressure, kPa
p^0	reference pressure, kPa

R	universal gas constant, 8.314 J/(mol·K)
R^2	coefficient of determination
t	time, s
T	absolute temperature, K
X	reaction conversion

Indices

0	standard conditions for temperature and pressure (273.15 K, 1 atm)
dehyd	dehydration
eff	effective
exp	experimental
g	gas
hyd	hydration
norm	normalized
s	solid

Abbreviations

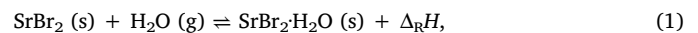
DSC	differential scanning calorimetry
HTF	heat transfer fluid
TG	thermogravimetric
TGA	thermogravimetric analysis

- no side reactions, thermal decomposition or melting,
- non-toxic materials and commercial availability.

A promising candidate is the inorganic salt strontium bromide. The dehydration reaction of strontium bromide hexahydrate to the monohydrate was discussed in several studies, e.g. by N'Tsoukpoe et al. [8] for thermal energy storage applications below 105 °C. Michel et al. investigated the monohydrate-hexahydrate reaction in an experimental study with a packed bed reactor operated with 400 kg hydrated salt, and reported thermal powers in the range from 0.75 to 2 W/kg [9]. Besides their experimental studies, the authors developed a two-dimensional model for a rectangular module of the thermochemical storage reactor operated at temperatures below 100 °C [10]. The reaction rates were assumed to depend on the reaction advancement and on the distance from the thermodynamic equilibrium, and a first-order kinetic law was chosen. A more detailed reaction rate model for the hydration reaction from the monohydrate to the hexahydrate form was developed by Esaki et al. for maximum operation temperatures of 80 °C [11]. In another experimental study, a composite material based on strontium bromide hexahydrate and natural graphite was investigated by Cammarata et al. [12]. The authors report an improvement of the hydration reaction progression due to an increased thermal conductivity and a reduced thermal hysteresis. However, no investigation on the cycle stability of the composite material was conducted. Same as in the studies referenced above, this thermochemical system addresses domestic applications with a maximum storage temperature of 100 °C. A possible show stopper in these low-temperature storage applications are the relatively high specific material costs of strontium bromide, since especially seasonal storage applications require high storage capacities. Nevertheless, the production process of strontium bromide on a large industrial scale is not yet optimized and costs may reduce drastically with increasing usage. This issue is addressed by Gilles et al. [13]. The authors investigate an alternative and cost-efficient synthesis pathway to reduce production costs, and also discuss the carbon footprint of strontium bromide when used for low temperature energy storage (< 100 °C).

In contrast, operating a thermochemical reactor with the reacting couple SrBr₂·H₂O at higher temperatures (> 150 °C) and high specific thermal powers has not been in the spotlight of research yet. This is

possible by selecting the thermochemical reaction from the anhydrous phase to the monohydrate,



instead of mono- to hexahydrate. This reaction is listed in a database on salt hydrate pairs by Glasser [14], and thermodynamic data is given with $\Delta_R H^0 = 72.8$ kJ/mol and $\Delta_R S^0 = 152$ J/(mol·K) ($p^0 = 27.4$ Torr, $T^0 = 298$ K). Based on the standard enthalpy and entropy of formation given in the NBS Tables [15], the reaction enthalpy and entropy are 71.98 kJ/mol and 143.93 J/(mol·K), respectively ($p^0 = 0.1$ MPa, $T^0 = 298$ K), which are the values we refer to in the present work. The reaction was identified as a potential candidate for thermochemical heat transformation applications in a previous study by our research group [6]. We found the reaction to be reversible, however, a thermal reaction hysteresis was observed in thermogravimetric analysis (TGA) experiments: at a water vapor partial pressure of 5 kPa, a difference of 22 K between the hydration and dehydration temperatures was found. For 10 dehydration/hydration reactions, cycle-stability was experimentally confirmed. Based on these screening results, we investigated the hydration reaction of strontium bromide on a 1 kg scale [16]. This work led to an experimental proof-of-concept for thermochemical heat transformation with 102 K thermal upgrade and a maximum discharge temperature of 280 °C in a 1 kW lab-scale prototype [17]. During the discharging process, the specific thermal power of the storage module was observed to slightly decrease with increasing discharge temperature and constant steam pressure. In addition, the granular storage material was found to have agglomerated into larger porous structures, thus raising questions on the cycle stability of the chemical reaction.

Therefore, to further clarify the qualification of the SrBr₂/H₂O working pair for industrial energy storage and heat transformation applications in the temperature range from approximately 150–300 °C (e.g. waste heat recovery from batch processes in chemical industries), in this work we present a detailed analysis of its cycle stability and thermodynamic and kinetic properties.

2. Experimental methods and data analysis

Two different experimental methods were applied in the presented study: firstly, thermogravimetric analyses with samples on a 15 mg

scale, and secondly, investigations with a lab-scale test setup with sample masses of around 1 kg of $\text{SrBr}_2\cdot\text{H}_2\text{O}$.

2.1. Sample preparation

Strontium bromide was supplied in the form of hexahydrate crystals (strontium bromide hexahydrate, 99%, CAS 7789-53-9, particle size: 0.2–1.25 mm, abcr GmbH). The hexahydrate phase melts at a temperature of 89 °C [18], and therefore was dried in a circulating air oven at 70 °C for several hours to obtain the monohydrate form, $\text{SrBr}_2\cdot\text{H}_2\text{O}$. Full decomposition from the hexahydrate to the monohydrate phase was assured by recording the mass loss. The monohydrate samples were then preserved at 70–110 °C until they were investigated with the experimental methods described in the following.

2.2. Thermogravimetric analysis (TGA)

For the kinetic and cycling investigations on milligram scale, two different commercial TGA setups were used: a NETZSCH STA 449C *Jupiter*[®], equipped with a water vapor furnace and a steam generator (aDROP by *Bronkhorst*), and, a NETZSCH STA 449F3 equipped with a humidity generator (MHG32 by ProUmid) and humidity sensor. The two devices mainly differ in the manner of vapor generation and, thereby, in their operation range in respect to the available water vapor partial pressure.

In both devices, a dry flow of nitrogen was used as purge and protective gas. To set the desired vapor partial pressure, the purge gas flow was mixed with water vapor (constant total volumetric flow of 100 ml/min). The volumetric flow of nitrogen used as protective gas stayed at a constant level, and is not considered in the calculation of the water vapor partial pressure (STA 449C: 50 ml/min, STA 449F: 20 ml/min). The TGA devices operate at ambient conditions, and we assumed the ambient pressure to be at a constant value of 97 kPa. In the case of the STA 449C, the resulting water vapor partial pressure was calculated from the set nitrogen volume flow and water mass flow (maximum error $\pm 0.5\text{--}1$ kPa). In case of the STA 449F, humidity data were obtained from the humidity sensor located right before the gas inlet to the sample chamber. Assuming a humidity sensor measurement accuracy of 2%, and an error in the temperature measurement in the evaporator chamber (Pt100, ± 1 K) contributing to the maximum error propagation, this results in a maximum error of 1.3 kPa for typical operation conditions (85 °C evaporator temperature, 5 kPa water vapor partial pressure). A TGA sample mass of 15 ± 1 mg and platinum/rhodium crucibles (STA 449F3, DSC sample carrier with thermocouple Type K, measurement accuracy ± 1 K) or alumina crucibles (STA 449C, TG sample carrier with thermocouple Type S, measurement accuracy ± 1 K) were chosen. The sampling rate was set to 60 points per minute. To reduce noise, all TGA data were smoothed using the NETZSCH *Proteus*[®] software (Savitzky-Golay filter, smoothing factors 4–6, A).

At the beginning of each TGA experiment, the sample was heated up to 250 °C to obtain the anhydrous phase. The hydration and subsequent dehydration and further reaction cycles were performed under the desired water vapor partial pressure and temperature conditions. From the recorded mass change $\Delta m_{\text{TGA}}(t)$, the reaction conversion $X(t)$ was calculated based on the $\text{SrBr}_2\cdot\text{H}_2\text{O}$ sample mass, m_{sample} , and molar weights, M :

$$X_{\text{hyd}}(t) = \frac{\Delta m_{\text{TGA}}(t)}{m_{\text{sample}}} \cdot \frac{M_{\text{SrBr}_2\cdot\text{H}_2\text{O}}}{M_{\text{H}_2\text{O}}}, \quad (2)$$

$$X_{\text{dehyd}}(t) = 1 - \frac{\Delta m_{\text{TGA}}(t)}{m_{\text{sample}}} \cdot \frac{M_{\text{SrBr}_2\cdot\text{H}_2\text{O}}}{M_{\text{H}_2\text{O}}}. \quad (3)$$

The reaction conversion is analyzed in isothermal and dynamic (constant heating or cooling rate) experiments in the temperature range from 150 to 210 °C and the water vapor partial pressure range from 0

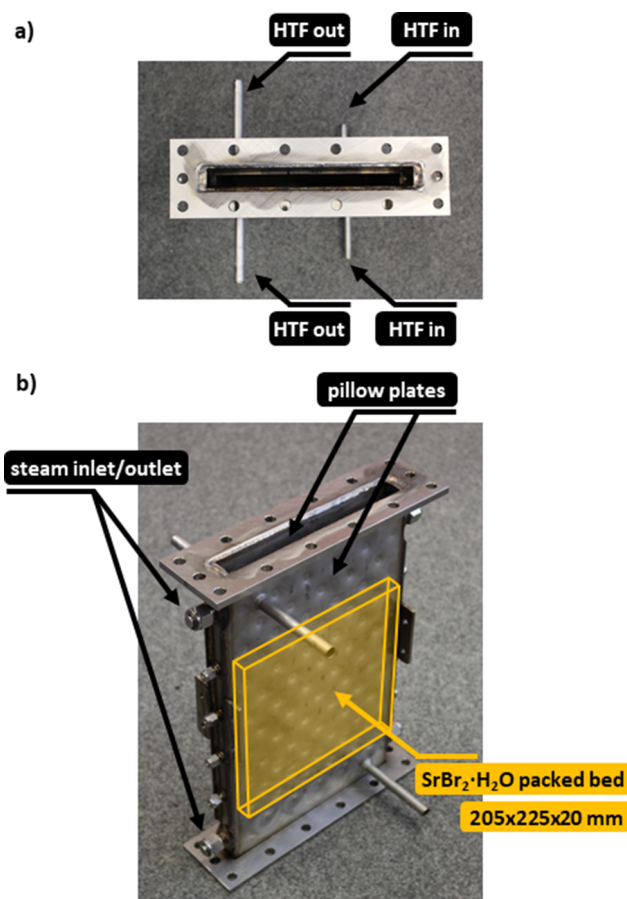


Fig. 1. Pillow plate reaction chamber. (a) Top view, (b) side view. In addition to the aspect of minimized heat losses from the bulk phase to the ambient, the reaction chamber was designed to be easily accessible for temperature sensors. It consists of two single-embossed pillow plates that are mounted with their plane sides back-to-back. This way, a 290 mm \times 225 mm \times 20 mm space is formed, filled with approximately 1 kg of $\text{SrBr}_2\cdot\text{H}_2\text{O}$ (205 mm filling height). The reactive packed bed is fixed by metallic sinter filters with a mesh size of 5 μm . During the dehydration and hydration experiments, the temperature and the flow rate of the heat transfer fluid (HTF) are set to constant values. Pt100 temperature probes are installed in the HTF inlet and outlet, and at several positions within the $\text{SrBr}_2\cdot\text{H}_2\text{O}$ fixed bed. In this analysis, the temperature measured at the central position of the fixed bed is evaluated.

to 97 kPa. For the later application, this is the operation range relevant for thermally charging the storage at low temperatures, e.g. by using waste heat from industrial processes. For discharging the storage at higher temperatures, higher steam pressures are of interest. However, due to the experimental limitations of the setups, higher pressures could not be investigated in the available TGA devices. For this purpose, a lab-scale test setup was implemented.

2.3. Lab-scale test setup

The lab-scale setup was designed to answer two specific questions: Firstly, the investigation of the general feasibility of the hydration reaction at steam pressures up to approximately 150 kPa, and secondly, detailed investigations on the reaction temperatures of the hydration and dehydration reactions. To investigate the bulk phase of the reactive material, a rectangular packed bed of the reactive material is examined, which is enclosed by single-embossed pillow plates (see Fig. 1). Via the pillow plates, the reaction chamber is heated by thermal oil, with the most important design consideration being the minimization of heat losses from the SrBr_2 packed bed to the ambient. A detailed description of the setup is given in [16]. The test rig that was used to operate the

chemical reaction is adapted from former experiments on calcium chloride [19]. The steam pressurizer, which is constructed from a tube bundle heat exchanger with thermal oil on the shell side, serves as condenser during the dehydration, and as evaporator during the hydration process. In the present work, the relevant measurement data recorded during the experiments are the temperature measured at the central position of the bulk phase and the steam pressure in the setup, which is controlled by the set condenser/evaporator temperature (temperature sensor: Pt100 class A, measurement uncertainty $\pm (0.15 \text{ }^\circ\text{C} + 0.002 \text{ }^\circ\text{C}/^\circ\text{C})$, digitization error $\pm 0.05 \text{ K}$. Pressure sensor: Endress + Hauser, Cerabar M PMP55, measurement uncertainty and digitization error $\pm (0.8 \text{ kPa} + 0.007 \text{ p/kPa})$).

The experiments are conducted as follows: before the start of a dehydration experiment, the reactive material is preheated to a constant temperature via the heat transfer fluid. Hence, steam pressure builds up in the reactive chamber. As soon as the pressure in the reaction chamber drops when connecting the reaction chamber with the condenser, the endothermic reaction starts, indicated by a temperature drop in the solid bulk phase. When the temperature in the fixed bed reaches its initial value, the dehydration reaction is considered to be completed, and the test setup is evacuated to remove all remaining inert gases or steam. Correspondingly, during the hydration process, steam is supplied at a constant evaporation temperature. As soon as the vapor penetrates the solid phase after connecting the reaction chamber with the evaporator, the exothermic reaction starts, thus resulting in a steep rise in the solid temperature. Again, the chemical reaction is assumed to be completed when the bulk phase reaches its initial temperature. For the hydration reaction, we discussed exemplary $T(p,t)$ curves and pressure-dependent maximum reaction temperatures in a prior publication [16]. In this work, we present the corresponding results of the dehydration reaction, i.e. the minimum temperatures which were measured at the central position of the fixed bed for different steam pressures.

2.4. Thermodynamic equilibrium and kinetic modelling of gas–solid reactions

Before we proceed to the discussion of the experimental results, the thermodynamic considerations for the analysis of reversible gas–solid reactions will be discussed in brief.

Assuming ideal gas properties, the equilibrium constant K_{eq} for the gas–solid reaction from Eq. (1) is given by the expression

$$K_{\text{eq}}(T, p) = \left(\frac{p}{p^0}\right)^{\nu_{\text{H}_2\text{O}}}, \quad (4)$$

with the stoichiometric coefficient $\nu_{\text{H}_2\text{O}} = 1$ and the reference pressure p^0 . In the thermodynamic equilibrium state, the Gibbs free energy is minimized, and Eq. (5) applies:

$$\Delta_{\text{R}}G = \Delta_{\text{R}}G^0 + RT \cdot \ln K_{\text{eq}}(T, p) = 0. \quad (5)$$

With the definition of the Gibbs free energy of reaction,

$$\Delta_{\text{R}}G^0 = \Delta_{\text{R}}H^0 - T \cdot \Delta_{\text{R}}S^0, \quad (6)$$

we obtain the linear form of the Van't Hoff equation for a reversible gas–solid reaction:

$$\ln K_{\text{eq}}(T, p) = \ln\left(\frac{p}{p^0}\right) = -\frac{\Delta_{\text{R}}H^0}{RT} + \frac{\Delta_{\text{R}}S^0}{R}. \quad (7)$$

Thus, according to Eq. (7), a $\ln(K_{\text{eq}})$ versus $1/T$ graph (Van't Hoff plot) based on the standard molar enthalpy and entropy of the chemical reaction (e.g. calculated from molar enthalpies and entropies of formation) gives an approximation of the equilibrium line. Different methods are established to investigate the thermodynamic equilibrium line of gas–solid reactions, e.g. dynamic TGA measurements with varying gas pressures or long-term pressure measurements in

isothermal closed systems. However, in non-ideal thermochemical systems, a thermal hysteresis can arise between the endothermic and the exothermic reactions, e.g. due to kinetic limitations and the occurrence of a metastable zone in the vicinity of the equilibrium line, resulting in two “apparent” equilibrium lines instead of a single one, e.g. such as observed in the case of calcium chloride [20] and copper chloride [21]. This is also the case for the $\text{SrBr}_2/\text{H}_2\text{O}$ reaction system investigated in the present work. In this context, we therefore use the term “pressure-dependent reaction temperature”, when we refer to the apparent equilibrium temperature. Experimental data points on the pressure-dependent reaction temperatures are obtained from the lab-scale setup. These data are evaluated to determine the operation range of the thermochemical working pair.

For the design of high-power storage reactors, not only knowledge on the reaction temperatures is required, but also information on the effective reaction rates, as these might limit the performance of the storage. However, it is important to note that it is not our aim to gain a deep understanding on the actual reaction mechanisms or the physical processes which determine the reaction kinetics of the gas–solid reactions. Instead, we set our focus on establishing application-oriented empirical models for describing the effective reaction rate with regard to the relevant conditions for thermochemical energy storage and heat transformation.

For the parametrization of the empirical reaction rate models, experimental data from TGA measurements are evaluated. Based on the general kinetic equation commonly used for describing the reaction rate in gas–solid reactions, we consider three separate rate-determining terms:

$$\frac{dX}{dt} = k(T) \cdot f(X) \cdot h(p) \quad (8)$$

with the temperature-dependent term $k(T)$ according to Arrhenius law, a yield-dependent term $f(X)$, and a vapor pressure-dependent term $h(p)$. For describing the influence of the gas pressure, we chose a term in the form of $h(p) = (1 - p/p^*)^n$, with p^* referring to the equilibrium pressure.

Hence, for the dehydration reaction, the reaction rate is described as follows:

$$\frac{dX}{dt} = A_0 \exp\left\{-\frac{E_a}{RT}\right\} \cdot f(X) \cdot \left(1 - \frac{p}{p_{\text{dehyd}}}\right)^n, \quad (9)$$

and, correspondingly, for the hydration reaction:

$$\frac{dX}{dt} = A_0 \exp\left\{-\frac{E_a}{RT}\right\} \cdot f(X) \cdot \left(\frac{p}{p_{\text{hyd}}} - 1\right)^n. \quad (10)$$

The kinetic parameters (pre-exponential factor A_0 , activation energy E_a , conversion-depending reaction model function $f(X)$, and pressure term exponent n) are fitted from isothermal and isobaric TGA experiments. The detailed fitting procedure is described in Section 3.3.

3. Results and discussion

Using the experimental methods and data analysis procedures described above, the thermochemical working pair $\text{SrBr}_2/\text{H}_2\text{O}$ is investigated with regard to its operation range for energy storage and heat transformation. Data on the dehydration reaction temperature and kinetics are necessary to better understand the limiting processes during the charging phase of the storage, which we assume to take place at temperatures as low as possible in industrial applications. In contrast, the hydration reaction determines the maximum discharge temperature and thermal power of the storage, given that steam is supplied as gaseous reactant at a certain maximum pressure, e.g. determined by the maximum available waste heat temperature. And, lastly, cycle stability of the chemical reaction is a basic prerequisite in all kinds of industrial storage and heat transformation applications.

3.1. Investigations on the dehydration and hydration reaction temperatures

As described above, data on the thermodynamic equilibrium of gas–solid reactions are commonly determined from dynamic (non-isothermal) TGA measurements. Usually, sets of dynamic experiments with varying vapor pressures are performed, and the onset temperatures are evaluated [22]. As the onset temperature also depends on the heating rate (dehydration) or cooling rate (hydration), respectively, measurements are conducted at different rates. The onset temperatures are extrapolated to a rate of 0 K/min, which gives the estimated equilibrium temperature for a corresponding vapor partial pressure.

However, following this procedure for the reaction system $\text{SrBr}_2/\text{H}_2\text{O}$, a kinetic limitation was found which led to unexpectedly low hydration temperatures. For example, for heating/cooling rates of ± 0.5 K/min and a water vapor partial pressure of 19 kPa, the onset temperature of the dehydration reaction was 211 °C, whereas for the hydration reaction at the same vapor pressure, an onset temperature of 158 °C was found, thus resulting in a thermal hysteresis of 53 K (see Fig. 2a).

In contrast to these dynamic TGA experiments, where a specific temperature profile is applied on the SrBr_2 sample, the experiments with the lab-scale setup are conducted at constant preheat temperatures. However, no significant heat flux is introduced into or withdrawn from the reactive material during the reaction. Hence, a characteristic temperature plateau builds up in the bulk phase. These characteristic plateaus correspond to a minimum temperature in the case of the endothermic dehydration reaction, and to a maximum temperature in the case of the exothermic hydration reaction.

Compared to the TGA experiments at similar vapor (partial) pressures, our results from the lab-scale experiment show slightly lower dehydration temperatures (202 °C reaction temperature vs. 211 °C onset temperature) and significantly higher hydration temperatures (188 °C reaction temperature vs. 158 °C onset temperature). Thus, in the lab-scale experiment, the thermal hysteresis is reduced to 14 K between the dehydration of the monohydrate and the hydration of the anhydrous phase (see Fig. 2b). This finding indicates that the onset temperatures determined from dynamic TGA experiments are dominated by a kinetic limitation, and therefore do not lead to a reliable evaluation of the thermodynamic equilibrium state. Obviously, the lab-scale setup results are much closer to the actual thermodynamic equilibrium. As described by Sögütoglu et al., a metastable zone in the vicinity of the of the equilibrium line can be described by nucleation and

growth processes [21]. Based on their findings, the kinetic limitation observed in the TGA experiments on the SrBr_2 hydration reaction could be explained by the formation of nuclei, with the nucleation rate limiting the overall conversion in the metastable zone. This could lead to the lower hydration onset temperature found in the dynamic TGA experiment. In contrast, in the lab-scale setup with a sample mass of around 1 kg, the existence of nucleation sites already at the very beginning of the hydration reaction is very likely, e.g. due to a remainder of some only partially dehydrated crystals in the packed bed. These already available nucleation sites could instantaneously trigger the hydration reaction, thus leading to higher apparent equilibrium temperatures in the lab-scale setup. Hence, to obtain the pressure-dependent reaction temperatures of the hydration and the dehydration reactions, we use the lab-scale setup which features reaction conditions more representative for potential storage applications.

One key finding of those lab-scale experiments is that the temperature plateaus are solely determined by the steam pressure, and do not depend on the preheat temperature of the bulk phase, which is set via the heat transfer fluid temperature. Corresponding exemplary experiments with a variation of the steam pressures and preheat temperatures are presented in Fig. 3. Based on these results, we conclude that from the temperature plateaus, the pressure-dependent reaction temperatures of the chemical reaction can be derived in sufficient approximation.

The resulting temperature–pressure data pairs are plotted in the Van't Hoff graph in Fig. 4 for a total of 75 experiments, conducted with three different batches of $\text{SrBr}_2\cdot\text{H}_2\text{O}$. In this experimental series, the steam pressures as well as the preheat temperatures were varied. The experimental results reveal that there still is a thermal hysteresis between the endothermic and the exothermic reaction, but that it is significantly smaller than found in dynamic TGA experiments. We assume this hysteresis to be caused by a similar mechanism as discussed for the TGA experiments, which is presumably more significant at lower temperatures. For experimental reasons (the maximum thermal oil temperature is limited to 210 °C), higher dehydration pressures could not be investigated in the available setup. Additional experiments would hence be needed to fully clarify if the two lines merge into one at higher steam pressures (and thus, at higher absolute temperatures), as it is the case e.g. for the hydration reaction of CaO and dehydration of $\text{Ca}(\text{OH})_2$, respectively [23].

In order to account for the drifting apart of the reaction temperatures from the equilibrium line for pressures below approximately

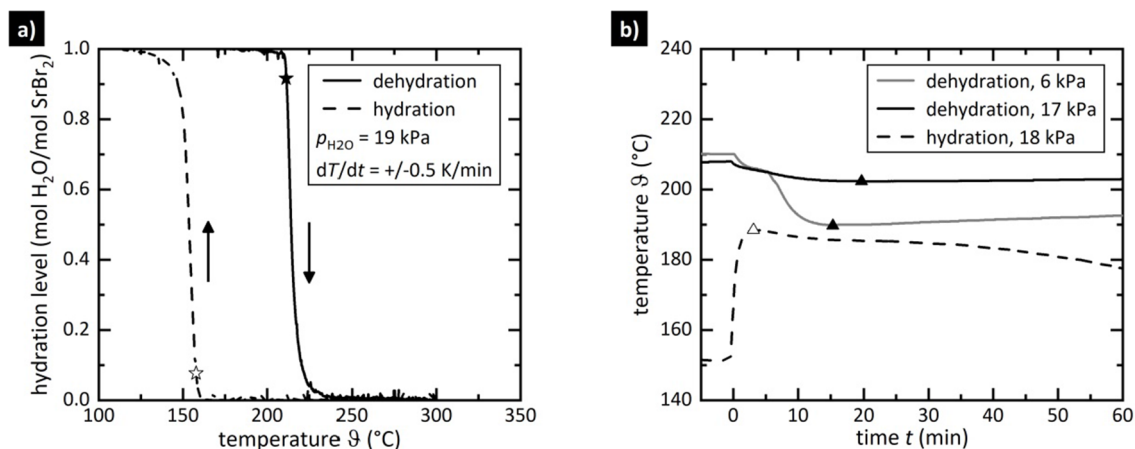


Fig. 2. (a) Investigation of the dynamic dehydration and hydration reaction with thermogravimetric analysis (TGA). Resulting level of hydration for $p = 19$ kPa and a heating/cooling rate of ± 0.5 K/min. A hysteresis of 53 K is found between the hydration and dehydration onset temperatures (☆,★). (b) Investigation of the pressure-dependent reaction temperatures in the lab-scale setup. For a similar steam pressure as in the TGA experiments (hydration: 18 kPa, dehydration: 17 kPa), a significantly smaller hysteresis of 14 K between the reaction temperatures (△,▲) is observed. When the pressure was lowered to 6 kPa in the dehydration process, a reaction temperature of 189 °C was reached. In comparison to the 188 °C hydration data point, this corresponds to a hysteresis of approximately 12 kPa in terms of the pressure offset between the back and forward reaction at the same temperature.

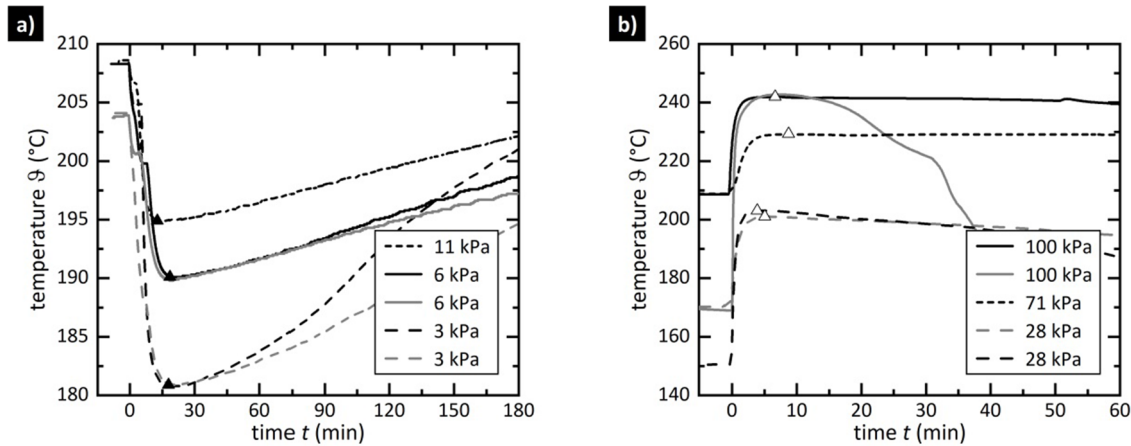


Fig. 3. Investigation of the reaction temperatures in the lab-scale setup for different steam pressures and preheat temperatures. The differing preheat temperatures can be read from the isothermal conditions before the start of the experiment ($t = 0$ min). The resulting plateau temperatures (Δ , \blacktriangle) are evaluated as a function of the corresponding pressure data. a) Dehydration reaction. b) Hydration reaction.

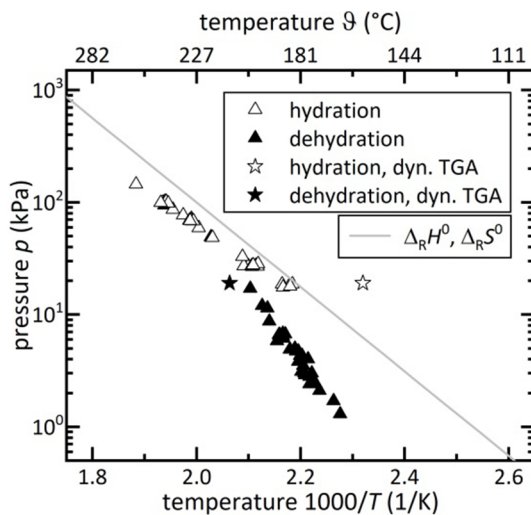


Fig. 4. Van't Hoff plot of the experimental results on the dehydration and hydration reaction temperatures. In addition to the pressure-dependent, characteristic temperature plateaus found in experiments with the lab-scale setup (Δ , \blacktriangle), the plot contains data from dynamic TGA measurements (\star , \blackstar). These two experiments were conducted at a heating and cooling rate of ± 0.5 K/min and, despite this low rate, reveal a thermal hysteresis which is significantly larger than the one observed in the lab-scale experiments. The thermodynamic data $\Delta_R H^0 = 72.8$ kJ/mol and $\Delta_R S^0 = 152$ J/(mol·K) are given for the reference pressure $p^0 = 0.1$ MPa, and temperature $T^0 = 298$ K [15].

30 kPa, the dehydration and the hydration data points were fitted by linear regression:

$$\text{dehydration reaction: } \log(p_{\text{dehyd}}/\text{kPa}) = 14.69 - 6.41 \cdot \frac{10^3}{T/\text{K}}, \quad (11)$$

$$\text{hydration reaction: } \log(p_{\text{hyd}}/\text{kPa}) = 8.18 - 3.19 \cdot \frac{10^3}{T/\text{K}}. \quad (12)$$

These correlations of the steam pressure and the reaction temperatures give a first estimation of the operation range of a thermochemical storage and heat transformer operated with the $\text{SrBr}_2/\text{H}_2\text{O}$ working pair. E.g., we conclude that a minimum temperature of 170°C will be required to charge the storage, even if the steam pressure is kept below 2 kPa (15°C condensation temperature), which can be considered a lower limit in industrial applications due to the needed cooling effort. The two p, T -correlations from Eqs. (11) and (12) are used in the analysis on the effective hydration and dehydration reaction rates

later on.

3.2. Cycle stability

After having identified the operation range of the reversible chemical reaction, probing the cycle stability is the next crucial hurdle to qualify the $\text{SrBr}_2/\text{H}_2\text{O}$ working pair for any industrial storage application. As 170°C is identified as the minimum required charging temperature, this value is chosen as reference temperature for isothermal cycling TGA experiments. In this analysis, the progression of the reaction conversion is evaluated.

100 hydration/dehydration cycles were performed at the constant temperature of 170°C (STA 449 F3 with humidity sensor): In the hydration phase, the water vapor partial pressure was set to 30 kPa (relative humidity of 51% at 85°C) for the duration of one hour. This humidity condition was chosen as it allows for full conversion to the monohydrate within < 10 min. Subsequently, the relative humidity in the sample chamber was set to 0% for one hour, except for the last dehydration phase (cycle #100), which was set to three hours under dry atmosphere. The humidity was measured in the gas mixing chamber next to the inlet of the sample chamber. When analyzing the recorded humidity for the given TGA operation conditions, we observed that it takes < 2 min to reach 80% of the set humidity during the hydration phase, but approximately 10 min until a dry atmosphere is obtained in the sample chamber in the dehydration phase. This temporal offset, which depends on the TGA parameters (e.g. prior and set humidity, gas volume flow and temperatures) causes a dead time until the reaction in the TGA sample chamber starts, both in the case of the dehydration and the hydration reaction.

In the analysis on the reaction conversion calculated from the mass loss or gain during cycling, it is assumed that at the end of a hydration phase, i.e. after 60 min under humid atmosphere, a full reaction conversion of $X_{\text{hyd}} = 1$ is reached. The progression of the reaction conversion from cycle #1 up to cycle #100 is displayed in Fig. 5. It is found that the phase transition from the monohydrate to the anhydrous phase and reverse is cycle stable, although the rate of the dehydration reaction decelerates considerably during the cycling series especially for the “tail” of the reaction progression.

While in the 1st dehydration cycle, full conversion is already reached within approximately 20 min, the 100th dehydration is completed only after three hours (not shown in the graph). Although the hydration reaction was observed to slightly decelerate too, the effect is less significant. The first hydration reaction apparently has an offset compared to all the later cycles, even though the qualitative trend is very similar to the next cycles. We assume this to be caused by the

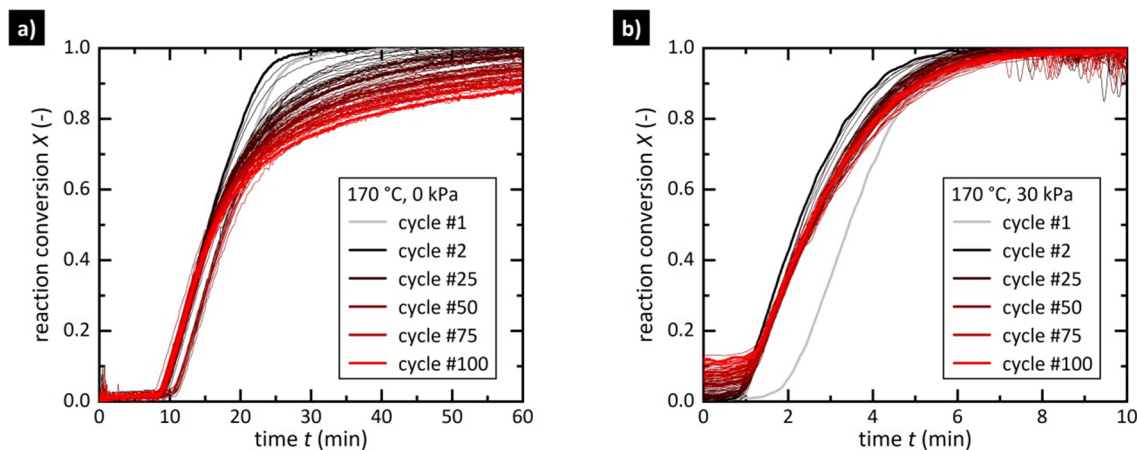


Fig. 5. Cycle stability in terms of the reaction progression during isothermal cycling. Data from different cycles are indicated by changing colors from black to red, with examples shown in the legend for orientation. (a) Isothermal dehydration at 170 °C sample temperature and dry nitrogen atmosphere. (b) Isothermal hydration at 170 °C sample temperature and a water vapor partial pressure of 30 kPa.

experimental conditions in the setup, e.g. humidification of the sample chamber walls and piping, as the equipment was purged with nitrogen for several hours before the start of the experiment. Similarly, we consider the larger dead times in several of the dehydration cycles to be experimental artefacts caused by deviant humidity conditions in the setup.

As the experimental cycle time was fixed to one hour each for the hydration and the dehydration runs, the decomposition reaction did not reach full yield after several cycles, and therefore the hydration reaction did not start from the hydration level 0.0 mol H₂O/mol SrBr₂ for higher cycle numbers. The impact of the rate-decelerating effect is quantifiable from the analysis presented in Fig. 6, which gives the experimental time until 50% and 80% of the expected full conversion are reached. The time constants do not change for the hydration and, in the case of 50% conversion, also for the dehydration reaction. In contrast, the 80% time constant in case of the dehydration rises linearly. Over the course of 100 hydration/dehydration cycles, this time constant increases by approximately 60%. We assume this to be caused by microscopic changes within the SrBr₂·H₂O phase, e.g. causing inhibited vapor mass transfer, or by some effect on the reaction kinetics of the dehydration reaction. It is not clear from this experiment, if and when any steady state is reached.

Please note that this cycling series was performed under “extreme” experimental conditions, i.e. the minimum temperature required to perform the dehydration reaction on a reasonable time scale (< 1 h in TGA experiments). We believe this very low temperature of 170 °C to be hardly realistic for charging the storage in an industrial application as this requires very low steam pressures (< 2 kPa or 15 °C condensation temperature). Therefore, in order to understand how the cycling affects the dehydration behaviour at higher temperatures and pressures which are likely to be more relevant in industrial applications, additional experiments were performed with the cycled SrBr₂ sample and compared to an uncycled sample in an identical experiment. At the beginning of these experiments, the samples were treated with the usual heating procedure up to 250 °C to ensure complete dehydration to the anhydrous phase. Fig. 7 contrasts the results obtained for the cycled SrBr₂ with the results from the uncycled SrBr₂. In all cases, the reaction conversion exceeds 95%, with no significant differences between cycled and uncycled samples (< 3%) with the given measurement accuracy. For better comparison of the reaction progression, the conversion is normalized to a value of 1 in Fig. 7. As the dead time varies due to the different experimental conditions, the curves are shifted along the time axis. The onset time $t = 0$ min is determined by the intercept point of a tangent fitted at $X_{\text{norm}} = 0.1$ with the time axis. It is observed that at higher dehydration temperatures (210 °C), the reaction conversion of

the cycled material is very similar to the behavior of uncycled material: the progression of the dehydration reaction at 210 °C and a dry nitrogen atmosphere, and also under a water vapor partial pressure of 10 kPa, is not affected in any way similar to the dehydration behavior under the cycling series conditions (170 °C, 0 kPa). This is a very important finding since it proves that the lacking cycle stability indicated by Fig. 6 is only of little relevance under application-relevant operation temperatures. Also, this observation supports the assumption that cycling may affect the reaction kinetics of the dehydration reaction, but not the “chemical” reversibility of the dehydration reaction.

No macroscopic changes were visible to the bare eye when the SrBr₂ sample was optically investigated after the completion of the experimental series. The granules did not agglomerate, but were still loose and easily pourable. However, this does not give information on cycling-induced microscopic transformations within the SrBr₂ particles.

Summing up, from the experimental study on the cycle stability of the monohydrate formation and decomposition, we conclude that the reaction is chemically reversible, although the reaction rate of the dehydration reaction decreases in the course of the cycling at low temperatures (170 °C). Given that this degradation effect is not observed when the cycled material is investigated at higher temperatures (210 °C), and moreover, that the degradation could likely be eliminated

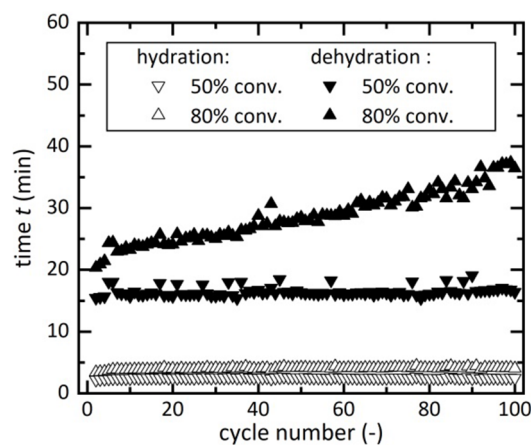


Fig. 6. Evaluation of the cycle stability in terms of the experimental time required to reach 50% and 80% reaction conversion. While the hydration reaction can be considered to be fully cycle-stable under the given experimental conditions (170 °C, 30 kPa water vapor partial pressure), a decrease of the effective reaction rate of the dehydration reaction is found at reaction conversions larger than 50% (170 °C, dry nitrogen atmosphere).

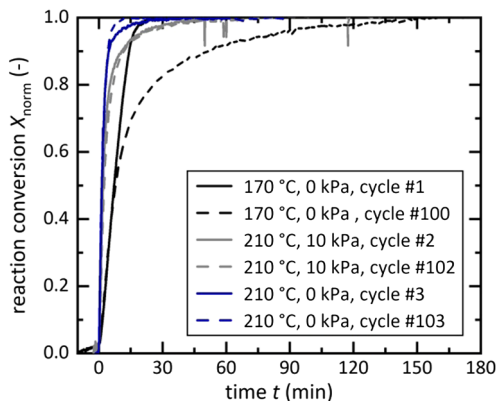


Fig. 7. Progression of the dehydration reaction conversion of cycled and uncycled SrBr₂·H₂O. For better comparison, the conversion is normalized and the reaction onset time is set to 0 in this graph. These experiments prove the cycle stability of the SrBr₂/H₂O working pair over 100 hydration/dehydration cycles.

by pretreating the SrBr₂·H₂O particles (e.g. milling to obtain smaller primary particles) or using rate-accelerating additives, our results indicate that the reaction system SrBr₂/H₂O is indeed a promising candidate for thermochemical energy storage and heat transformation, with applications requiring large numbers of charging/discharging cycles. Besides, the progression of the dehydration reaction conversion performed under application-relevant operation conditions (210 °C and 10 kPa, corresponding to 45 °C condensation temperature) shows that 80% of the full conversion is reached after approximately 5 min, thus highlighting that the SrBr₂/H₂O working pair promises high specific thermal powers due to fast reaction kinetics. This last point is discussed in more detail in the following section.

3.3. Empirical models of the effective reaction rates

Not only the thermodynamic properties (i.e. pressure-dependent reaction temperatures), but also the reaction kinetics determine a thermochemical storage's operation range since the maximum thermal power of the thermochemical reactor is limited by the effective rate of the chemical reaction. To be able to assess the maximum thermal powers allowed by the effective rate of reaction, kinetic data on the reaction progression are required, which include the temperature and pressure range relevant for typical storage applications. However, due to the operational limitations of the TGA setups, this range is restricted to operation under atmospheric pressures and adjusting the steam pressure by dilution with nitrogen. In the following analysis, it is therefore assumed that running the chemical reaction at water vapor partial pressures instead of pure steam atmosphere does not affect the reaction progression. This is considered a valid assumption due to the milligram sample size, so that the formation of a nitrogen boundary layer (which could limit vapor transport) can be neglected. Please note that the aim of this section is not to understand the reaction mechanism in depth, but rather to provide the simplest empirical model with sufficient resolution for the investigation of potential applications.

Based on the qualitative progression of the reaction conversion presented in the investigation on the cycle stability, a single-step reaction progression is assumed. Besides, the trends of the reaction conversion of uncycled material suggest that a bounded exponential growth model is appropriate to mathematically describe the effective reaction rates. Hence, we chose the first-order rate model for both the dehydration reaction and the hydration reaction [24]:

$$X(t) = 1 - \exp(-k_{\text{eff}} \cdot t). \tag{13}$$

With the thereby given linear correlation between $-\ln(1-X)$ and t , effective rate coefficients $k_{\text{eff,exp}}$ were determined by fitting results from TGA experiments similar to the cycling experiments from Fig. 5

Table 1

Effective rate coefficients $k_{\text{eff,exp}}$ of the dehydration reaction under isothermal and isobaric conditions. ΔT gives the difference between the experimental temperature T and the reaction temperature T_{dehyd} expected for the given water vapor partial pressure p . R^2 gives the coefficients of determination of the linear fit of the experimental data, which is evaluated in the range from X_{min} to X_{max} .

T (°C)	p (kPa)	T_{dehyd} (°C)	ΔT (K)	$k_{\text{eff,exp}}$ (10 ⁻³ /s)	R^2 (-)	X_{min} (-)	X_{max} (-)
162	0	-	-	1.08	0.921	0.05	0.80
172	0	-	-	1.82	0.938	0.05	0.80
185	0	-	-	3.20	0.974	0.05	0.80
190	0	-	-	4.20	0.987	0.05	0.80
210	0	-	-	8.69	0.997	0.05	0.80
210	0	-	-	9.01	1.000	0.05	0.80
185	5	185	≈ 1	1.47	0.987	0.10	0.60
190	5	185	5	3.25	0.987	0.05	0.80
200	5	185	15	5.26	0.996	0.05	0.80
210	5	185	25	9.21	0.998	0.05	0.80

conducted under isothermal and isobaric conditions. The rate curves $X(t)$ are normalized to 1. In the non-normalized data, the average reaction conversion is 1.00, with a standard deviation of 2%. The minimum and maximum values range from 0.95 to 1.05. We assume that the reaction yielded full conversion in the experiments evaluated in context of the reaction rate determination, and attribute the error to measurement inaccuracies, e.g. due to partial hydration during weighing of the monohydrate samples under ambient conditions. The results of the evaluation on $k_{\text{eff,exp}}$ are summarized in Table 1 (dehydration reaction) and Table 2 (hydration reaction).

Considering the rate of reaction derived from Eq. (13),

$$\frac{dX}{dt} = k_{\text{eff}} \cdot (1 - X) = k_{\text{eff}} \cdot f(X), \tag{14}$$

and the rate model proposed in Eq. (8), it follows that k_{eff} gives all the necessary information on the activation energy E_a , the pre-exponential factor A_0 , and the exponent n of the pressure term:

$$\text{dehydration reaction: } k_{\text{eff}} = A_0 \exp\left\{-\frac{E_a}{RT}\right\} \cdot \left(1 - \frac{p}{p_{\text{dehyd}}}\right)^n, \tag{15}$$

$$\text{hydration reaction: } k_{\text{eff}} = A_0 \exp\left\{-\frac{E_a}{RT}\right\} \cdot \left(\frac{p}{p_{\text{hyd}}} - 1\right)^n. \tag{16}$$

The further reaction rate analysis is discussed separately for the hydration and dehydration reactions in the following sections.

3.3.1. Parametrization of the dehydration reaction rate model

The dehydration reaction of the monohydrated salt was investigated

Table 2

Effective rate coefficients $k_{\text{eff,exp}}$ of the hydration reaction under isothermal and isobaric conditions. ΔT gives the difference between the experimental temperature T and the reaction temperature T_{hyd} expected for the given water vapor partial pressure p . R^2 gives the coefficients of determination of the linear fit of the experimental data, which is evaluated in the range from X_{min} to X_{max} .

T (°C)	p (kPa)	T_{hyd} (°C)	ΔT (K)	$k_{\text{eff,exp}}$ (10 ⁻³ /s)	R^2 (-)	X_{min} (-)	X_{max} (-)
186	69	230	-44	12.98	0.996	0.06	0.95
192	69	230	-38	8.19	0.985	0.05	0.90
200	69	230	-30	3.84	0.992	0.05	0.85
203	69	230	-27	2.35	0.996	0.05	0.85
207	69	230	-23	1.38	0.994	0.05	0.65
180	29	202	-22	1.54	0.997	0.05	0.85
180	36	209	-28	3.46	0.984	0.05	0.90
180	45	216	-36	8.06	0.991	0.05	0.80
180	55	223	-42	13.20	0.986	0.05	0.95
151	45	216	-65	65.63	0.964	0.05	0.95

in isothermal experiments performed at low water vapor partial pressures (STA 449F3 with humidifier and humidity sensor). To account for the temperature-dependency of the dehydration reaction rate, the first parameter being assessed from an Arrhenius plot is the activation energy E_a , and the pre-exponential factor A_0 , see Fig. 8a. In this analysis, data from TGA experiments in dry nitrogen atmosphere are evaluated, since this way the vapor pressure influence on the reaction rate can be neglected. The temperatures in the considered experiments vary in the range from 160 °C to 210 °C, and the analysis gives the two parameters $E_a = 75.7$ kJ/mol and $A_0 = 1.38 \cdot 10^6$ 1/s.

In the next step, the pressure term exponent n is fitted from dehydration experiments in humid atmosphere. In this analysis, experiments at a constant water vapor partial pressure of 5 kPa and different temperatures were considered, as these values are relevant for industrial applications and, besides, correspond to the operation conditions investigated in the proof-of-concept of the SrBr₂/H₂O working pair in a 1 kW storage module [17]. From the plot given in Fig. 8b, we obtain the parameter $n = 0.25$.

Hence, the empirical rate model of the dehydration reaction is parametrized as follows:

$$\frac{dX}{dt} = 1.38 \cdot 10^6 \text{s}^{-1} \exp\left\{-\frac{75.7 \text{ kJ} \cdot \text{mol}^{-1}}{RT}\right\} \cdot (1-X) \cdot \left(1 - \frac{p}{p_{\text{dehyd}}}\right)^{0.25}. \quad (17)$$

The reaction pressure p_{dehyd} for the given temperature is derived from the experimental results of the lab-scale setup, and can be obtained from Eq. (11).

3.3.2. Parametrization of the hydration reaction rate model

The hydration reaction was investigated in isothermal experiments performed at higher water vapor partial pressures (STA 449C with steam generator). Following the same procedure as in the case of the dehydration reaction, the effective rate coefficients $k_{\text{eff,exp}}$ are calculated based on a first-order rate model, see Table 2. Notably, the results indicate that at constant vapor pressures and varying temperatures, the rate coefficients actually decrease with increasing temperature (or decreasing temperature difference ΔT).

This is explained by the pressure term in Eq. (10) (last term): an increased temperature leads to a higher reaction pressure p_{hyd} , thus resulting in a smaller ratio p/p_{hyd} , which lowers the overall reaction rate. In the considered temperature and pressure range, this rate-limiting effect of the pressure term overbalances the rate-increasing impact of the Arrhenius term. If these k_{eff} data were fitted in an Arrhenius plot (compare Fig. 8a for the dehydration reaction), this would result in a physically nonsensical negative activation energy. This is not an

uncommon phenomenon for gas–solid reactions showing a rate decrease in the vicinity of the equilibrium line. For instance, a virtual negative activation energy was also observed for the hydration reaction of calcium oxide [25]. A non-parametric modelling method such as proposed by Birkelbach et al. is one approach to address such kind of a reaction rate behavior [26]. However, since in this work we pursue an application-oriented empirical correlation on the hydration reaction rate, we set aside the determination of the Arrhenius parameters (pre-exponential factor A_0 , activation energy E_a) from the experimental data. Instead, based on the assumption of a first-order rate model, we simplify Eq. (16) by replacing the Arrhenius term by a constant, and obtain the following equation:

$$k_{\text{eff}} = K_{\text{Fit}} \cdot \left(\frac{p}{p_{\text{hyd}}} - 1\right)^n. \quad (18)$$

Provided that this mathematical approach is valid, plotting the data points $\ln(k_{\text{eff}})$ versus $\ln(p/p_{\text{hyd}}-1)$ should result in a straight line, with the slope n and the offset $\ln(K_{\text{Fit}})$. Indeed, the experimental data displayed in Fig. 9a indicate that this simplification of the rate model is justified. The slope of the linear fit gives the pressure term exponent $n = 1.8$. The rate coefficient $K_{\text{Fit}} = 1.60 \cdot 10^{-3}$ 1/s is determined from the intercept.

Therefore, the parametrized rate model of the hydration reaction results in:

$$\frac{dX}{dt} = 1.60 \cdot 10^{-3} \text{s}^{-1} \cdot (1-X) \cdot \left(\frac{p}{p_{\text{hyd}}} - 1\right)^{1.8}. \quad (19)$$

The reaction pressure p_{hyd} for the given temperature is derived from the experimental results of the lab-scale setup, and can be obtained from Eq. (12). Due to the simplification of the hydration rate model, i.e. due to omitting the rate-diminishing Arrhenius term, the model will at some point fail to correctly reproduce the decrease of the rate with decreasing temperatures. Instead, the model given in Eq. (19) would predict infinitely increasing reaction rates with decreasing temperatures. Hence, predicting a “cold start” of the hydration reaction from initial temperatures of more than approximately 65 K below the expected reaction temperature (compare maximum values of ΔT given in Table 2) could lead to incorrect results. Apart from that, in the particular case of the SrBr₂/H₂O reaction system, starting from “too low” temperatures (e.g. ambient temperature) would lead to a hydration reaction not only from the anhydrous salt to the monohydrate, but also from the monohydrate salt to the hexahydrate, and then to an unwanted solid–liquid phase change at higher temperatures.

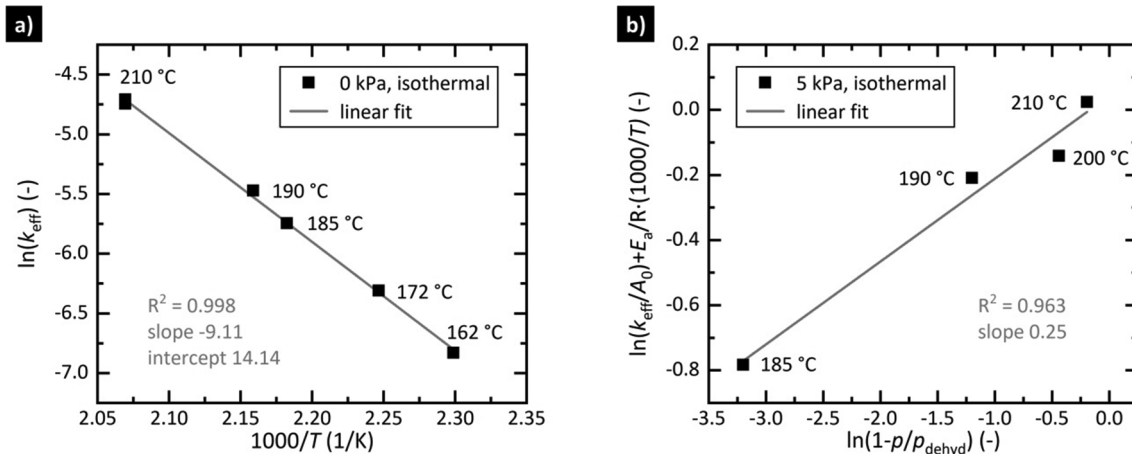


Fig. 8. Dehydration reaction. (a) Determination of the activation energy E_a from the slope and the pre-exponential factor A_0 from the offset of the linear regression (Arrhenius plot). Only experiments conducted under dry nitrogen atmosphere are evaluated in this analysis. (b) Determination of the pressure term exponent. Here, experiments conducted under 5 kPa water vapor partial pressure and different temperatures are evaluated.

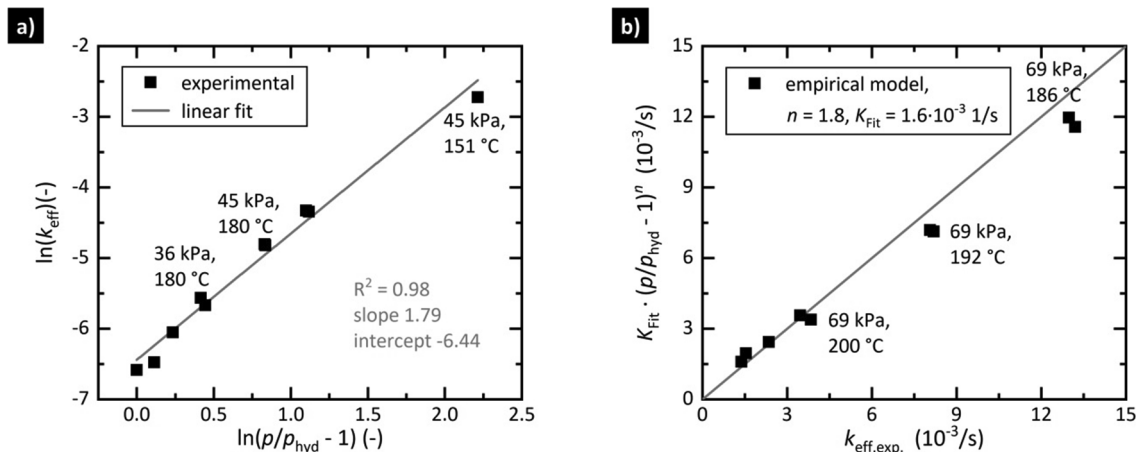


Fig. 9. Parametrization of the hydration rate model. (a) The pressure term exponent n is determined from the slope, and the rate coefficient K_{Fit} from the intercept of the linear fit. (b) Validity evaluation of the effective rate coefficients predicted by the empirical model, which is parametrized with the values n and K_{Fit} determined from the left plot. The bisectrix in the parity plot indicates an ideal reproduction of the experimental rate coefficients.

Although Eq. (19) is based on a simplified rate model approach, the effective rate coefficients are reproduced with good accuracy. This is indicated by the evaluation presented in the form of a parity plot in Fig. 9b, which contrasts the predicted with the experimental rate coefficients. The rate-diminishing effect of increased temperatures is correctly reproduced. However, for operation parameters resulting in larger rates, e.g. 69 kPa and 186 °C, the model slightly underrates the experimental values.

3.3.3. Model evaluation

In a last step, the empirical models are evaluated by comparison with the experimentally determined reaction conversions from the TGA experiments. Fig. 10 shows the modelled reaction conversions (line plots) versus the experimental results (scattered plots) for varying operation conditions. For all of the depicted graphs, the results from the empirical models are shifted along the time axis so that the point $X_{norm} = 0.5$ corresponds to the same point of the experimental curve in order to compensate for the dead time caused by the TGA experimental conditions.

Generally, the qualitative trends of the reaction conversions are correctly reproduced by the empirical models. In the case of the dehydration, the rate-increasing impact of the temperature is clearly indicated by the model (e.g. 5 kPa, 190 °C versus 210 °C). For higher rates, e.g. 10 kPa and 210 °C, the slope of the reaction conversion is

closely reproduced by the empirical model up to a conversion of 80%, even though the parametrization of the rate model was implemented based on a data set with a maximum dehydration vapor pressure of 5 kPa. For low dehydration rates, e.g. 170 °C and dry nitrogen atmosphere, the model underrates the dehydration progression of $SrBr_2 \cdot H_2O$. Here, the reaction conversion follows a more sigmoidal trend and, hence, is not closely represented by a first-order rate model.

Similarly, in the case of the hydration reaction, the empirical model shows close agreement with experimental data for operation parameters which allow high reaction rates. For operation parameters closer to the equilibrium conditions, e.g. 69 kPa, 207 °C, the experimental reaction conversion shows a more sigmoidal progression, and hence, cannot be fully reproduced by the first-order rate model. To prove the validity range of the empirical model, the plot includes additional experimental data which are not considered in the determination of the rate model parameters (97 kPa, 189 °C). Still, even for this higher water vapor partial pressure, the empirical model predicts the reaction conversion with sufficient accuracy.

In general, in the range from approximately $0.1 < X_{norm} < 0.8$, the qualitative trend of the reaction conversion is accurately reproduced, so that the models parametrized in this work are considered valid empirical descriptions of the hydration and dehydration reaction rates of strontium bromide anhydrate.

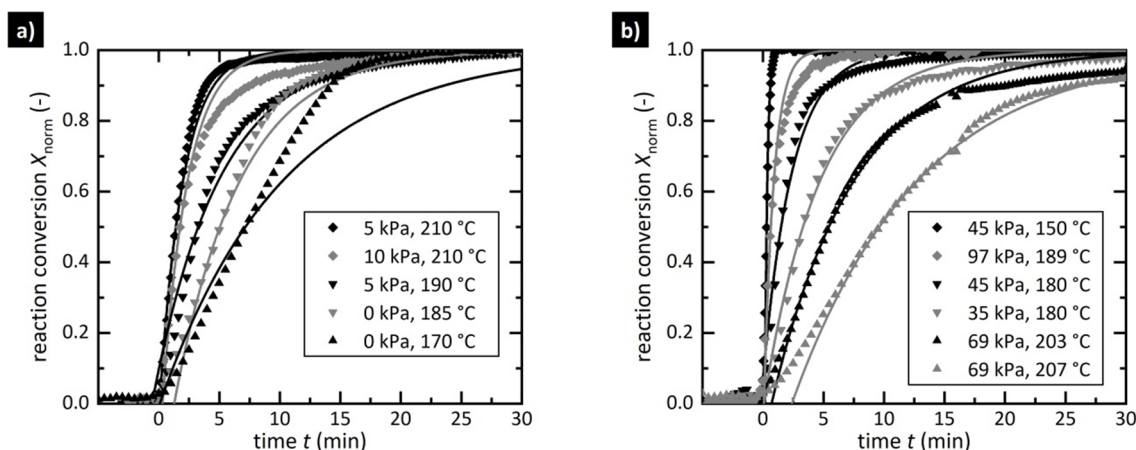


Fig. 10. Evaluation of the empirical rate models. The experimental data is given by the scatter plots; the corresponding results from the experimental rate models given in Eq. (17) and Eq. (19), respectively, are displayed as line plots in the same color. (a) Dehydration reaction. (b) Hydration reaction.

3.4. Consequences for thermochemical storage applications

The performed material characterization study provides technically feasible charging and discharging temperatures as a function of the water vapor pressure. In a previous study, we have demonstrated the technical feasibility of distinct storage operation parameters, e.g. a minimum charging temperature of 179 °C (1 kPa condenser pressure) and a maximum discharging temperature of 281 °C (560 kPa evaporator pressure) [17]. With the p,T -correlations presented here, the operation parameters of the storage can be estimated for any other operation point within this range. E.g. for a given waste heat temperature of 120 °C (200 kPa) available for steam generation, the corresponding reaction temperature of the hydration reaction is 270 °C, according to Eq. (12). Assuming that a heat exchanger temperature gradient of 20 K is required to allow for a heat flux between the heat transfer fluid (HTF) and the storage, we conclude that the storage can be discharged at 250 °C HTF temperature. On the other hand, charging the storage e.g. at 210 °C HTF temperature (e.g. solar thermal energy or industrial waste heat) requires the condensation of the gaseous reactant at 7 kPa, see Eq. (11). Again, this estimation takes into account an internal gradient of 20 K in the heat exchanger. This vapor pressure corresponds to a condensation temperature of 40 °C, e.g. cooling with ambient air. The given operation points therefore result in an effective thermal upgrade by 40 K between the charging and the discharging temperature. Besides, the analysis of the effective reaction rates reveals 170 °C as the minimum temperature required for charging with technically relevant operation conditions: although charging the storage at lower temperatures is possible with moderate dehydration rates in water-free atmospheric conditions, this requires additional cooling effort to condense the water vapor emerging from the reactive material (e.g., below 15 °C).

Our results on the effective rates of reaction imply that the SrBr₂/H₂O working pair is suitable for applications which require high specific thermal powers: e.g. for the discharging reaction running at 69 kPa and 200 °C, the effective rate coefficient $3.84 \cdot 10^{-3}$ 1/s implies that 80% of the storage's capacity can be discharged with specific thermal powers from 0.2 – 1.2 kW/kg SrBr₂, assuming a reaction enthalpy of 72 kJ/kg, the SrBr₂ molar weight 247 g/mol, and the first-order rate model described in Eq. (14). By choosing a higher steam pressure, these values can be further increased. Alternatively, for a lower discharge temperature and the same steam pressure (180 °C, 69 kPa), the specific power reaches values in the range of 0.9 – 4.4 kW/kg SrBr₂ (effective rate coefficients in Table 2). Correspondingly, running the charging reaction e.g. at 210 °C and 5 kPa results in specific thermal powers in the range of 0.5 – 2.5 kW/kg SrBr₂/H₂O (effective rate coefficients in Table 1). However, the thermal power of an actual storage reactor is more likely determined by its design with regard to heat and mass transfer limitations. For instance, at distinct operating points (discharging at 208 °C, 150 kPa), the proof-of-concept storage reactor featured a maximum thermal power of 0.26 kW/kg SrBr₂ [17], and hence, was probably limited by heat transfer. Still, the empirical rate models developed and validated in this work are required to optimize the storage performance, e.g. by performing numerical studies on the packed bed heat exchanger design.

4. Conclusions

The hydration reaction of strontium bromide to its monohydrate phase and the dehydration reaction of the latter were identified as a promising thermochemical system for thermal energy storage and heat transformation. In this study, we report on the thermodynamic and kinetic properties and the cycle stability of the reactions. Our study includes examinations based on thermogravimetric analysis (TGA) as well as lab-scale experiments.

Pressure–temperature correlations describing the reaction temperatures for the dehydration and the hydration reactions are derived

from the lab-scale setup in a pressure range from 1 kPa up to 150 kPa. The observed reaction temperatures stretch from approximately 160 °C up to 260 °C. At a steam pressure of 17 kPa, a thermal hysteresis of 14 K between the dehydration and the hydration reaction is observed. With the p,T -correlations presented here, the operation parameters of a SrBr₂/H₂O thermochemical energy storage and heat transformer can be assessed in terms of charging/discharging pressures and temperatures.

To be able to assess the maximum thermal power allowed by the effective rate of reaction, we conducted kinetic studies in a temperature and pressure range relevant for typical storage applications. It is found that the rate of reaction slows down significantly when approaching thermodynamic equilibrium conditions not only in the case of the dehydration, but also in the case of the hydration reaction: here, at constant steam pressure, increasing temperatures effectively lead to lower reaction rates. For instance, when discharging at 180 °C and 69 kPa steam pressure, specific powers up to 4.4 kW/kg SrBr₂ were found in the TGA experiments. Furthermore, we developed empirical models for the hydration and the dehydration reactions which allow predicting the progression of the chemical reactions in a storage system operated under technically relevant operation conditions (hydration reaction: 30 – 97 kPa, 150 – 210 °C; dehydration reaction 0 – 10 kPa, 160 – 210 °C).

Cycle stability is experimentally proven in an isothermal TGA experiment for 100 hydration/dehydration cycles. Although the rate of the dehydration reaction decreases for conversions larger than 50% during cycling under low temperatures (170 °C), the reaction is fully reversible. Although no final statement can be drawn on the more long-term cycle stability or possible macroscopic changes when operated on larger scale, strontium bromide is a highly promising candidate for thermochemical energy storage and heat transformation.

CRedit authorship contribution statement

Jana Stengler: Conceptualization, Data curation, Investigation, Methodology, Validation, Visualization, Writing - original draft. **Inga Bürger:** Methodology, Writing - review & editing. **Marc Linder:** Funding acquisition, Supervision, Writing - review & editing.

Declaration of Competing Interest

The authors declare that they have no known competing financial interests or personal relationships that could have appeared to influence the work reported in this paper.

Acknowledgements

The work described in this paper has received financial support from the “Bundesministerium für Wirtschaft und Energie” (BMWi, Federal Ministry for Economic Affairs and Energy) in Germany as part of the “TheSan” project (03ET1297A). We gratefully acknowledge the support of Marius Drexler and Stefan Wohnrau during the operation of the lab-scale setup and the TGA experimental campaign, respectively.

References

- [1] Wongsuwan W, Kumar S, Neveu P, Meunier F. A review of chemical heat pump technology and applications. *Appl Therm Eng* 2001;21:1489–519.
- [2] Yu Y, Zhang P, Wu J, Wang R. Energy upgrading by solid–gas reaction heat transformer: A critical review. *Renew Sustain Energy Rev* 2008;12:1302–24.
- [3] Odukoya A, Naterer GF. Upgrading waste heat from a cement plant for thermochemical hydrogen production. *Int J Hydrogen Energy* 2014;39:20898–906.
- [4] Donkers PAJ, Söğütöglu LC, Huinink HP, Fischer HR, Adan OCG. A review of salt hydrates for seasonal heat storage in domestic applications. *Appl Energy* 2017;199:45–68.
- [5] Trausel F, De Jong AJ, Cuypers R. A review on the properties of salt hydrates for thermochemical storage. *Energy Procedia* 2014;48:447–52.
- [6] Richter M, Habermann E-M, Siebecke E, Linder M. A systematic screening of salt hydrates as materials for a thermochemical heat transformer. *Thermochim Acta* 2018;659:136–50.
- [7] Afflerbach S, Trettin R. A systematic screening approach for new materials for

- thermochemical energy storage and conversion based on the Strunz mineral classification system. *Thermochim Acta* 2019;674:82–94.
- [8] N'Tsoukpoe KE, Schmidt T, Rammelberg HU, Watts BA, Ruck WKL. A systematic multi-step screening of numerous salt hydrates for low temperature thermochemical energy storage. *Appl Energy* 2014;124:1–16.
- [9] Michel B, Mazet N, Neveu P. Experimental investigation of an innovative thermochemical process operating with a hydrate salt and moist air for thermal storage of solar energy: Global performance. *Appl Energy* 2014;129:177–86.
- [10] Michel B, Neveu P, Mazet N. Comparison of closed and open thermochemical processes, for long-term thermal energy storage applications. *Energy* 2014;72:702–16.
- [11] Esaki T, Kobayashi N. Reaction rate characteristics of SrBr₂ hydration system for chemical heat pump cooling mode. *J Mater Sci Chem Eng* 2016;4:106–15.
- [12] Cammarata A, Verda V, Sciacovelli A, Ding Y. Hybrid strontium bromide-natural graphite composites for low to medium temperature thermochemical energy storage: Formulation, fabrication and performance investigation. *Energy Convers Manage* 2018;166:233–40.
- [13] Gilles D, Segato T, Courbon E, Degrez M, D'Ans P. Affordable process for the production of strontium bromide used in low grade heat recovery applications. *Procedia CIRP* 2018;69:383–8.
- [14] Glasser L. Thermodynamics of inorganic hydration and of humidity control, with an extensive database of salt hydrate pairs. *J Chem Eng Data* 2014;59:526–30.
- [15] Wagman DD, Evans WH, Parker VB, Schumm RH, Halow I, Bailey SM, et al. The NBS Tables of chemical thermodynamic properties. Selected values for inorganic and C1 and C2 organic substances in SI units. *J Phys Chem Ref Data* 1982. 11.
- [16] Stengler J, Weiss J, Linder M. Analysis of a lab-scale heat transformation demonstrator based on a gas-solid reaction. *Energies* 2019;12:2234.
- [17] Stengler J, Linder M. Thermal energy storage combined with a temperature boost: An underestimated feature of thermochemical systems. *Appl Energy* 2020;262:114530.
- [18] Perry DL. *Handbook of inorganic compounds*; 2011, 581.
- [19] Richter M, Bouché M, Linder M. Heat transformation based on CaCl₂/H₂O – Part A: Closed operation principle. *Appl Therm Eng* 2016;102:615–21.
- [20] Molenda M, Stengler J, Linder M, Wörner A. Reversible hydration behavior of CaCl₂ at high H₂O partial pressures for thermochemical energy storage. *Thermochim Acta* 2013;560:76–81.
- [21] Sögütöglü L-C, Steiger M, Houben J, Biemans D, Fischer HR, Donkers P, et al. Understanding the hydration process of salts: the impact of a nucleation barrier. *Cryst Growth Des* 2019;19:2279–88.
- [22] Wagner M. *Thermal analysis in practice: fundamental aspects*; 2018.
- [23] Schmidt M, Linder M. Power generation based on the Ca(OH)₂/CaO thermochemical storage system – Experimental investigation of discharge operation modes in lab scale and corresponding conceptual process design. *Appl Energy* 2017;203:594–607.
- [24] Galwey AK, Brown ME. Thermal decomposition of ionic solids: chemical properties and reactivities of ionic crystalline phases; 1999, 596.
- [25] Schaube F, Koch L, Wörner A, Müller-Steinhagen H. A thermodynamic and kinetic study of the de- and rehydration of Ca(OH)₂ at high H₂O partial pressures for thermo-chemical heat storage. *Thermochim Acta* 2012;538:9–20.
- [26] Birkelbach F, Deutsch M, Werner A. The effect of the reaction equilibrium on the kinetics of gas-solid reactions — A non-parametric modeling study. *Renewable Energy* 2020;152:300–7.

2.3 Paper III: Material characterization

2 Publications

2.4 Paper IV: Performance analysis

This article was published in *International Journal of Heat and Mass Transfer*, 167, 120797, Copyright Elsevier (2021).

<https://www.sciencedirect.com/science/article/abs/pii/S0017931020337352>



Performance analysis of a gas-solid thermochemical energy storage using numerical and experimental methods

Jana Stengler*, Inga Bürger, Marc Linder

Institute of Engineering Thermodynamics, German Aerospace Center (DLR) Pfaffenwaldring 38-40, 70569 Stuttgart, Germany

ARTICLE INFO

Article history:

Received 23 August 2020

Revised 6 November 2020

Accepted 30 November 2020

Keywords:

Thermochemical energy storage
heat transformation
strontium bromide
reactor design

ABSTRACT

Thermochemical energy storage is not only discussed for the long-term storage of thermal energy with large capacities, but also for applications requiring high specific thermal powers, e.g. the thermal upgrade of waste heat via thermochemical heat transformers in continuous operation. Our work aims at the quantitative analysis of the dominating processes in storage designs for gas-solid reactions, which specifically target high-power applications.

As reference storage design, we chose a 1 kW prototype featuring axial aluminum fins for an increased effective bulk conductivity. It was operated with strontium bromide, which reacts with steam in a reversible gas-solid reaction in the 160–320°C temperature range, reaching specific thermal powers up to 250 W/kg anhydrous salt. By combining our experimental work with numerical studies based on the finite element method, we quantitatively evaluate the influence of the heat transfer-related parameters on the storage's maximum thermal power. Based on a thermal sensitivity study, the largest contributor turns out to be the heat transfer coefficient between the reactive bulk phase and the heat exchanger. The experimentally validated simulation tool allows us to draw further conclusions on the scale-up of the current storage design for large-scale applications. In particular, it provides the necessary data to estimate the exergy efficiency of a broad variety of storage application scenarios of the investigated storage system.

© 2020 Elsevier Ltd. All rights reserved.

1. Introduction

Various designs for closed thermochemical thermal energy storages (TES) have been investigated for a wide variety of gas-solid working pairs, such as salts (e.g. salt hydrates or ammonium salts), metal hydrides or metal oxides [1,2]. Usually, providing sufficient heat and mass transfer at the same time is a challenging design consideration, since the solid reactants are characterized by either a low thermal conductivity when used as loose granules or powders or by low permeabilities if pressed to pellets, e.g. in the case of metal hydrides [3]. To outbalance these contradicting effects, numerous analytical and numerical models have been developed to investigate the storage performance from a local and global perspective [4]. Often, the fixed-bed reactor designs in these studies follow rather simple geometric concepts with high symmetry to ensure straight-forward modelling, e.g. cylindrical designs [5] or rectangular honeycomb blocks [6]. However, large industrial appli-

cations such as heat recovery from continuous processes, e.g. in pulp and paper industries, or batch processes in chemical industries, require reactor concepts designed with explicit regard to high specific thermal powers and easy scalability. Hence, to prove the potential of thermochemical TES, we see the need to further improve the state-of-the-art on suitable reactor concepts. However, more complex storage designs are challenging when it comes to the spatially resolved numerical modelling, which we see as one of the key tools in order to analyze and systematically enhance the reactor performance.

In this study, we focus on the aspects which determine the exergy efficiency of the thermochemical energy storage, i.e. the temperature gradients needed to operate the storage at relevant thermal powers. This is of particular importance in industrial applications, where each additional Kelvin lost due to the storage's internal temperature gradient decreases the overall efficiency and hence, the profitability of the thermal energy storage – thermal losses to the ambient not even considered.

A common assumption in the design of thermochemical TES is that the overall process is controlled by the rate of heat trans-

* Corresponding author. Tel.: +49 711 6862 8238.
E-mail address: jana.stengler@dlr.de (J. Stengler).

Nomenclature

Abbreviations

Exp.	experimental
HTF	heat transfer fluid
Sim.	simulation
TES	thermal energy storage
TGA	thermogravimetric analysis

Greek letters

α	heat transfer coefficient, $W/(m^2 \cdot K)$
γ	dimensionless parameter
ε	bulk porosity
η	dynamic viscosity, $Pa \cdot s$
λ	thermal conductivity, $W/(m \cdot K)$
ρ	density, kg/m^3
ϑ	temperature, $^{\circ}C$

Latin letters

c_p	heat capacity, $J/(kg \cdot K)$
h	level of hydration, mol/mol
$\Delta_R H$	standard molar enthalpy of reaction, kJ/mol
$\Delta_R S$	standard molar entropy of reaction, $J/(mol \cdot K)$
K	permeability, m^2
k	heat transfer coefficient, $W/(m^2 \cdot K)$
m	mass, kg
\dot{m}	mass flow, kg/s
M	molar mass, g/mol
n	molar density, mol/m^3
p	pressure, kPa
P	thermal Power, W
q	local heat flux density, W/m^2
R	universal gas constant, $8.314 J/(mol \cdot K)$
t	time, s
T	absolute temperature, K
v	velocity, m/s
V	volume, m^3
X	reaction conversion

Indices

dehyd	dehydration
g	gas
hyd	hydration
norm	normalized
s	solid
th	thermal

fer, and, more specifically, by mainly the low thermal conductivity of the reactive bulk phase, which has therefore been subject to extensive investigations and enhancement approaches. If, however, the storage design is improved towards higher specific thermal powers, the relative impact of the contact heat transfer coefficient at the bulk/heat exchanger boundary becomes increasingly important [7,8]. The contact heat transfer coefficient depends on the “arrangement” of the storage material in the reaction chamber, e.g. the shape of the reaction chamber and the application of mechanical forces during filling [9,10]. In addition, the wall heat transfer coefficient depends on the reactive material's particle size [11], and hence can be subject to change in the course of the chemical reaction. Furthermore, it might also alter during the lifetime of the storage, e.g. due to agglomeration or shrinking. E.g., Lu et al. give a conversion-dependent coefficient in the range of 150 to 550 $W/(m^2 \cdot K)$, assuming a higher value for the “discharged” material (initial state of the decomposition reaction, ammonia salt pellets) [12]. Similarly, for strontium chloride reacting with ammonia, Huang et al. give a value of 249

$W/(m^2 \cdot K)$ for the adsorption process, and 165 $W/(m^2 \cdot K)$ for desorption [13]. They report that in the case of their cylindrical reactor, the contact thermal resistance is the main limitation. At the same time, no universally valid correlations exist for the assessment of these coefficients and available literature data appear inconsistent. Most of the given values are fitted to experiments, if not their origin remains unclear or they are simply assumed to be very large, and thus non-limiting. For example, for strontium bromide hexahydrate and monohydrate, Lahmidi et al. assume a value of 1000 $W/(m^2 \cdot K)$, concluding that the heat transfer coefficient at the bulk/heat exchanger boundary does not play a major role in the overall heat transfer [10]. We draw a similar conclusion in the analysis of a calcium oxide/hydroxide TES, assuming that the low bulk thermal conductivity of the solid in a 10 mm packed bed dominates the overall heat transfer [14]. All in all, it remains unclear if and to what extent the heat transfer coefficient at the bulk/heat exchanger interface dominates the overall performance in particular in the case of high-power storage modules, which feature a complex geometry and an increased effective bulk thermal conductivity.

In contrast to some of the mentioned works, we pursue a storage design which is capable of transferring large thermal powers: by choosing a more complex heat transfer structure, we aim at minimizing the impact of the low bulk conductivity on the overall thermal performance. As a conclusion, we expect other heat transfer coefficients, particularly the wall/solid boundary, to play a more important role in the tuned-up storage design, so we focus this aspect in the present publication. As a reference reaction system, we chose the hydration and dehydration reactions of strontium bromide ($SrBr_2$), which has proven to be a potential candidate for thermochemical TES and heat transformation for a temperature range highly relevant for a broad range of industrial applications (160–320 $^{\circ}C$). In two recent publications, we have investigated the characteristic material and reaction properties of the thermochemical working pair $SrBr_2/H_2O$ [15] and the operation of a closed TES and heat transformer based on $SrBr_2$ on a 1 kW scale [16]. The experimental proof-of-concept showed that the storage can be charged at temperatures below 180 $^{\circ}C$, and discharged at temperatures above 280 $^{\circ}C$. This was achieved by raising the steam pressure, from 1 kPa during the endothermic reaction, to 560 kPa in the exothermic reaction. It was observed that the average thermal power of the scalable storage module correlates linearly with the internal temperature gradient, i.e. the temperature difference between the heat transfer fluid and the reaction temperature measured in the $SrBr_2$ bulk phase. This suggests that the storage's performance is dominated by the heat transfer rate. However, a quantitative analytical assessment of the dominating processes is hardly possible due to the complex geometry of the reactor design.

In this work, we link the two mentioned approaches – an experimental parametric study using the reactor design described in [16] and the $SrBr_2/H_2O$ reaction system characterization [15] – with a detailed simulation-based discussion on the storage's characteristic performance. We thus prove the assumption on the heat transfer limitation, and at the same time identify limiting aspects and potential for further design and operation improvements. As a tool, we establish a numerical model which includes heat and mass transfer as well as the reaction kinetics, and which we validate based on the experimental results. As discussed before, from the application's point-of-view, the most crucial optimization problem is decreasing the internal temperature gradients of the storage without decreasing the storage's thermal power. We will point out the capabilities and limits of the design chosen in [16], and thereby provide the required information for further up-scaling as well as hands-on data on the storage's performance characteristics.

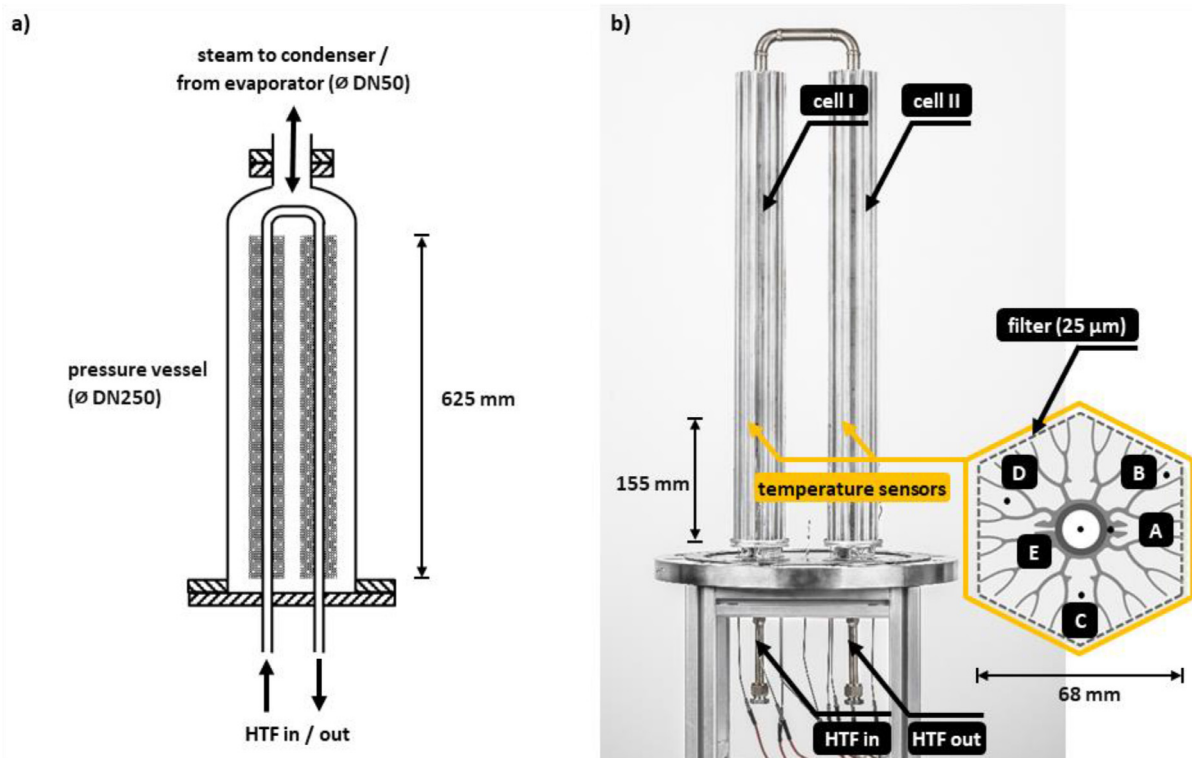


Fig. 1. Prototype of the scalable thermochemical storage module, which is divided into two separate cells arranged in series. The aluminum fins are attached on the stainless steel tube by metal clips, and are wrapped by two layers of stainless steel filter tissue (25 μm mesh size) before they are filled with the storage material. The storage contains a total $\text{SrBr}_2 \cdot \text{H}_2\text{O}$ mass of 5.059 kg. a) Schematic drawing. b) Photograph. The cells are equipped with temperature sensors at the positions indicated in the graph.

2. Methods

2.1. Experimental setup

The layout of the test rig and the storage module is described in detail in our prior publication [16]. The 1 kW storage prototype analyzed in this work (see Fig. 1) was developed under consideration of two different design aspects: firstly, high specific thermal powers, and, secondly, easy scalability for larger storage capacities and thermal powers. An important feature of the storage design are the axial aluminum fins, which are mounted onto the heat transfer fluid tube with steel clips. The fin geometry had originally been developed and optimized for a latent TES operated with sodium nitrate as phase change material for direct steam generation in the steel tube [17]. Out of the different aluminum structures proposed by Johnson et al., we chose the fin type “Axial-70” because of its higher ratio of thermal power per storage capacity (kW/kWh) compared to the other discussed fin types [17].

In the present study, the storage prototype contains approximately 5 kg of $\text{SrBr}_2 \cdot \text{H}_2\text{O}$. To investigate the temperature distribution within the bulk phase, the storage module is equipped with several temperature sensors (type Pt100, see Fig. 1b: positions A–D in the reactive medium, position E in the heat transfer fluid). Additionally, the inlet and outlet temperatures and the mass flow of the heat transfer fluid (HTF) are recorded, along with the fluid level in the evaporator/condenser. From these values, the thermal power transferred to and from the storage module and the reaction conversion, respectively, are calculated (for details on data analysis and measurement uncertainties, see [16]).

The setup for operating the storage is designed to test steam-based thermochemical storage reactors in the operation range of 1–600 kPa abs. steam pressure and up to 320°C HTF temperature. The main components of the setup are the storage and the evaporator/condenser unit, all of which are heated and cooled with ther-

mal oil as HTF. All steam-containing piping is equipped with electric heat tracing and insulation to prevent condensation. The desired water vapor pressure during charging/discharging the storage is set by the condenser/evaporator temperature.

2.2. Experimental data

In this work, we discuss different aspects of the kinetics of the chemical reaction, the steam mass transfer and the heat transfer based on the experimental results of the 1 kW prototype. We refer to two reference data sets: a charging experiment conducted at 189°C HTF temperature and 1.3 kPa steam pressure (Fig. 2a), and a discharging experiment performed at 208°C and 66 kPa (Fig. 2b). With regard to a later industrial application, the absolute pressure of the discussed charging experiment is on the very low end of potential operational states since it requires a very low condensation temperature (5°C), which requires additional cooling effort. Essentially, we chose this extreme pressure condition for the comparison because if no substantial steam mass transfer limitations are observed in this case, they will not occur at higher steam pressures due to the increasing steam densities and, thus, smaller mass flow velocities. In order to discuss the reaction progress under similar heat transfer boundary conditions for charging and discharging, the second criterion for selecting the reference experiments was the temperature difference between the HTF temperature and the pressure-dependent reaction temperature. In the two chosen reference experiments, this temperature difference is approximately 20 K.

The course of these experiments will be briefly explained in the following to give the reader a better understanding of the working principle of the TES system and the experimentally accessible data for the performance evaluation of the system. The plots given in Fig. 2 contain the pressure curve measured during the experiment, the temperature in the HTF and at several positions within

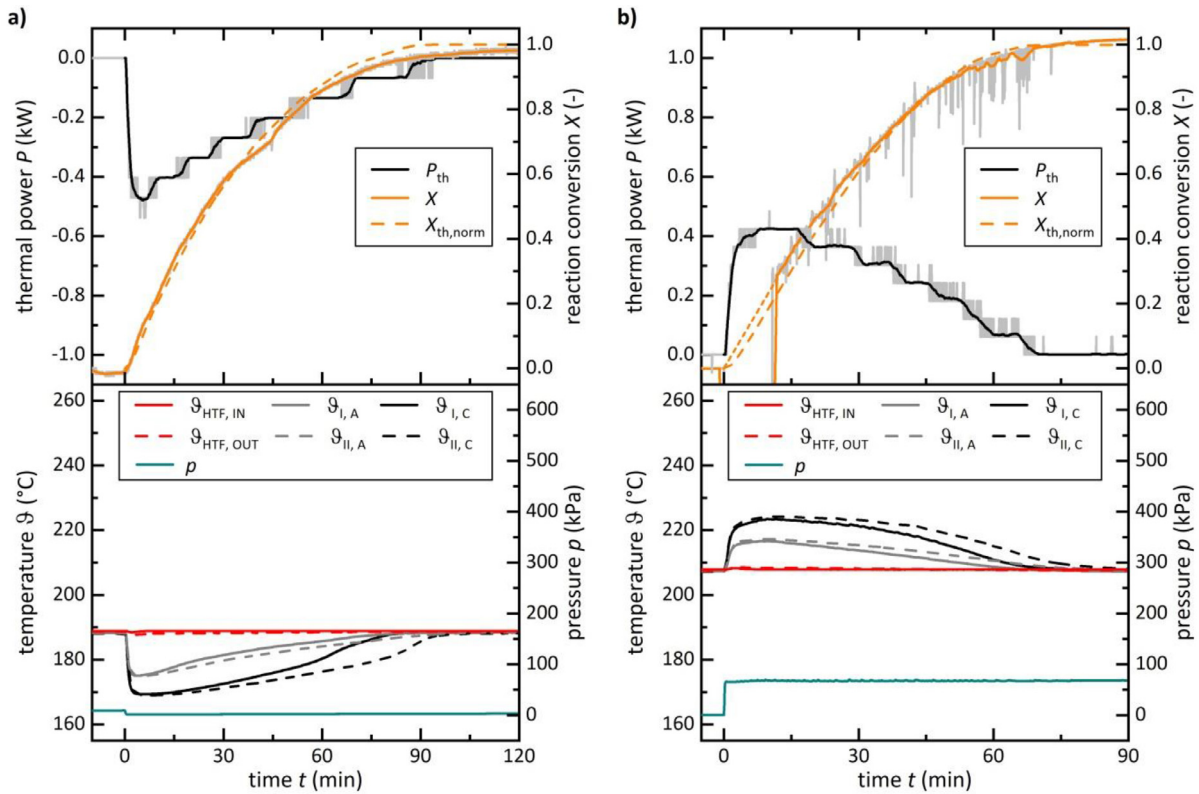


Fig. 2. Experimental results of the 1 kW prototype. The effective thermal power of the storage module P_{th} and the reaction conversion X are displayed in the upper part of the panels. For comparison, the graphs additionally contain the reaction conversion $X_{th,norm}$, which is calculated from the thermal power P_{th} . The lower panels display the temperature progression at different positions in the reactive bulk phase (positions A, C of cell I and II) as well as the HTF temperatures, and the pressure measured in the storage module. a) Charging experiment at 189°C HTF temperature (16.4 kg/min flow rate) and 1.3 kPa steam pressure. b) Discharging experiment with 208°C HTF temperature (14.4 kg/min) and 66 kPa steam pressure.

the bulk phase (lower panel), and the thermal power transferred to/from the HTF along with the overall reaction conversion (upper panel). The effective thermal power of the storage module P_{th} and the reaction conversion X data are smoothed with a 120 s moving average smoothing function; the raw data are indicated in grey.

The progression of the pressure measured in the storage module illustrates the experimental procedure: the endothermic charging reaction starts as soon as the pressure p drops when the storage module is connected to the condenser ($t = 0$ min, lower panel of Fig. 2a). The temperatures in the reactive bulk drop steeply, thus indicating that the endothermic reaction is taking place. The thermal energy required to provide the reaction enthalpy is supplied from the HTF, resulting in negative power values (upper panel). After approximately 90 minutes, the reaction conversion approaches its maximum, and, correspondingly, the temperatures in the bulk phase return to their initial values, and the effective thermal power transferred from the HTF to the storage module reduces to zero.

Reversely, in the discharging process, the temperature progression is characterized by a steep rise of the solid temperatures, indicating the exothermic reaction, which starts as soon as steam is supplied from the evaporator (Fig. 2b, lower panel). The released thermal energy is transferred to the HTF, resulting in positive values of the effective thermal power (upper panel). After 90 minutes, the storage module is fully discharged as the reaction conversion approaches the value 1, and the temperatures in the bulk phase decrease to their initial values. Please note that in this experiment, the level indicator did not read data during the first 15 minutes of the experiment, probably due to condensation on the measurement rod. In this range, the reaction conversion was therefore estimated by linear interpolation from the last available data point

($t = 0$ min) to the next available one. This is indicated by the dotted section in the $X(t)$ -progression.

Although the error propagation in the thermal power calculation results in relatively large errors (± 110 W for typical operation conditions, dominated by the error of the temperature measurement combined with the small temperature differences of approximately 0.5 to 2 K between the HTF inlet and outlet), the $X_{th,norm}$ progression shows very close agreement with the reaction conversion X obtained from the level measurement in the condenser/evaporator. In the calculation of $X_{th,norm}$ from the integration of the thermal power over the experimental time, thermal losses are neglected due to the scaling of $X_{th,norm}$ to a maximum value of 1. A more detailed discussion on the progression of the charging and discharging processes and the operating range of the storage module is presented in our prior publication [16].

2.3. Numerical model

In the numerical part of this work, a simulation study is conducted based on the finite element method (FEM) to investigate the characteristic storage performance. For this purpose, a 2D radial cross-section of the heat transfer structure filled with the reactive bulk phase is implemented in COMSOL Multiphysics®. Given the symmetrical design, a quarter of the aluminum structure is chosen as a representative segment. We use a time-dependent solver with a varying time step size ranging from 0.5 s during the initial phase of the reaction to 10 s towards the end of the process time. The 2D cross-section of the heat exchanger is resolved with an adaptive triangular mesh with approximately 11,300 elements and a maximum element size of 0.5 mm. While we found that the mesh could be coarser and still give identical global results (such

Table 1
Physical and chemical properties of the SrBr₂/H₂O reaction system.

Category	Parameter	Value	Reference
solid properties	SrBr ₂ density $\rho_{s,0}$	4216 kg/m ³	literature data [25]
	SrBr ₂ ·H ₂ O density $\rho_{s,1}$	3911 kg/m ³	linear interpolation between SrBr ₂ and SrBr ₂ ·6H ₂ O densities from [25]
	SrBr ₂ specific heat capacity $c_{p,s,0}$	75.35 J/(mol·K)	literature data [26]
	SrBr ₂ ·H ₂ O specific heat capacity $c_{p,s,1}$	120.9 J/(mol·K)	literature data [26]
bulk properties (SrBr ₂ and SrBr ₂ ·H ₂ O)	SrBr ₂ molar mass $M_{s,0}$	247 g/mol	literature data [26]
	bulk porosity ϵ	0.66 (SrBr ₂ ·H ₂ O)–0.71 (SrBr ₂)	fitted to the SrBr ₂ ·H ₂ O mass contained in the specific reactor setup [16]
	permeability K	1·10 ⁻¹⁰ m ²	literature data on SrBr ₂ ·H ₂ O [19]
	thermal conductivity λ_{bulk}	0.4 W/(m·K)	range of 0.2–0.6 W/(m·K) given for SrBr ₂ ·H ₂ O [19] and SrBr ₂ [21] for temperatures up to approximately 70°C
hydration reaction (SrBr ₂ to SrBr ₂ ·H ₂ O)	enthalpy of reaction $\Delta_R H$	71.98 kJ/mol	calculated from literature data on enthalpy of formation [26]
	entropy of reaction $\Delta_R S$	143.93 J/(mol·K)	calculated from literature data on entropy of formation [26]

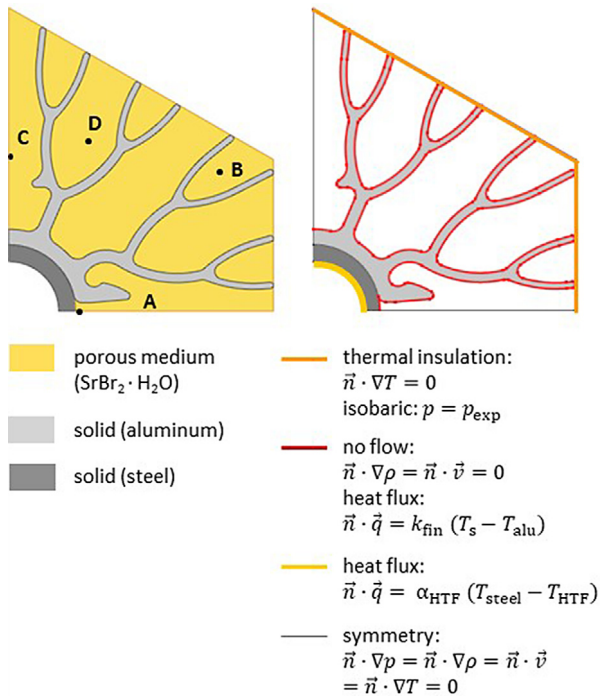


Fig. 3. Model domains and boundary conditions, with heat and mass transfer in the porous medium, and heat transfer in solids (aluminum and steel). Here, \vec{n} refers to the normal vector. On the outer boundary of the porous medium domain, thermal insulation, steam flux, and no transport of reactive solid are set as boundary conditions. The heat flux from the porous medium to the aluminum structure is characterized by the heat transfer coefficient k_{fin} . The heat flux from the steel tube to the heat transfer fluid is described with the heat transfer coefficient α_{HTF} . The inner boundary between the aluminum and the steel domains is assumed with no additional heat transfer resistance. Due to symmetry reasons, no flux is assumed at the lower and the left boundary or symmetry axis. For details on the design and the dimensions of the aluminum fins, please refer to Johnson et al. [17]. The positions A–D correspond to the temperature probe positions indicated in Fig. 1b.

as the global reaction conversion), the chosen mesh resolution is needed to avoid mesh artefacts when analyzing local effects (such as the local rate of reaction).

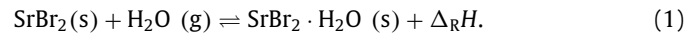
The model domains and boundary conditions are described in Fig. 3. The integral results for the 3D experimental setup are obtained by scaling the 2D numerical results with the total length of the two cells, hence, disregarding any influence of the connection pipe, and assuming the absence of axial temperature gradients. Since there are no temperature gradients in the gas phase

along the cell length, and the temperature gradients in the HTF are small compared to the radial temperature differences in the reactive bulk, this approach is justified.

In the following, we describe the underlying physics starting with the chemical reaction model, and then proceeding towards the mass and energy transport phenomena. The relevant physical processes are modelled under the assumption that the bulk phase does not change during the reaction phase in terms of its total volume and outer shape, while its “inner properties”, specifically the porosity ϵ and heat capacity c_p , depend on the hydration level. The permeability K and thermal conductivity λ_{bulk} are assumed to be time-independent and homogeneously distributed. Relevant SrBr₂ and SrBr₂·H₂O properties are either derived from literature data or own measurements, see summary in Table 1.

2.3.1. Reaction rate model

For a distinct operation range (150–210°C, 0–97 kPa), we developed empirical first-order rate models for the hydration and the dehydration reaction of SrBr₂ based on thermogravimetric analysis (TGA) measurements, see our previous work [15]:



In addition, the temperature-dependent reaction pressures p_{dehyd} and p_{hyd} were analyzed from experiments conducted in a different lab-scale setup [18,15]. In these experiments, it was observed that a thermal hysteresis occurs between the hydration and the dehydration reaction. For this reason, we use the term “pressure-dependent reaction temperature” when we refer to the apparent thermodynamic equilibrium. The relevant empirical correlations for the reaction rate models and reaction temperatures from [15] are summarized as follows:

Dehydration reaction:

$$\frac{dX}{dt} = (1.38 \cdot 10^6 \text{ s}^{-1}) \exp\left\{-\frac{75.7 \text{ kJ/mol}}{RT}\right\} (1-X) \left(1 - \frac{p}{p_{\text{dehyd}}}\right)^{0.25} \quad (2)$$

with

$$\log(p_{\text{dehyd}}/p^+) = 14.69 - (6.41 \cdot 10^3 \text{ K}) \frac{1}{T} \quad (3)$$

Hydration reaction:

$$\frac{dX}{dt} = (1.60 \cdot 10^{-3} \text{ s}^{-1}) (1-X) \left(\frac{p}{p_{\text{hyd}}} - 1\right)^{1.8}, \quad (4)$$

with

$$\log(p_{\text{hyd}}/p^+) = 8.18 - (3.19 \cdot 10^3 \text{ K}) \frac{1}{T} \quad (5)$$

In Eq. (3) and Eq. (5), p^+ refers to the reference pressure of 1 kPa. Except for Eq. (4), these equations were implemented in the numerical model as written. The hydration rate model had to be modified for reasons that will be discussed in the results section, and was finally implemented in the numerical model in the following form:

$$\frac{dX}{dt} = 3.04 \cdot 10^{-5} \text{ s}^{-1} (1 - X) \left(T(\rho_{\text{hyd}})/K - T/K \right)^{1.79}. \quad (6)$$

2.3.2. Phase transition

The solid mass of the porous bulk phase changes due to the chemical reaction, which proceeds with the effective rate dX/dt , and so do the density and other physical properties. Note that for both, dehydration and hydration reaction, we follow the convention that the reaction conversion X proceeds from 0 to 1. Therefore, in the model, all property changes are implemented as a function of the hydrate level h to keep consistent governing equations for both charging and discharging. Correspondingly, the hydrate level h runs from 1 to 0 in the case of the dehydration reaction, and from 0 to 1 during hydration:

$$h = \begin{cases} X, & \text{hydration} \\ 1 - X, & \text{dehydration} \end{cases}. \quad (7)$$

Due to the solid's mass and density change from the monohydrous to the anhydrous state, the porosity ε is assumed to change during the charging and discharging process, as, by our definition, the overall bulk volume is assumed constant:

$$\varepsilon = \varepsilon_0 + h(\varepsilon_1 - \varepsilon_0). \quad (8)$$

The porosity of the bulk in its monohydrate state ε_1 is fitted to match the mass of $\text{SrBr}_2 \cdot \text{H}_2\text{O}$ contained in the experimental setup. From ε_1 , the porosity of the bulk in its anhydrous phase is determined by:

$$\varepsilon_0 = 1 - (1 - \varepsilon_1) \frac{\rho_{s,1} M_{s,0}}{M_{s,1} \rho_{s,0}}, \quad (9)$$

with the densities ρ_s and the molar masses M_s of the anhydrous phase (index 0) and the monohydrous phase (index 1), respectively. With ε_0 , we define the volumetric molar number of the SrBr_2 molecules taking part in the chemical reaction, n_0 :

$$n_0 = (1 - \varepsilon_0) \frac{\rho_{s,0}}{M_{s,0}}. \quad (10)$$

2.3.3. Steam mass balance

Due to the gas-solid reaction, steam is either consumed by the bulk phase (hydration reaction) or released from it (dehydration reaction). Hence, a steam mass source, which is linked to the effective rate of reaction dX/dt , is implemented in the porous medium model domain:

$$\frac{\partial}{\partial t} (\varepsilon \rho_g) + \nabla \cdot (\rho_g \vec{v}) = \frac{dX}{dt} n_0 M_{\text{H}_2\text{O}}, \quad (11)$$

with \vec{v} being the superficial velocity of the steam flowing in the direction of \vec{x} . Concerning the mass transfer of steam, one will have to distinguish between two processes: the transfer of steam within the porous bulk phase, and the transfer of steam within the SrBr_2 and $\text{SrBr}_2 \cdot \text{H}_2\text{O}$ granules via micro- and nano-pores. While the first process is explicitly included in our numerical model by the above-mentioned Eq. (11), the latter can within the experiments from [15] not be distinguished from the kinetics of the reaction itself. More specifically, it is implicitly accounted for during the determination of the effective reaction rates, which were experimentally investigated in thermogravimetric measurements of the same kind of granules which were also used in the 1 kW prototype. The adsorption of water vapor on the particle surface or intraparticle diffusion processes are therefore included in the empirical reaction rate models.

2.3.4. Momentum balance

As described above, our model only explicitly includes the interparticle mass transfer of steam within the reactive bulk phase, which is described as a porous solid. Usually, porous media are characterized by their specific permeability K (m^2). For different salt hydrate packed beds, the permeability varies in the range of approx. 10^{-8} – 10^{-12} m^2 . For $\text{SrBr}_2 \cdot \text{H}_2\text{O}$, Michel et al. report a permeability of $1 \cdot 10^{-10}$ m^2 [19], which we will use as reference in this publication. The momentum balance is solved by Darcy's law for steam flowing through the porous bulk phase in the direction of the flow [20]:

$$\vec{v} = - \frac{K}{\eta_g} \nabla p, \quad (12)$$

with η_g being the dynamic viscosity of steam. According to Darcy's law, the average fluid velocity \vec{v} is proportional to the permeability K of the porous media and the pressure drop in the direction of the flow. Since in the experiment, the steam pressure p is controlled by the set evaporator/condenser temperature, the pressure recorded during the experiment is defined as boundary condition on the outer bound of the modelling domain.

2.3.5. Energy balance

The model considers the transfer of thermal energy from the HTF to the steel tubing and aluminum structure, and then to and within the solid bulk phase. Heat radiation is neglected as the temperature differences within the observed model domains are small. Furthermore, we assume local thermal equilibrium between the gas and the solid phase within the porous medium. The chemical reaction is implemented as a heat source (exothermic discharge reaction) or heat sink (endothermic charge reaction) in the reactive solid, with the molar reaction enthalpy of $\Delta_R H = 71.98$ kJ/mol. Here, the specific isobaric heat capacity of the solid $c_{p,s}$, and the reaction enthalpy are assumed to not change with the temperature:

$$\begin{aligned} (\varepsilon \rho_g c_{p,g} + (1 - \varepsilon) \rho_s c_{p,s}) \frac{\partial T}{\partial t} + \rho_g c_{p,g} (\vec{v} \cdot \nabla T) \\ - \nabla \cdot (\lambda_{\text{eff}} \nabla T) = - \frac{dX}{dt} n_0 \Delta_R H. \end{aligned} \quad (13)$$

The effective thermal conductivity of the porous medium is composed of the conductivities of steam and the porous solid matrix:

$$\lambda_{\text{eff}} = \varepsilon \lambda_g + \lambda_{\text{bulk}}. \quad (14)$$

From literature data on SrBr_2 and $\text{SrBr}_2 \cdot 6\text{H}_2\text{O}$ measured at temperatures up to 70°C it is expected that the thermal conductivity increases during the hydration process of SrBr_2 [21]. However, since there is no literature data available on the thermal conductivities of a SrBr_2 and $\text{SrBr}_2 \cdot \text{H}_2\text{O}$ bulk phase in the relevant porosity and temperature range, we have simplified the model in this regard. Hence, it does not consider changing bulk conductivities due to the transformation from the monohydrate to the anhydrous phase, or due to porosity changes. It will be seen from the thermal sensitivity studies in the results section that this has a negligible impact on the overall simulation results for the given storage geometry. In contrast, the model does consider that the solid's heat capacity $c_{p,s}$ depends on the hydration level, same as the density ρ_s :

$$c_{p,s} = c_{p,s,0} + h(c_{p,s,1} - c_{p,s,0}), \quad (15)$$

$$\rho_s = \rho_{s,0} + h(\rho_{s,1} - \rho_{s,0}), \quad (16)$$

with $c_{p,s,0}$ and $\rho_{s,0}$ being the properties of the anhydrous phase, and $c_{p,s,1}$ and $\rho_{s,1}$ the properties of the monohydrous phase based on the literature data given in Table 1.

The temperature-dependent steam properties (ρ_g , λ_g , $c_{p,g}$, η_g) are taken from the COMSOL Multiphysics® material database. The heat exchanger domains are characterized by the physical properties of stainless steel 1.4404 and aluminum 6060 (stainless steel 1.4404: $\rho_{\text{steel}} = 8000 \text{ kg/m}^3$, $c_{p,\text{steel}} = 500 \text{ J/(kg}\cdot\text{K)}$, $\lambda_{\text{steel}} = 15 \text{ W/(m}\cdot\text{K)}$; aluminum 6060: $\rho_{\text{alu}} = 2700 \text{ kg/m}^3$, $c_{p,\text{alu}} = 900 \text{ J/(kg}\cdot\text{K)}$, $\lambda_{\text{alu}} = 220 \text{ W/(m}\cdot\text{K)}$). The stainless steel filter tissue enclosing the aluminum fins is not considered in the model.

2.3.6. Heat transfer boundary conditions

The local heat flux density at the interfaces between the heat transfer fluid (HTF) and the steel tube as well as between the aluminum fins and the reactive bulk is given by

$$q = \alpha_{ij} (T_i - T_j), \quad (17)$$

for the two domains i and j . T_i and T_j refer to the local domain temperatures right at the boundary, with α_{ij} being the corresponding heat transfer coefficient (see Fig. 3). α_{HTF} is derived from the Gnielinski empirical model for turbulent flow [22]. The HTF fluid properties are taken from the supplier's datasheet. Since the aluminum fins are tightly attached onto the steel tubing, there is no additional heat transfer resistance assumed at the steel/aluminum interface. Thermal insulation boundary conditions are assumed at the outer boundary of the porous media domain. Please note that no temperature continuity is assumed at the interface between the aluminum fins and the reactive bulk. In the experiment, a small gap may arise between the two domains (aluminum and porous medium) due to shrinking and swelling of the thermochemical material. Since the size of the gap is unknown and expected to change during the chemical reaction, it is implemented as a discrete heat transfer resistance at the boundary, and not as a volumetric domain. Hence, the heat transfer coefficient k_{fin} at this interface has a special role within this setting since it is crucial to understand the overall system performance, as we will see in the later chapters. However, there are no suitable correlations available from the literature. Therefore, the coefficient k_{fin} is obtained empirically by fitting of the numerical model with corresponding experimental data. This will be discussed in detail in the results section.

2.3.7. Implementation of the experimental operating conditions

The experimental pressure data are included as boundary condition into the model after being processed with a 120 s moving-average smoothing function. As the pressure sensor is installed right behind the ball valve connecting the storage vessel with the condenser/evaporator, and not inside the reactor vessel itself, the measured pressure increase in the case of the discharge process is smoothed by a restricted-growth pre-factor to account for the steam transport from the sensor position to the reactor ($1/60 \text{ s}^{-1}$ time constant, approx. 90% of the full pressure is reached after 120 s). In case of the charging process, experimental pressure data are smoothed with a 1440 s moving-average smoothing filter in order to remove digitization artefacts from the 0.2 kPa readout accuracy (starting from $t = 0 \text{ s}$). The initial values for the temperatures are derived from the experimental data (mean values of the bulk temperatures). Numerical probe points are implemented at those positions where Pt100 sensors have been installed in the corresponding experimental setup for direct comparison. For both cells, the same 2D model is used, with the only difference being the HTF temperature from the experiment that was used as input parameter for the simulation.

3. Results

In the following, we discuss the analysis of the storage's performance based on the model described in the previous section. In order to structure the discussion, we start from local aspects, such

as the temperature and reaction propagation within the reactive bulk and conclude with integral aspects, such as the overall thermal performance of the storage during charging and discharging.

3.1. Local aspects: temperature and reaction rate progression

Except for the heat transfer coefficient k_{fin} describing the aluminum/bulk-boundary, all physical properties are taken from literature values or own experimental data, see Table 1. To assess the unspecified parameter k_{fin} , the numerical model was "calibrated" to the experiments by fitting k_{fin} as a function of the level of hydration, h , which proceeds from 1 to 0 in the case of the charging process, and from 0 to 1 during discharging. It was found that the parameter

$$k_{\text{fin}} = (30 + 15h) \text{ W/(m}^2 \cdot \text{K)} \quad (18)$$

yields close agreement between the simulation results and the experimental data, both for charging and discharging. In the Appendix (Fig. A1), we give additional simulation results obtained for wall heat transfer coefficients independent of the hydrate level h , which led us to the resulting correlation in Eq. (18). The dependence of the wall heat transfer coefficient on h can be intuitively understood as the solid bed swells and shrinks due to the chemical phase change from the anhydrous state to the monohydrate state and reverse. This behavior can be directly derived from the literature data on the density (Table 1): the decrease in density for the hydrate with respect to the anhydrate indicates a volume change in addition to the water uptake. Apart from that, in the experiment, the solid is found to have agglomerated (see [16]), hence, it is likely that gaps form between the reactive phase and the aluminum fins, with the gap size varying while the solid "breathes" during the reaction. Unfortunately, the details of the gap formation will underlie strong local variations such as porosity inhomogeneities, in addition to the substantial uncertainties on the corresponding parameters (e.g. local volume change). Hence, we will only include this effect via the effective behavior from Eq. (18), knowing that the local conditions may vary significantly from the behavior as described by our model.

Compared to the literature values mentioned in the Introduction, the obtained correlation results in relatively small values of k_{fin} . For example, among the cited references, Mazet et al. give the smallest heat transfer coefficient of $100 \text{ W/(m}^2 \cdot \text{K)}$, which is experimentally determined for a mixture of salts reacting with ammonia. Based on their simulation work, they report a minor effect on the overall thermal power of their cylindrical reactor concept [23].

3.2. Charging process

The comparison of the experimental and numerical results for the charging process is given in Fig. 4. In the upper part, the panel displays the local temperature propagation at the measurement positions over time. The experimental data originates from the experiment displayed in Fig. 2a. Here, the plot contains all four probe positions of the first of the two serially arranged storage cells. Supplementary, the reaction temperature (ϑ_{dehyd}) is plotted, which is determined from the experimental pressure curve and Eq. (3). Since the pressure increases over time, so does the reaction temperature. In addition to the temperatures, the numerically determined local reaction rates dX/dt are indicated in the lower panel. While these data cannot be determined directly from the experiment, they allow to better understand the local temperature progression.

Although small deviations between the experimental temperature probe positions and the numerical cut point definitions cannot be excluded, the simulated data reproduces the overall temperature trend in close agreement: as soon as the steam pressure-induced reaction temperature ϑ_{dehyd} falls below the initial solid

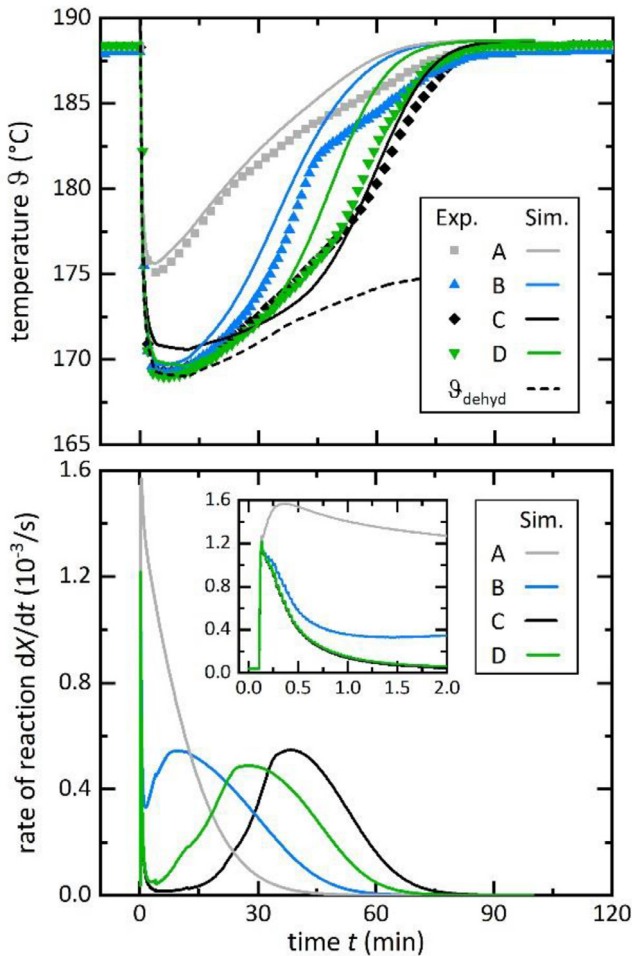


Fig. 4. Validation of the simulation results for the reference charging process (188.7°C HTF temperature, 1.3 kPa average steam pressure, 16.5 kg/min HTF mass flow). The upper panel shows the temperature progression at the different bulk positions measured in storage cell I (markers) in comparison to the simulation results (line plots) at the corresponding locations indicated in Fig. 1b and Fig. 3, respectively. For reference, the plot contains the dehydration reaction temperature (θ_{dehyd}), which is calculated from the experimental pressure curve. The lower panel gives the reaction front propagation through the bulk phase in terms of the local rate of reaction, which is determined from the numerical simulation.

temperature, the endothermic reaction in the bulk phase starts. During the initial phase of approximately 30 seconds, which can be seen as simultaneous peaks in the reaction rate curves, the reaction proceeds simultaneously at all positions while the bed is cooling down (see zoom into the effective reaction rates in the lower panel). Hence, this first time regime, reaching from $t = 0$ min until the time when the pressure-dependent dehydration reaction temperature is reached (approx. $t = 5$ min) is dominated by the effective rate of reaction. This phase terminates when the solid phase reaches the pressure-dependent reaction temperature.

The consecutive phases can be best understood looking at one of the specific positions C or D (compare Fig. 3). There, after reaching the reaction temperature, the reaction almost stops. This is essentially caused by the effect that the bulk’s sensible thermal energy is consumed by the endothermic reaction, while at the same time, the heat flux from the HTF apparently only drives the reaction in bulk regions closer to the heat exchanger surface, e.g. positions A and B. The outer regions of the reaction bed (close to the heat exchanger surface) “shield” the inner areas from heat transfer, and hence, hinder the course of the reaction at these positions. E.g. in the case of position C, this second phase takes approx. 20 min

($t = 5\text{--}25$ min) with negligible local conversion (3–5%, graph not shown).

In the third phase, all outer sections will have reached a high conversion level, so that the heat flux exceeds their enthalpy intake. Hence, the reaction proceeds at higher rates also in the inner regions of the bulk phase that are further away from the heat exchanger surface (position C: approx. from $t = 25\text{--}45$ min, 5–50% local reaction conversion). This phase is not occurring simultaneously at the different locations. Instead, it proceeds through the reaction bed as a reaction front. Following a first-order rate law, the effective reaction rate decreases if the local reaction conversion approaches the value 1, see Eq. (2). Consequently, as soon as the rate of reaction is smaller than the local heat transfer kinetics, the temperatures start to increase at a higher rate (position C: approx. from $t = 45\text{--}75$ min, 50–99% local reaction conversion).

At a certain moment, the reaction will have reached full conversion, or, in other words, the monohydrate is fully decomposed into the anhydrous phase and steam. In this fourth and last phase, the local temperature approaches its initial value, and sensible energy increase is the dominating process. E.g. in the case of position C, this fourth phase reaches from approx. $t = 75\text{--}90$ min, with no more change in the local conversion (99–100%).

The overall reaction progression and the different phases can be seen in the 2D plots given in Fig. 5, which display the level of hydration, the rate of reaction, and the temperature progression at specific time steps (10 s, 60 s, 15 min, and 45 min). Although the temperature distribution in the first 15 min of the charging process is rather homogenous (Fig. 5a), it is revealed that this is not the case for the local reaction rates (Fig. 5b) and the resulting level of hydration (Fig. 5c). At the beginning of the charging process, after the overall bed temperatures have dropped to their minimum, the dehydration reaction proceeds following the shape of the aluminum structure. Even if the differences in the local distance to the next heat transfer surface are on the mm-scale, there are still “dead zones” in the largest compartments. Summing up the analysis on the charging process, we observe the storage performance to be mainly dominated by the rate of heat transfer. This will be investigated in more detail in the later discussion of integral aspects of the storage performance (see section 3.2).

3.3. Discharge process

Same as in the prior discussion of the charging process, a simulation was performed with the operation parameters of the reference experiment (HTF temperature and mass flow, steam pressure, see Fig. 2b) as boundary conditions. The parameters relevant for the heat and mass transfer (K , λ , k_{fin}) remained at identical values as in the charging process simulation.

However, in contrast to the prior discussed charging process, we observed that the simulation could not reproduce the experimental data: with the hydration reaction rate model implemented as described in Eq. (4), the simulation results yielded in lower bulk temperatures and significantly larger discharging times than expected from the experiment. This indicates that the reaction rate model underrates the effective rate coefficients. Therefore, based on a maximum error estimation in the empirical model parametrization, the hydration reaction rate model was modified as given in Eq. (6) (see Appendix for a detailed discussion). As can be seen from the data given below and in the Appendix, the latter scenario yields close agreement of the numerical model with the experimental observations. Hence, Eq. (6) is considered valid for the remainder of this study.

With the modified rate model, the qualitative temperature progression in the reactive bulk is closely reproduced by the simulation, even if the maximum temperatures are slightly higher than in the experiment (Fig. 6, upper panel). Just like it is observed in the

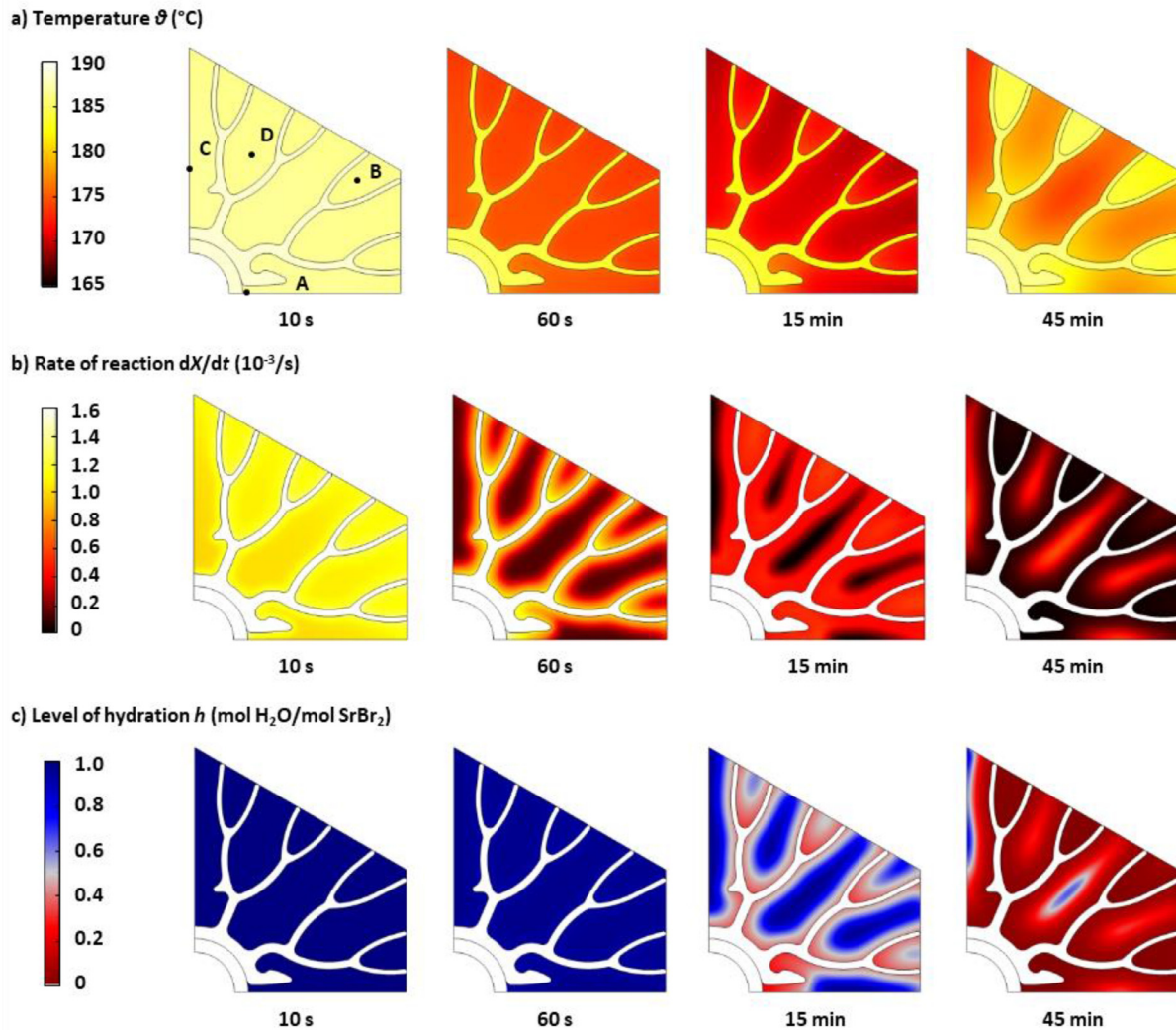


Fig. 5. 2D plots of the simulation results for the reference charging process. After the temperatures have uniformly decreased towards the characteristic plateau in the first phase of the endothermic process ($t = 10$ s), the chemical reaction propagates through the porous bulk starting from areas near the aluminum fins. For the specific position C, located in the center of the largest bulk compartment, the time steps correspond to the second phase ($t = 60$ s and $t = 30$ min), and the third phase of the charging process ($t = 45$ min). a) Temperature progression. b) Rate of reaction. c) Level of hydration.

experiment, the simulated temperature curves closely follow the “shape” of the maximum reaction temperature which is calculated from the pressure curve. Small pressure fluctuations in the experiments, which can occur due to changing evaporation temperatures, directly appear in the temperature progression.

Notably, different than in the charging experiment, the temperatures do not reach the reaction temperature expected for the given steam pressure (approx. 229°C), but stay at a lower plateau. This can be explained by the effective rate of the hydration reaction, which drastically slows down when the bulk phase approaches the pressure-dependent reaction temperature (see Fig. A2 in the Appendix, $\Delta T \rightarrow 0$ K). Please note that if no heat flux to the HTF is enabled (e.g. by stopping the HTF flow), the bulk temperatures reach the expected pressure-dependent reaction temperature (see Fig. A4 in the Appendix for corresponding experimental and simulation results), which proves the empirical correlation given in Eq. (5). As the occurrence of an offset between the bulk temperatures and ϑ_{hyd} is correctly described by the simulation, we conclude that the numerical model reproduces a correct ratio of the heat transfer rate and the rate of the hydration reaction.

Similarly to the charging process, the discharging process can again be interpreted as a sequence of four time regimes dominated by different mechanisms: first, a reaction kinetics-dominated regime which determines the time until the characteristic temperature plateau is reached, followed by a heat transfer-dominated time regime. Within the third phase, the effective rate of reaction decreases while proceeding towards the full conversion to the monohydrate state. Finally, the discharge process is concluded by the cool-down phase after the chemical reaction ended. Note that the four phases cannot be separated as clearly as this was the case for the charging process, but the general trends remain the same. More specifically, the local effective reaction rates at the different bulk positions do not show a “one after the other”-behavior, but a more homogenous distribution within the reactive bulk (Fig. 6, lower panel). This observation is confirmed by the 2D plots displayed in Fig. 7 in analogy to Fig. 5. It is an interesting finding that compared to the charging process there are no “dead zones” where for a certain period of time the reaction rate drops to values close to 0. To our understanding, this is explained by the overall lower rate of the hydration reaction which is outperformed by the heat transfer rate. Hence, since the bulk temperatures do not reach

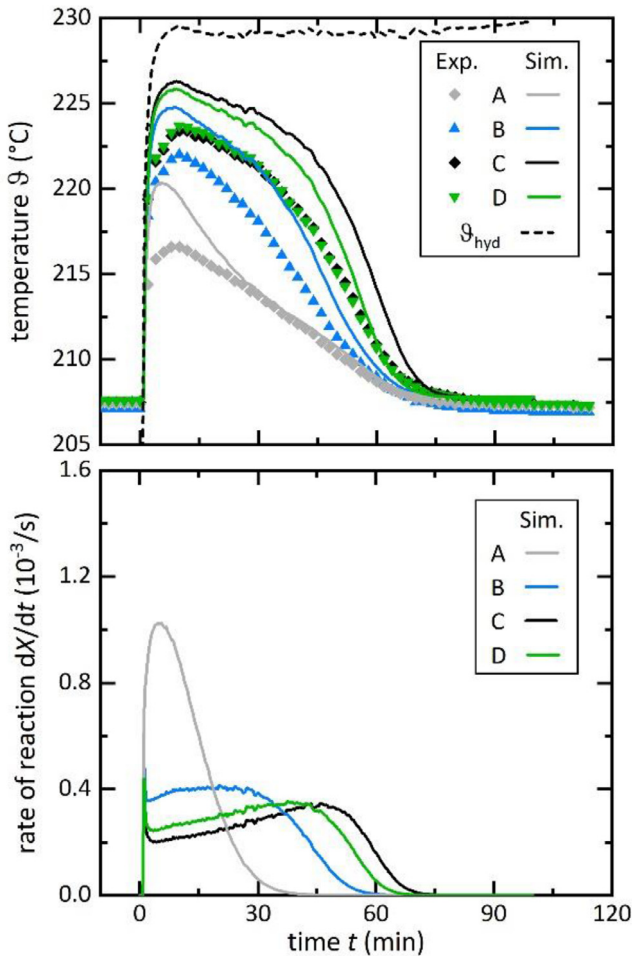


Fig. 6. Validation of the simulation results for the reference discharging process (207.8°C HTF temperature, 67 kPa average steam pressure, 14.4 kg/min HTF mass flow). The upper panel shows the temperature progression at the different bulk positions measured in storage cell I (markers) in comparison to the simulation results (line plots). For reference, the plot contains the hydration reaction temperature (ϑ_{hyd}), which is calculated from the experimental pressure curve. The lower panel gives the reaction front propagation through the bulk phase in terms of the local rate of reaction, which is determined from the numerical simulation.

ϑ_{hyd} at any time during the discharge process, “dead zones” as seen in the charging process do not appear.

All in all, based on the comparison of the local temperature distributions during the charging and discharging phase, it can be stated that the numerical model can be successfully validated by the experimental data. In this context, it is important to mention that the sole parameter used for the fitting of the numerical model with the experimental data is the heat transfer coefficient k_{fin} . Despite the complex and also partly competing physical processes, it is possible to correctly reproduce the storage behavior with regard to the discussed local aspects. Thus, in the next section, we extend the analysis to the integral performance of the storage.

3.4. Integral aspects: thermal power and overall reaction conversion

So far, we have discussed the results of a 2D simulation in comparison with results from experimental data based on local temperature distributions in one cut plane. In the following section, we will extend the analysis by the integral (3D) performance of the storage module, such as the thermal power and the overall reaction conversion. As described in section 2.2, there are two independent ways to experimentally assess the global performance of the

storage: first, the reaction conversion X , which is determined from the fluid level measurement in the condenser/evaporator, and, secondly, the measurement of the thermal power P_{th} transferred to the HTF. This is why we discuss the simulation results in these two variables, even if they are directly corresponding to one another in the model. The experimental thermal power curves $P_{\text{th,norm}}$ are scaled so that their integral values meet the theoretical capacity of the storage module of 1374 kJ, in order to account for unavoidable thermal losses to the ambience (which average approximately 15% of the capacity due to the relatively small set-up). Correspondingly, the experimental reaction conversion X_{norm} is normalized to a value of 1 for comparison with the simulation results.

In the following sections, we focus on aspects which are not implemented in the numerical model and therefore represent potential error sources, such as local inhomogeneities within the bulk phase, and effects due to the axial HTF temperature gradients. Obviously, these effects are not limited to either the discharging or the charging process. However, they will be discussed only once, in the context where their impact is most prominent.

3.5. Charge process

3.5.1. Axial temperature gradients on the HTF side

Concerning the experimental conditions at the outer boundary of the storage cells, i.e. the steam temperature and pressure, no gradients are expected to arise along the cells’ total length. However, axial temperature gradients exist at the storage cells’ inner boundary: In the experimental setup, the thermal power transferred to the HTF is calculated from the temperature difference between the HTF inlet and outlet. Typical temperature differences are in the range of approximately 0.5 to 2 K. Obviously, this axial thermal gradient is not represented in the 2D model. Exemplarily, in order to give an indication on the magnitude of the effect on the integral performance, the local temperature progression for the original HTF temperature (188.7°C) along with a 2 K lower HTF temperature is displayed in Fig. 8 in the upper panel. This graph contains the experimental temperature data recorded in the first and the second storage cell (positions I-II,A and I-II,C). In the experiment, we observe a delay time between cell I and II of about 15–30 min. Judged by the simulation results, the delay time of cell II can be reproduced with an approx. -2 K lower HTF temperature, indicating that the storage’s performance is sensitive to even small axial temperature gradients. The same effect occurs in the discharge process, where the HTF temperature increases due to the exothermic reaction. The corresponding reaction conversions are plotted in the lower panel.

While in this experiment, the magnitude of the axial temperature gradients is not critically impacting the overall performance, they need to be taken into account for large-scale storages. This is especially important for large-scale applications where the storage is operated with sensible heat transfer fluids and larger temperature differences, e.g. -10 K, as chosen in Fig. 8. For comparison, the graph contains additional experimental data from a charging experiment conducted at 178.7°C HTF temperature and the same condenser settings as the reference experiment. As the plot suggests a reasonable agreement of numerical and experimental data, the model can be used as a first approximation for these effects. However, it should be noted that the 2D model does not fully reflect the experimental situation: first, the HTF temperature is assumed constant over time, and, second, the reaction conversion refers to one specific cut plane of the storage cell. In this way, the simulated reaction conversion curves with lower HTF temperatures reflect the conversions in a 2D cross-section e.g. at the end of a large-scale storage.

Summing up the analysis on the axial temperature gradients with regard to designing storages for large-scale applications op-

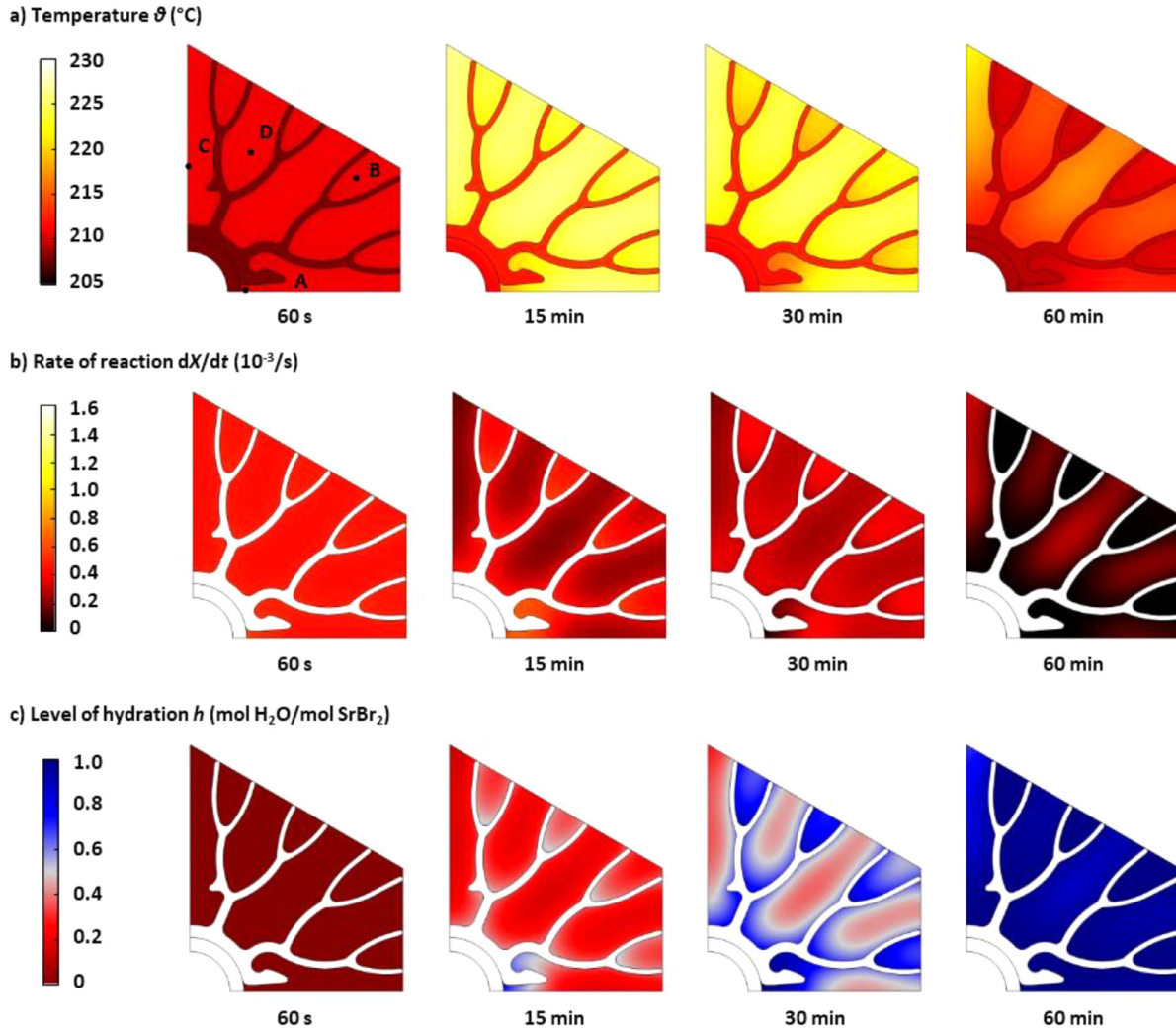


Fig. 7. 2D plots of the simulation results for the reference discharging process. After the temperatures have uniformly increased towards the characteristic plateau in the first phase of the exothermic process, the chemical reaction propagates through the porous bulk starting from areas near the aluminum fins. However, compared to the charging process, the reaction spreads more homogenously, leaving no distinctive “dead zones” where the reaction proceeds later than in the other areas. Except for the temperature plot, the axes are scaled identically as for charging to be able to directly compare the results. a) Temperature progression. b) Rate of reaction. c) Level of hydration.

erated with sensible HTFs such as thermal oil, we conclude that a parallel arrangement of several storage modules is advantageous compared to serial arrangements. Best-case is an operation with a phase-changing HTF, e.g. condensing steam for charging the storage.

3.5.2. Macroscopic changes in the bulk phase

In the experiments, we observed that the initially loose granules of the reactive bulk agglomerate in the reaction chamber [16]. At the same time, cracks form in the agglomerated structure (Fig. 9). Both effects might affect the overall bulk permeability, and cause local deviations. As these are difficult to investigate experimentally, we compare the overall storage performance for different homogenous permeability values implemented in the numerical simulation. This way, we are not able to resolve local effects, but can at least empirically describe the effect on the integral performance of the storage.

Fig. 10 gives the simulation results of the reference charge experiment, with the thermal power in the upper panel, and the reaction conversion displayed in the lower panel. The permeability is varied from $1 \cdot 10^{-9} \text{ m}^2$ to $1 \cdot 10^{-11} \text{ m}^2$. From this comparison,

one may get the impression that a lower effective bulk permeability should have been chosen for the simulation to account for macroscopic changes in the bulk phase. However, a permeability lower than $1 \cdot 10^{-10} \text{ m}^2$ is not indicated by the temperature progressions in the 2D cross-section of the reactive bulk (see discussion of Fig. 4; corresponding data for higher and lower permeability values are given in the Appendix in Fig. A5 and Fig. A6, respectively).

While the initial phase of the charging process is reproduced in sufficient approximation in all cases, the model over-estimates the overall charging progression for later process times, both in terms of $P_{th, norm}$ and X_{norm} . However, at this point, we cannot distinguish if this is an artefact from the experimental procedure, e.g. caused by a blockage of the condenser vessel with non-condensable gases which could have led to limited condensing rates (see bend in the experimental reaction conversion data at $t = 45 \text{ min}$).

3.6. Discharge process

In the previous case of the charging process, the unknown effective bulk permeability resulted in an uncertainty in the simula-

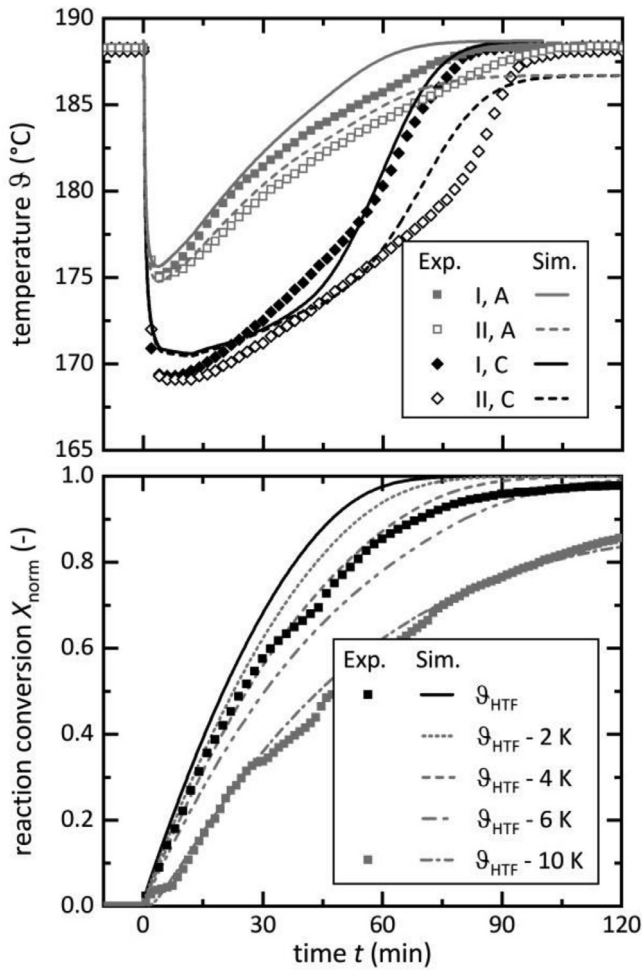


Fig. 8. Impact of axial HTF temperature gradients on the simulation results for the reference charging process. In the temperature progression displayed in the upper panel, the additional simulation results referring to cell II are obtained with a 2 K lower (but still constant) charging temperature compared to cell I (reference HTF temperature of 188.7°C). The lower panel shows the experimental and numerical results on the reaction conversion for an HTF temperature which is reduced by up to 10 K. Again, the simulation assumes a temporally and spatially constant HTF temperature.

tion parameters. In contrast, since the discharge process usually is conducted at higher pressures in order to achieve higher discharge temperatures compared to the charging process, mass transfer limitations are even more unlikely to occur here. Hence, an impact of the above-mentioned uncertainty on the simulation results can be excluded.

Indeed, we see a very close agreement of the simulation results with the experimental data of the reference discharging process (see Fig. 11, black dots), judged by the comparison of the thermal power transferred to the HTF (upper panel) and the reaction conversion (lower panel). Towards the end of the discharging process ($X > 80\%$), we see a slowdown in the experiment which we do not find in the simulation result. This might be explained by the first-order reaction rate model, which over-estimates the effective rate of the hydration reaction for large reaction conversions [15].

3.6.1. Storage operation with large inner heat transfer coefficients

As discussed in context of the charging process, we see axial temperature effects on the HTF side, and the same applies for the discharging process. In the following, another aspect related to the HTF side of the storage is discussed: the inner heat transfer coefficient, α_{HTF} , which defines the heat transfer from the steel

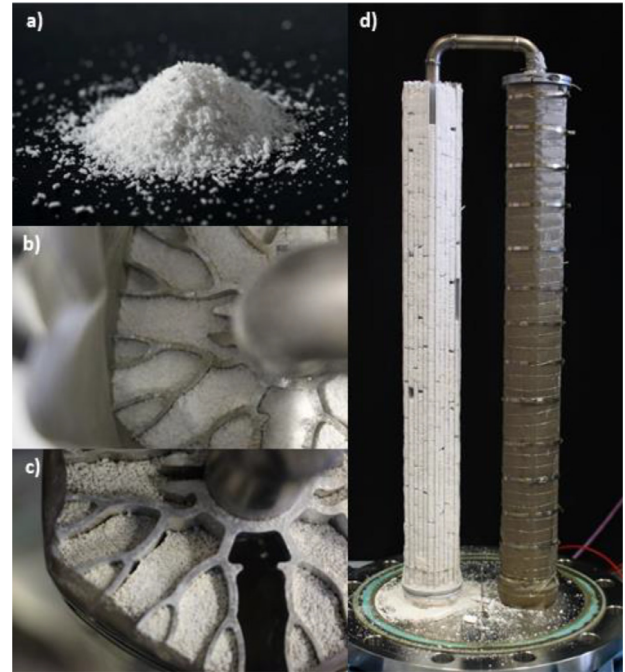


Fig. 9. Macroscopic effects in the reactive phase. In all photographs, the salt was in its monohydrate state. After the end of the experimental series, the reactive material had agglomerated in the segments of the heat transfer structure. Besides, small gaps had formed at the aluminum/porous medium interface. a) Loose granular monohydrate salt. b) Heat transfer structure filled with the reactive solid. c) View onto the storage cell after the end of the experimental series (34 charging/discharging cycles), with the filter mesh still attached. d) Dismantled storage module, with the metal filter mesh still attached onto the aluminum fins (storage cell I, right), and completely removed (storage cell II, left), respectively.

tube to the HTF. This research question is motivated by the boundary conditions given from applications with a phase-changing HTF, e.g. condensing steam/evaporating water, instead of a sensible HTF. Apart from smaller axial temperature gradients, phase-changing HTFs would allow for larger values of α_{HTF} . In the present experimental parametric study, the mass flow of the discharge process was varied in the range of 3.5 to 14.4 kg/min, with the steam pressure and HTF inlet temperature settings identical to the reference experiment. These mass flow rates correspond to heat transfer coefficients α_{HTF} in the range of 860 to 2840 W/(m²·K).

The same parameter variation was implemented in the numerical model (Fig. 11). Since the simulation results prove sufficient agreement with the corresponding experiments, both in terms of the thermal power (upper panel) and the reaction conversion (lower panel), we conducted another simulation study with an infinitely large HTF mass flow. Experimentally, such a scenario with a maximum potential performance of the storage design could be realized by e.g. evaporating water on the HTF side. For the given reference operation conditions, the storage's maximum thermal power could be increased by approximately 20%. This number indicates the potential of the storage design if it is operated without limitations on the HTF side, e.g. by replacing the sensible HTF by evaporating water. Notably, since the storage's performance is mainly dominated by heat transfer, it is independent of the choice of the reactive medium, provided that the reaction rates are at least as high as for the chosen reference system SrBr₂/H₂O.

4. Discussion

Based on the model validation discussed in the previous chapter, we have concluded that the thermal performance of the stor-

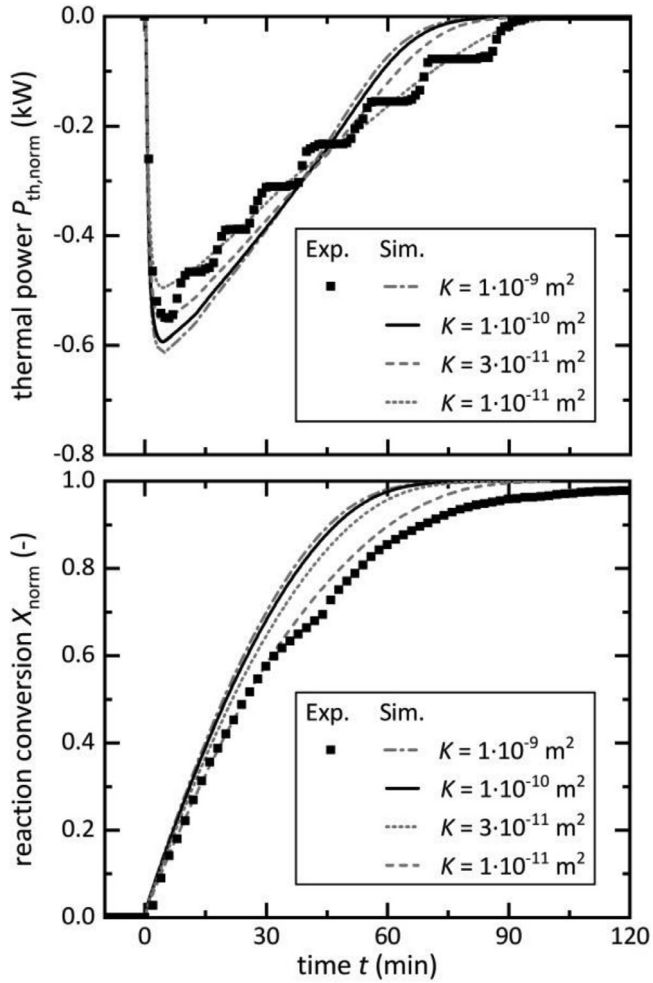


Fig. 10. Comparison of the simulation results with the experimental data from the reference charging process (188.7°C HTF temperature, 1.3 kPa average steam pressure, 16.5 kg/min HTF mass flow). The upper panel shows the experimental thermal power (markers) in comparison to the simulation results (line plots). The lower panel gives the reaction conversion of the dehydration reaction. Although it is not indicated by the local temperature propagation in the porous bulk, the integral performance of the storage is better reproduced with lower bulk permeabilities (e.g. $1 \cdot 10^{-11} \text{ m}^2$, compared to the reference value $1 \cdot 10^{-10} \text{ m}^2$).

age is dominated by heat transfer, which therefore is the first aspect to be addressed if the storage's performance shall be further optimized. Usually for gas-solid thermochemical reactions, the low conductivity of the solid is regarded as the "weak point" in the heat transfer coefficients. However, in order to gain a more detailed understanding to further improve the high-power storage design, it is of interest to also quantitatively distinguish between the different aspects contributing to the overall heat transfer limitation. When we neglect a thermal contact resistance between the aluminum fins and the stainless steel tube, there are four different contributors left to be considered: the thermal conductivities of the reactive bulk (λ_{bulk}) and the aluminum/steel heat exchanger (λ_{alu} , λ_{steel}) with their specific heat transport distances, and the heat transfer coefficients at the HTF/heat exchanger (α_{HTF}) and fin/bulk (k_{fin}) boundaries, with their specific heat transfer areas.

In the following, we approach this research question based on a thermal sensitivity study with the validated simulations. Finally, our work will be concluded by a discussion on the overall performance of the storage as a function of the internal temperature gradient, which serves as a hands-on estimation on the storage's

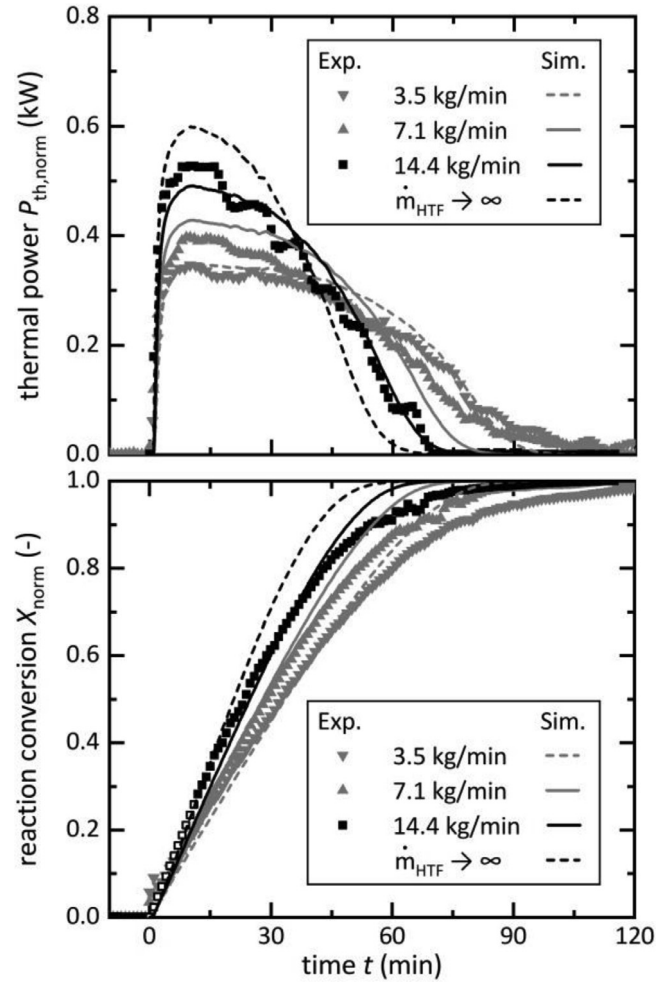


Fig. 11. Validation of the simulation results for the reference discharging process (black dots) and additional experiments conducted with smaller HTF mass flow rates. The upper panel shows the experimental thermal power (markers) in comparison to the simulation results (line plots). The lower panel gives the reaction conversion of the hydration reaction. The mass flow rates (3.5, 7.1 and 14.4 kg/min) correspond to heat transfer coefficients α_{HTF} of approximately 860, 1555, and 2840 $\text{W}/(\text{m}^2 \cdot \text{K})$. The experimental pressure curve from the reference experiment (14.4 kg/min) was implemented as boundary condition in all four simulation studies.

performance for any application-based boundary conditions on the charging/discharging temperatures and pressures.

4.1. Thermal sensitivity study

We have used the validated simulation tool to estimate the quantitative impact of the heat transfer-related parameters, such as thermal conductivities and heat transfer coefficients, via a sensitivity analysis. More precisely, each coefficient λ_j , α_j and k_j is separately varied by the factor $(1 + \gamma)$, with $\gamma \ll 1$. The relative influence of the parameter λ_j , α_j or k_j can be expressed by the corresponding sensitivity σ_j :

$$\sigma_j = \frac{P_{\text{th}}(k_j^*) - P_{\text{th}}(k_j)}{\gamma P_{\text{th}}(k_j)} \quad (19)$$

For steady-state heat transfer through parallel multi-layer walls or domains, these sensitivities σ_j would correspond to the share of a specific heat transfer coefficient in the total thermal resistance. However, in our case, the system features a transient and volumetric heat source/sink and a complex geometry. Consequently, the local temperature distribution at a layer boundary may vary. Still,

Table 2

To quantitatively assess the thermal sensitivities σ_j as given in Eq. (19), the simulated maximum thermal powers in the charging and discharging processes at the reference operating parameters are evaluated for the original and the varied sensitivity parameters k_j and k_j^* , respectively.

Sensitivity parameter	Charging σ_j	Discharging σ_j
$k_{fin}^* = (1 + \gamma) k_{fin}$	47%	51%
$\alpha_{HTF}^* = (1 + \gamma) \alpha_{HTF}$	20%	18%
$\lambda_{alu}^* = (1 + \gamma) \lambda_{alu}$ $\lambda_{steel}^* = (1 + \gamma) \lambda_{steel}$	15%	13%
$\lambda_{bulk}^* = (1 + \gamma) \lambda_{bulk}$	5%	3%
$k_{fin}^* = (1 + \gamma) k_{fin}$ $\alpha_{HTF}^* = (1 + \gamma) \alpha_{HTF}$ $\lambda_{alu}^* = (1 + \gamma) \lambda_{alu}$ $\lambda_{steel}^* = (1 + \gamma) \lambda_{steel}$ $\lambda_{bulk}^* = (1 + \gamma) \lambda_{bulk}$	86%	85%

the steady-state condition can be assumed as an approximation in the time regime where the thermal power is at its maximum (and hence, transients are minimal).

Eq. (19) is computed from the numerical model, but in our case its meaning is restricted to the sensitivity of the thermal power with respect to specific contributors. We chose the point in time with maximum thermal power transferred to or from the HTF in the reference charging and discharging processes also because the peak power is the most relevant storage characteristic for high-power applications. The results obtained for the reference operation parameters are given in Table 2. Please note that, from the application perspective, parameters such as λ_{alu} and λ_{steel} cannot be easily increased. In this case, the results should rather be interpreted as an inquiry if an optimization of the fin geometry (e.g. thicker fins) has any impact on the performance of the storage.

The results imply that the main contributor determining the maximum thermal power is the heat transfer coefficient k_{fin} at the bulk/heat exchanger boundary (sensitivity of 47–51%). The prior discussed heat transfer coefficient α_{HTF} from the HTF to the heat exchanger also leaves room for improvement (18–20%), same as the design of the aluminum fins (13–15%). In contrast, the effective bulk conductivity of the reactive phase has a neglectable impact on the storage's thermal performance (3–5%), at least during the charging/discharging phases close to the maximum thermal power. Actually, we find that the resulting sensitivities are almost constant within the time regime close to the maximum thermal power (time-resolved results not shown). Still, this conclusion cannot be transferred to all phases of the charging/discharging process, since e.g. in the early and late phases, sensible effects are pre-dominant.

From this analysis, it is concluded that the reactor geometry achieves its design targets: the impact of the (low) bulk thermal conductivity is reduced and the other contributors are balanced to a certain degree. Obviously, the wall heat transfer coefficient k_{fin} at the fin surface is the dominating effect regarding the maximum thermal power, which is not surprising, keeping in mind the discussion on the formation of gaps due to agglomeration and the reactive material's "breathing" behavior. In order to further improve the design, a geometry where this material behavior does not lead to the formation of gaps should be given high priority (e.g., by a design using wedged reactor chambers and an external force).

Interestingly, many numerical studies on closed thermochemical TES neglect an additional thermal resistance on the bulk/heat exchanger-boundary, assuming that the low bulk thermal conductivity is the dominating parameter. E.g., Fopah Lele et al. investigated the dehydration process of magnesium chloride hexahydrate in a closed lab-scale plate heat exchanger with only 6 mm reac-

tive bulk depth. When implementing a corresponding 3D numerical model, no additional heat transfer coefficient is considered at the bulk/heat exchanger boundary [24]. The sensitivity study performed in this work suggests that this is no valid assumption in the proposed high-performance reactor design. In contrast, in order to achieve a notably better overall thermal performance by increasing the bulk's effective thermal conductivity, λ_{bulk} would have to be increased by at least an order of magnitude.

An advantage of using the results of the simulation for assessing the thermal sensitivities is that this analysis implicitly includes the impact of the reaction rate and the steam mass transfer. E.g., pressure losses caused by mass transfer limitations result in locally varying reaction temperatures and, thus, varying temperature gradients. Similarly, the effective rate of reaction approaches a value of 0, if the thermochemical reaction system approaches thermodynamic equilibrium conditions, i.e. the solid's temperature equals the reaction temperature for the given steam pressure. Hence, a certain temperature gradient is needed to drive the chemical reaction. As can be seen from the last row in Table 2 (where all heat transfer-related coefficients are varied), heat transfer accounts for approximately 85% of the overall sensitivity with the remainder being related to contributions from the steam mass transfer and the rate of the chemical reaction.

4.2. Global performance: maximum thermal power

We have clearly seen in the previous section that heat transfer is the dominating effect for the reactor's overall performance. As a conclusion, the reactor performance can essentially be described in one single plot, where the operation parameters are expressed solely in the form of a single temperature difference. More specifically, every operating point of the storage is characterized by the difference of the HTF temperature (charging/discharging temperature) and the set steam pressure, which corresponds to a specific dehydration or hydration temperature, respectively:

$$\Delta T = T_{HTF} - T(p_{H2O}), \tag{20}$$

which turns positive in the case of charging, and negative in the case of discharging.

This temperature gradient is the maximum ΔT available to drive the chemical reaction and for the transfer of thermal energy. Other authors also refer to ΔT with the term "equilibrium temperature drop", e.g. Stitou et al. [7]. From the prior discussion on the thermal sensitivities, we learned that the parameters related to heat transfer account for approximately 85% of the overall sensitivity of the maximum thermal power. Consequently, as heat transfer is the dominating power limitation, the operation characteristics of the present storage module can be summarized in a master plot, with the maximum thermal power P_{th} plotted versus the maximum temperature difference ΔT allowed by the operating parameters (ϑ_{HTF} , p_{H2O}). The corresponding graph is depicted in Fig. 12. Here, the power is scaled to 1 m heat exchanger length. In contrast to the power progression discussed above ($P_{th,norm}$), the experimental data points in Fig. 12 are not normalized, and hence include thermal losses. Since the reference discharging experiment discussed in this work (Fig. 2b) was conducted at a lower mass flow compared to the others (14 kg/min versus approximately 16 kg/min), we included a similar experiment with a flow rate of 16.4 kg/min instead for better comparability. In addition to the reference charging and discharging experiments chosen for the model validation (Fig. 2), the plot contains data from storage operation points discussed in our prior work [16]. Furthermore, we have included the results of the corresponding simulation studies, both for the lab-scale setup, and for storage operation at very large HTF mass flows.

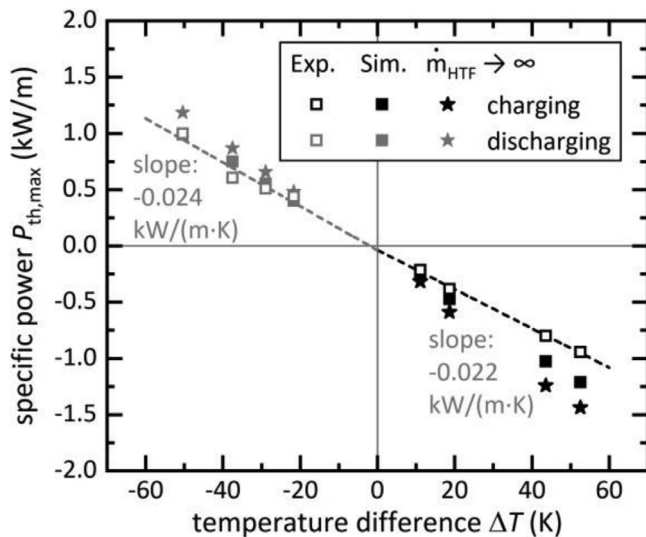


Fig. 12. Maximum specific thermal power provided by the 1 kW prototype (kW per meter finned tube heat exchanger). ΔT is the difference between the pressure-dependent reaction temperature, which is calculated from Eq. (3) and Eq. (5), and the set charge/discharge temperature. The data points are evaluated from the reference experiments discussed here and in our prior work [16].

As expected from the thermal sensitivity studies and the discussion on the power-dominating processes, the experimental data points scale linearly with ΔT . This is especially remarkable since the graph contains data obtained at a wide range of steam pressures and HTF temperatures (charging: 1–10 kPa and 180–250°C; discharging: 70–560 kPa and 210–280°C). Generally, we find larger over-estimation of the experimental peak power by the numerical model in case of the charging process than for discharging. Please note that in particular for the hydration reaction, the empirical rate models were determined for maximum steam pressures of approx. 70 kPa. But still, the model predicts the storage's discharging performance in very close reproduction even for higher pressures, e.g. $p_{\text{HTF}} = 208^\circ\text{C}$, $p_{\text{H}_2\text{O}} = 147 \text{ kPa}$ ($\Delta T = -50 \text{ K}$).

Apparently, the linear regressions given for the experimental data result in a similar slope for charging and discharging. In contrast, for the same absolute values of ΔT , the simulation data obtained for $m_{\text{HTF}} \rightarrow \infty$ indicates higher peak powers for the charging process than for discharging. This could be explained with the overall higher dehydration reaction rates, since even if the storage's performance is mainly determined by the heat transfer, the impact of the reaction kinetics is not reduced to zero.

The resulting $P_{\text{th}}(\Delta T)$ -regressions are useful for the investigation of various storage applications in several ways. For instance, to estimate suitable operating points, e.g. the needed condenser temperature for a given storage charging temperature and power. Apart from that, since we could prove that the storage's performance is scalable by verifying its heat transfer-dominated properties, the diagram can also be used as a design tool to define the needed storage size, e.g. for a given maximum condenser temperature and a minimum discharge temperature. Moreover, since the data points correspond to the storage's effective temperature gradients needed for charging and discharging, the correlations allow to calculate the exergy efficiency of the storage process, both for an ideal storage operation (simulation data for $m_{\text{HTF}} \rightarrow \infty$) or in a realistic scenario (experimental data with thermal losses).

Lastly, the main conclusions of the analysis as well as the developed tools are transferable to other thermochemical gas-solid reaction systems which target high-power applications. Since the storage's overall performance is mainly determined by heat transfer,

it will remain unchanged if the storage is operated with another salt-steam reaction, given that the thermochemical working pair allows for reaction rates at least as large as with the reference system $\text{SrBr}_2/\text{H}_2\text{O}$. Again, strictly stated, this estimation is only valid for the period of time in which the process is actually dominated by the effective heat transport. While this will be the case during the most interesting reaction phases from an application perspective, the behavior may deviate especially in the late reaction phases.

5. Summary

In the present work, we show that the operation of a thermochemical energy storage and heat transformer based on the hydration reaction of strontium bromide and the dehydration of its monohydrate can be modelled with a small number of fitting parameters. As one might expect, the overall thermal performance of the storage is dominated by heat transfer, and not by steam mass transfer or the reaction kinetics. From a thermal sensitivity study based on the numerical model, we conclude that the boundary between the aluminum fins and the reactive bulk is the most important limitation to the storage's maximum thermal power. This means that, all in all, the finned heat exchanger effectively mitigates the low thermal conductivity of the porous medium, and thus, a further increased bulk thermal conductivity would have a low impact on the overall performance of the TES. Based on the thermal sensitivity studies, we prove that the maximum thermal power of the storage correlates linearly with the internal temperature gradient of the storage, ΔT , which is defined as the difference between the charging/discharging temperature and the reaction temperature for the given steam pressure. The largest influence on the maximum thermal power is attributed to the heat transfer at the bulk/heat exchanger boundary. This is an important finding since the bulk/wall heat transfer coefficient is usually neglected when analyzing the storage performance, assuming that it is larger by orders of magnitude compared to the bulk thermal conductivity. However, we showed that this is not the case for reactor designs tuned up towards high specific thermal powers by means of large specific heat transfer surfaces (m^2 per kg storage material). These main conclusions as well as the developed performance characterization tools are transferable to other thermochemical gas-solid reaction systems which target high-power applications.

With regard to a scale-up of the proposed TES design for larger industrial applications, we discuss the impact of axial temperature gradients occurring in the heat transfer fluid. This is of particular interest for the design of scaled-up storage modules operated with sensible heat transfer fluids, e.g. thermal oil, where large HTF temperature gradients are expected.

In future work, the validated simulation tool could be used to further optimize the aluminum fin structure to meet the requirements of a specific industrial application, e.g. to determine the trade-off between high specific storage capacities and the specific thermal power, with "specific" referring to a radial cross-section of the heat exchanger. Another model application area could be the investigation of the impact of known degradation effects for large number of charging/discharging cycles, e.g. lower effective rates of reaction due to agglomeration. Moreover, the investigation of operation strategies, e.g. controlling the power output by constantly adjusting the steam pressure during the charging/discharging process, could be of high interest.

Most importantly, we see high potential in applying the discussed performance characterization, namely the correlation between the temperature gradient needed for charging and discharging the TES and the resulting maximum thermal power, for the identification of suitable industrial applications in detailed use-

case feasibility studies and, in particular, the implementation of an energy efficiency analysis of the storage process.

Declaration of Competing Interest

The authors declare that they have no known competing financial interests or personal relationships that could have appeared to influence the work reported in this paper.

CRedit authorship contribution statement

Jana Stengler: Writing - original draft, Visualization, Validation, Methodology, Investigation, Data curation, Conceptualization. **Inga Bürger:** Methodology, Writing - review & editing. **Marc Linder:** Supervision, Funding acquisition, Writing - review & editing.

Acknowledgements

The work described in this paper has received financial support from the “Bundesministerium für Wirtschaft und Energie” (BMWi, Federal Ministry for Economic Affairs and Energy) in Germany as part of the “TheSan” project (03ET1297A). We gratefully acknowledge the support of Christian Brack, Torsten Ascher, Marius Drexler, Eva Fischer, and Moritz Wild during the conception, installation, and the commissioning of the test setup. Also, we thank Dr. Bernd Hachmann from F. W. Broekelmann Aluminumwerk GmbH for providing the aluminum fins.

Appendix

Determination of the wall heat transfer coefficient k_{fin}

The wall heat transfer coefficient was obtained from separate simulation studies on the charging and discharging process. Since at the sensor position A, which is located right at the heat exchanger surface, the reaction progression is mainly determined by the local heat transfer coefficient, this data was chosen as reference for the determination of k_{fin} . The results of a sensitivity study are depicted in Fig. A1. Since the variation of k_{fin} resulted in different values for the charging (upper panel) and discharging processes (lower panel), a linear correlation between the two values was assumed, depending on the level of hydration h .

Modification of the hydration reaction rate model

If the empirical rate model given in Eq. (4) is evaluated, e.g. for a steam pressure of 69 kPa and different temperatures, it is observed that the effective rate coefficients k_{eff} reaches values below 0.005 1/s for temperatures less than 30 K from the hydration reaction temperature at 69 kPa (230°C, calculated from Eq. (5)), see Fig. A2.

The temperature difference in this graph is defined as $\Delta T = T - T_{hyd}(p_{hyd})$, and results in negative values for the hydration reaction (the hydration reaction only starts when the solid's temperature T is below the reaction temperature expected for the given steam pressure, $T_{hyd}(p_{hyd})$). The plot additionally contains the effective rate coefficients from thermogravimetric analysis (TGA) measurements, which were used for the parametrization of the empirical rate model as described in our previous work [15]. However, the experiments performed with the lab-scale storage module indicate that the TGA results cannot be transferred to the larger scaled experiment: if the empirical rate correlation is used in the numerical model, bulk temperatures do not reach the expected plateau as they do in the experiment, see the simulation results plotted in Fig. A3. In other words: the empirical rate model derived from the

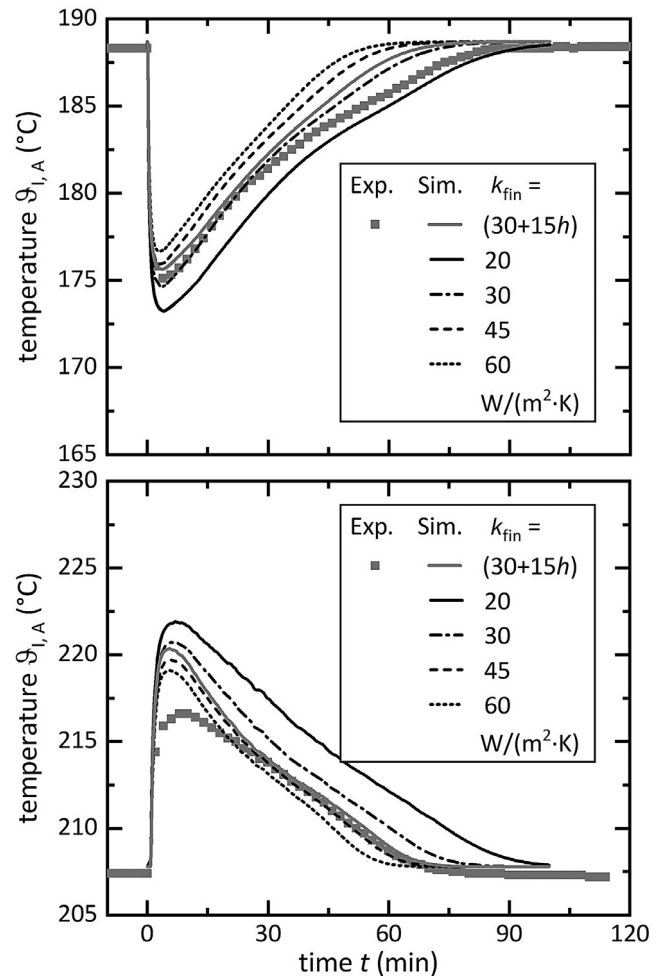


Fig. A1. Sensitivity study on the impact of k_{fin} on the progression of the charging process (upper panel) and the discharging process (lower panel). The plots contain data from different simulation studies, with constant values k_{fin} in the range of 20–60 $W/(m^2 \cdot K)$, as well the correlation finally chosen as the best fit, $k_{fin} = (30+15h) W/(m^2 \cdot K)$.

TGA measurements results in too small reaction rates, when compared to the experimental results from the lab-scale setup. At the same time, the empirical pressure-temperature correlation for the hydration reaction, which is given in Eq. (5), is confirmed by an experiment conducted with stopped HTF mass flow, see Fig. A4. This correlation is therefore excluded as a possible reason for deviations between the simulation and the experiments.

A potential (and likely) error source is the pressure determination when the model was developed from TGA data [15]. The lab-scale experiments discussed in the present work were conducted under a pure steam atmosphere, whereas the TGA measurements were performed under a mixed steam and nitrogen atmosphere. The commercial TGA setup features a sample chamber design where two separate gas flows (steam/nitrogen mixture as sample gas with a constant total volume flow of 100 ml/min, and pure nitrogen as protective gas with a constant volume flow of 50 ml/min to prevent condensation in the mass balance) were supposed to not intersperse, so that the impact of the protective gas flow was assumed negligible in the original pressure calculation. If, for experimental reasons, the gas flows did mix, a lower effective steam partial pressure results than originally calculated from the set operation parameters.

If the worst-case scenario of a completely mixed gas atmosphere is assumed and the given water vapor partial pressures are

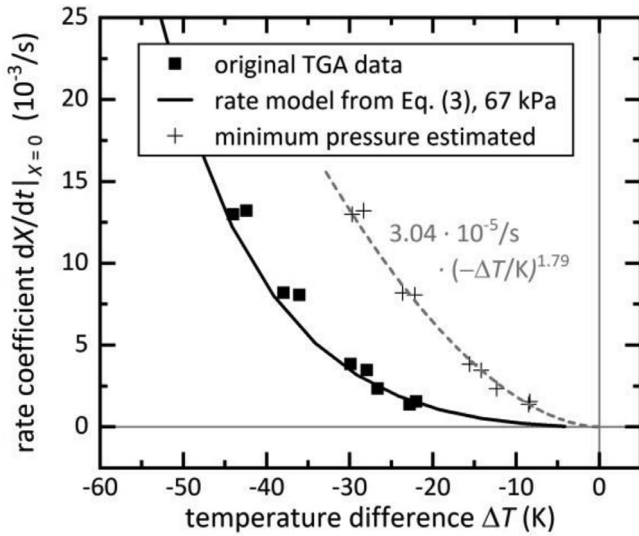


Fig. A2. Analysis of the effective rate coefficients of the hydration reaction, which were obtained from isothermal and isobaric thermogravimetric analysis (TGA) measurements [15]. The temperature difference ΔT is the gradient between the pressure-dependent reaction temperature, which is calculated from Eq. (5), and the set sample temperature. If a maximum error is assumed in the water vapor partial pressure settings, the TGA data points are moved towards smaller absolute ΔT values.

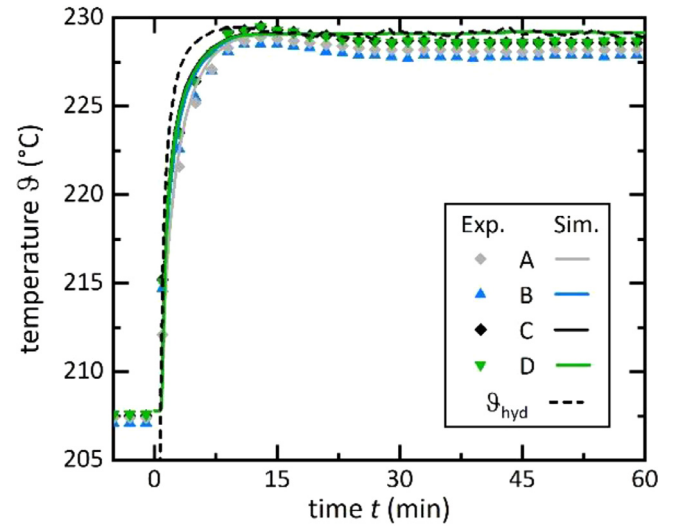


Fig. A4. Validation of the pressure-temperature correlation for the hydration reaction. When the HTF flow is stopped just before the steam valve is opened and the pressure increases, the temperatures reach the expected temperature plateau. This is correctly reproduced by the simulation, thus confirming the empirical pressure-temperature correlation of the hydration reaction, which is given in Eq. (5). The simulation results were obtained from the modified hydration reaction rate model.

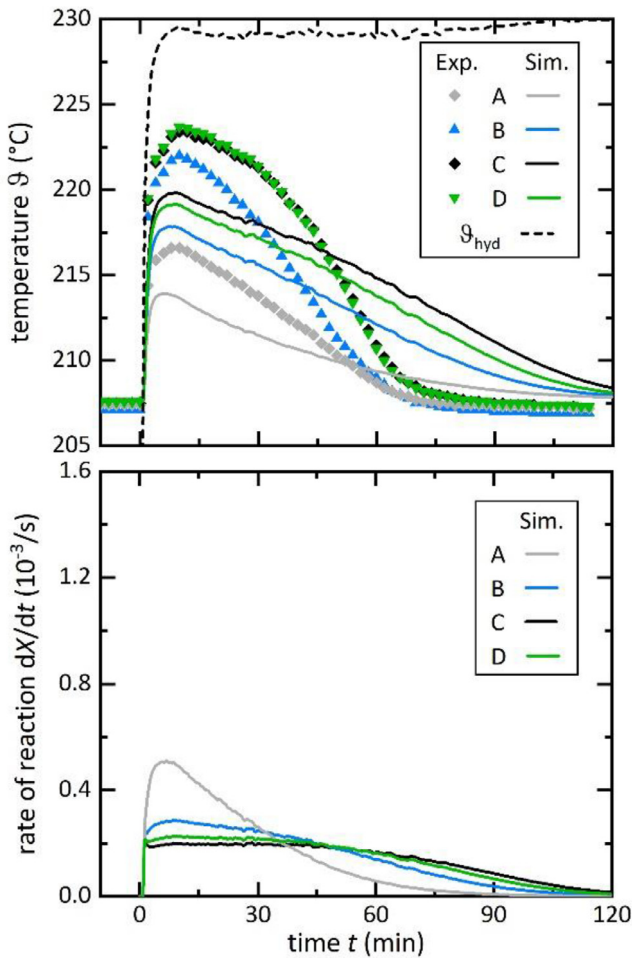


Fig. A3. Simulation results of the reference discharging process with the hydration reaction rate being implemented based on the unmodified empirical model from Eq. (4). Judged from the temperature progressions at the different bulk positions (upper panel), the unmodified model leads to too low effective reaction rates.

re-calculated with the resulting scaling factor $100/(100+50)$, the resulting rate coefficient data points are shifted towards smaller steam pressures or smaller absolute temperature differences, see Fig. A2. This way, the empirical rate model is shifted towards higher reaction rates when the thermochemical system approaches the expected reaction temperature. To obtain a simple empirical model representing these data points, we chose a power-law fit of the data points with the “minimum pressure estimation” as a function of the absolute value of the temperature difference, see Eq. (6). From the simulation results on the discharging process obtained with the modified rate model (Fig. 6), we conclude that the worst-case scenario leads to a slight over-estimation of the hydration reaction, indicated by the bulk temperatures higher than expected from the experiment.

Influence of the bed permeability on the temperature progression during charging

Under vacuum conditions, e.g. 1–10 kPa abs. during charging the storage, a change in the bulk permeability strongly affects the steam mass transfer within the porous medium. The temperature progression in the reactive bulk was numerically studied with the permeability ranging from $1 \cdot 10^{-9} \text{ m}^2$ (Fig. A5) to $1 \cdot 10^{-11} \text{ m}^2$ (Fig. A6), in addition to the reference value $1 \cdot 10^{-10} \text{ m}^2$ (Fig. 4). Judged by the temperature progression observed in the experiment, no pressure drop occurs between the temperature probe positions: a pressure gradient in the fixed bed would cause a temperature difference between the minimum temperatures at the positions B, C, D, and the expected dehydration reaction temperature as indicated in the simulation results in Fig. A6. E.g. in the reference study (Fig. 4), the simulated temperature at position C slightly deviates from the expected reaction temperature, which is not the case in the experiment. This could be explained e.g. by a higher local steam pressure occurring due to mass transfer limitations in the simulation. For example, if the permeability was increased from $1 \cdot 10^{-10} \text{ m}^2$ to $1 \cdot 10^{-9} \text{ m}^2$, the plateau temperatures of the positions B, C and D would coincide with ϑ_{dehyd} (Fig. A5). Hence, concluded from the comparison of the simulation results with the experimental temperature curves, the effect of steam mass transfer within the bulk phase is not dominating the system performance.

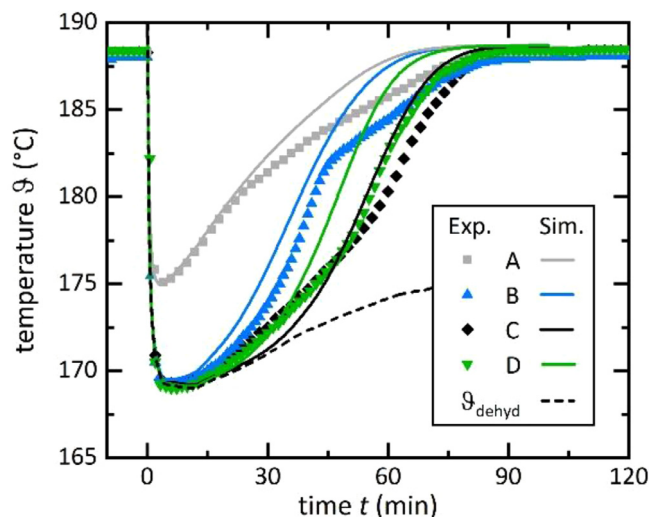


Fig. A5. Results of the reference charging process (188.7°C HTF temperature, 1.3 kPa average steam pressure, 16.5 kg/min HTF mass flow). In the numerical study, the bed permeability was increased to a value of $1 \cdot 10^{-9} \text{ m}^2$, leading to no effective pressure drop within the bulk phase even at the very low absolute pressure level. This is judged by the temperature minimum in the bulk positions B, C, and D, which correspond to the dehydration reaction temperature for the given steam pressure, and are in close agreement with the experimental data.

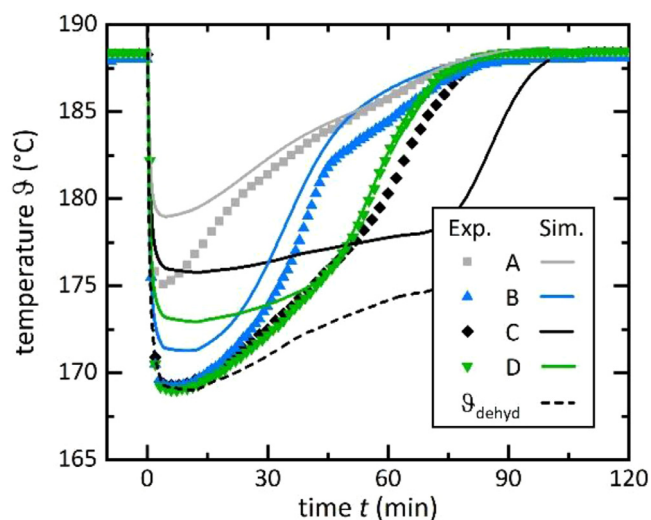


Fig. A6. Results of the reference charging process (188.7°C HTF temperature, 1.3 kPa average steam pressure, 16.5 kg/min HTF mass flow). Here, the bed permeability was set to a value of $1 \cdot 10^{-11} \text{ m}^2$ in the numerical study. Obviously, the lower permeability causes a pressure drop within the bulk phase, which leads to locally differing minimum temperatures in the simulation.

Supplementary materials

Supplementary material associated with this article can be found, in the online version, at doi:10.1016/j.ijheatmasstransfer.2020.120797.

References

- [1] D. Aydin, S.P. Casey, S. Riffat, The latest advancements on thermochemical heat storage systems, *Renewable & Sustainable Energy Reviews* 41 (2015) 356–367.
- [2] J. Sunku Prasad, P. Muthukumar, F. Desai, D.N. Basu, M.M. Rahman, A critical review of high-temperature reversible thermochemical energy storage systems, *Applied Energy* 254 (2019).
- [3] F.S. Yang, G.X. Wang, Z.X. Zhang, V. Rudolph, Investigation on the influences of heat transfer enhancement measures in a thermally driven metal hydride heat pump, *International Journal of Hydrogen Energy* 35 (18) (2010) 9725–9735.
- [4] T. Nagel, S. Beckert, C. Lehmann, R. Gläser, O. Kolditz, Multi-physical continuum models of thermochemical heat storage and transformation in porous media and powder beds—A review, *Applied Energy* 178 (2016) 323–345.
- [5] M. Gaeini, R. Wind, P.A.J. Donkers, H.A. Zondag, C.C.M. Rindt, Development of a validated 2D model for flow, moisture and heat transport in a packed bed reactor using MRI experiment and a lab-scale reactor setup, *International Journal of Heat and Mass Transfer* 113 (2017) 1116–1129.
- [6] M. Schaefer, A. Thess, Simulation of a closed low-pressure honeycomb adsorber for thermal energy storage, *International Journal of Heat and Mass Transfer* 126 (2018) 796–807.
- [7] D. Stitou, G. Crozat, Dimensioning nomograms for the design of fixed-bed solid-gas thermochemical reactors with various geometrical configurations, *Chemical Engineering and Processing: Process Intensification* 36 (1997) 45–58.
- [8] M. Mbaye, Z. Aidoun, V. Valkov, A. Legault, Analysis of chemical heat pumps (CHPs): Basic concepts and numerical model description, *Applied Thermal Engineering* 18 (1998) 131–146.
- [9] J. Castaing-Lasvignottes, P. Neveu, Development of a numerical sizing tool applied to a solid-gas thermochemical transformer—II. Influence of external couplings on the dynamic behaviour of a solid-gas thermochemical transformer, *Applied Thermal Engineering* 17 (1997) 519–536.
- [10] H. Lahmidi, S. Mauran, V. Goetz, Definition, test and simulation of a thermochemical storage process adapted to solar thermal systems, *Solar Energy* 80 (2006) 883–893.
- [11] M. Pons, P. Dantzer, J.J. Guilleminot, A measurement technique and a new model for the wall heat transfer coefficient of a packed bed of (reactive) powder without gas flow, *International Journal of Heat and Mass Transfer* 36 (10) (1993) 2635–2646.
- [12] H.-B. Lu, N. Mazet, B. Spinner, Modelling of gas-solid reaction—Coupling of heat and mass transfer with chemical reaction, *Chemical Engineering Science* 51 (1996) 3829–3845.
- [13] H. Huang, Modeling of gas–solid chemisorption in chemical heat pumps, *Separation and Purification Technology* 34 (1–3) (2004) 191–200.
- [14] K. Risthaus, I. Bürger, M. Linder, M. Schmidt, Numerical analysis of the hydration of calcium oxide in a fixed bed reactor based on lab-scale experiments, *Applied Energy* 261 (2020).
- [15] J. Stengler, I. Bürger, M. Linder, Thermodynamic and kinetic investigations of the SrBr₂ hydration and dehydration reactions for thermochemical heat transformation, *Applied Energy* 277 (2020) 115432.
- [16] J. Stengler, M. Linder, Thermal energy storage combined with a temperature boost: An underestimated feature of thermochemical systems, *Applied Energy* 262 (2020) 114530.
- [17] M. Johnson, J. Vogel, M. Hempel, B. Hachmann, A. Dengel, Design of high temperature thermal energy storage for high power levels, *Sustainable Cities and Society* 35 (2017) 758–763.
- [18] J. Stengler, J. Weiss, M. Linder, Analysis of a Lab-Scale Heat Transformation Demonstrator Based on a Gas–Solid Reaction, *Energies* 12 (12) (2019) 2234.
- [19] B. Michel, P. Neveu, N. Mazet, Comparison of closed and open thermochemical processes, for long-term thermal energy storage applications, *Energy* 72 (2014) 702–716.
- [20] H.D. Baehr, K. Stephan, *Wärme- und Stoffübertragung*, Springer, 2019.
- [21] A. Fopah Lele, K.E. N'Tsoukpoe, T. Osterland, F. Kuznik, W.K.L. Ruck, Thermal conductivity measurement of thermochemical storage materials, *Applied Thermal Engineering* 89 (2015) 916–926.
- [22] VDI-Wärmeatlas, (2013).
- [23] N. Mazet, M. Amouroux, Analysis of heat transfer in non-isothermal solid-gas reacting medium, *Chemical Engineering Communications* 99 (1991) 175–200.
- [24] A. Fopah Lele, F. Kuznik, H.U. Rammelberg, T. Schmidt, W.K.L. Ruck, Thermal decomposition kinetic of salt hydrates for heat storage systems, *Applied Energy* 154 (2015) 447–458.
- [25] D.L. Perry, *Handbook of Inorganic Compounds*, (2011).
- [26] D.D. Wagman, W.H. Evans, V.B. Parker, R.H. Schumm, I. Halow, S.M. Bailey, K.L. Churney, R.L. Nuttal, The NBS Tables of Chemical Thermodynamic Properties. Selected Values for Inorganic and C1 and C2 Organic Substances in SI Units, *Journal of Physical and Chemical Reference Data* 11 (1982).

3

Chapter 3

Discussion and Conclusions

The present work investigates a thermochemical energy storage and heat transformer for industrial waste heat recovery. It covers the development of a 1 kW prototype starting from the characterization of a suitable reactive material towards the experimental proof-of-concept and a numerical analysis of the performance-dominating process mechanisms.

In the following, the two leading research objectives described in Chapter 1.2 are discussed based on the publications from Chapter 2, starting with the conclusions on the suitability of strontium bromide for thermochemical heat transformation. Afterwards, the results on the operation characteristics of the storage prototype will be summarized and the limitations and optimization potential will be deduced from the results of the numerical simulation. The thesis is concluded by a discussion of three exemplary application scenarios, which are derived from the operation range of the developed storage technology.

3.1 Discussion

In a prior study based on thermogravimetric analysis measurements, it was experimentally determined that the anhydrous strontium bromide salt reacts with water vapor in a reversible chemical reaction in a temperature range relevant for

3 Discussion and Conclusions

industrial processes ($> 150\text{ }^{\circ}\text{C}$) [42]. From this starting point, in the present thesis, a detailed study on the reaction temperatures and pressures was conducted with the goal of identifying technically relevant charging and discharging temperatures. Technical relevance in this context means that the thermochemical system needs to provide sufficient rates of reaction to enable charging and discharging the storage at high power levels. This is motivated by the focus on industrial applications with large numbers of charging/discharging cycles, possibly also in continuous operation for continuous thermal upgrade of the stored energy.

In lab-scale experiments with approximately 1 kg of the reactive material, it was found that a thermal hysteresis appears between the dehydration and the hydration reaction of about 14 K at a mean steam pressure of 17 kPa. From these results, steam pressure-dependent correlations for the reaction temperatures were deduced. The thermal hysteresis is the reason why the term “equilibrium temperature” is avoided in this context: for the same steam pressure value, the technically relevant reaction temperatures of the hydration and dehydration reaction deviate. It is expected that the two pressure-temperature correlations merge into a single one at higher dehydration pressures (above approximately 50 kPa), as observed e.g. for the calcium oxide/calcium hydroxide thermochemical system [69]. However, such experiments could not be conducted within the present work. Interestingly, when experiments on the thermodynamics of the (chemically) reversible reaction were performed in the TGA setup, a kinetic limitation was observed. This applies to both reaction directions; however, the hydration is more affected than the dehydration. Based on the pressure-temperature correlations, empirical models on the reaction rates were determined for a limited operation range. It was found that the effective reaction rate can basically be described as a function of the temperature difference between the pressure-dependent reaction temperature and the sample temperature.

Apart from that, a study on the cycling stability of the chemical reactions was performed with 100 hydration/dehydration cycles in a TGA setup. It was observed that the hydration reaction is cycle stable, whereas the rate of the dehydration reaction slows down for higher reaction conversions (approximately $> 80\%$) under

3.1 Discussion

the given experimental conditions (170 °C, pure nitrogen atmosphere). However, the dehydration is fully reversible in terms of the overall reaction conversion.

For the experimental proof-of-concept, a storage design was developed which is dedicated to achieve high specific thermal powers, but still provides scalability for large storage applications. The storage consists of a finned-tube heat exchanger, with steam as reacting gas on the shell side, and the heat transfer fluid on the tube side. The tube is equipped with axial aluminum fins to allow for an increased effective thermal conductivity in the bulk phase. The used aluminum fins were originally designed for a latent TES operated with sodium nitrate [70], [71]. Within the present work, the storage design was adapted to meet the requirements of a thermochemical TES.

With the 1 kW prototype, the experimental proof-of-concept for thermochemical energy storage and heat transformation based on $\text{SrBr}_2/\text{H}_2\text{O}$ was successfully demonstrated for the first time. The minimum demonstrated charging temperature is 179 °C, with the steam pressure set to 1 kPa. The maximum discharging temperature is 281 °C. Here, the steam pressure was set to 560 kPa, which results in hydrations reaction temperatures above 300 °C. Since a pressure of 560 kPa corresponds to the maximum pressure allowed in the laboratory system, it can be expected that, if required, the discharge temperatures can be further raised by increasing the steam pressure. In the case of the charging reaction, the application-relevant lower limit of the operation temperature range is reached in the experiments: lower charging temperatures are possible by further lowering the condenser temperature, but this requires additional cooling effort below ambient temperature. At the same time, the reaction rate of the dehydration reaction does not allow for high specific thermal powers at low temperatures (approximately < 180 °C).

Apart from the identification of the maximum operation temperature range, parametric studies on the thermal power of the storage module were conducted. The peak power obtained during charging and discharging was approximately 1.2 kW, which corresponds to a specific thermal power of 250 W per kg of the anhydrous salt, or 960 W per meter finned tube.

3 Discussion and Conclusions

After the completion of the experimental series, which included 34 charging/discharging runs in total, the storage vessel was opened. The reactive bulk phase was observed to have agglomerated into a larger, porous structure, with fractures separating it into smaller pieces. At distinct points, gaps had emerged between the aluminum surface and the reactive phase. However, all in all, the reactor design was found suitable for a reliable storage operation and for up-scaling for larger thermal powers and capacities.

In a last step, the processes dominating the storage's thermal performance were analyzed in a numerical study. This way, the FEM-based transient 2D model links the results of the material characterization, i.e. the TGA experiments and the 1 kg measurements, with the proof-of-concept study. Data on the bulk's thermal conductivity, heat capacity and permeability were obtained from the literature, thus, for the parametrization of the model, one single parameter remained undefined: the heat transfer coefficient at the bulk/heat exchanger boundary, α_{fin} . Hence, this parameter was determined from a calibration of the numerical model with the experimental data obtained from the 1 kW prototype. It was found that a hydrate level-dependent correlation of α_{fin} allows for a close reproduction of the experimental data. With the fully parametrized and experimentally validated model, a sensitivity study on the single contributors to the overall heat transfer coefficient of the storage cell was performed.

These data were used to perform a thermal sensitivity analysis, since the geometry of the storage cell is too complex in order to be satisfyingly described in an analytical way. As basis for the comparison, the peak power of the storage module obtained in a reference charging and discharging experiment was chosen. From the sensitivity study, it is concluded that the thermal power is indeed largely dominated by heat transfer. In addition, the single contributors were quantified: about 50% of the overall thermal sensitivity of the storage cell relates to the bulk/heat exchanger boundary, whereas the low thermal conductivity of the bulk phase has a very low impact on the peak power (approximately 5% of the overall thermal sensitivity). This is a valuable conclusion since in many numerical studies on the performance of thermochemical TES systems, the

3.2 Application scenarios

thermal resistance at the heat exchanger wall is neglected. This may be justified for storage geometries designed for large specific capacities rather than for high specific powers and/or loose granules or powders. However, this is not the case for the presented high-power storage design, where on the one hand, the impact of the low bulk thermal conductivity is effectively mitigated, and on the other hand, the bulk phase agglomerates.

The proven heat transfer limitation implies that the peak power of the storage module scales (almost) linearly with the storage's internal temperature gradient ΔT . The internal gradient is defined as the difference between the charging (discharging) temperature and the dehydration (hydration) temperature, each corresponding to the given steam pressures. Hence, for any given storage operation point (temperature and pressure), the performance of the proposed storage design can be predicted based on this parameter. Moreover, this conclusion is transferable to other steam-based reaction systems, given that the effective reaction rates are at least as high as in the case of $\text{SrBr}_2/\text{H}_2\text{O}$.

Based on the investigated prototype and the derived performance characteristics of the combined TES and heat transformer design, one can imagine a variety of potential application scenarios. Three general concepts of the integration of this technology into industrial applications will be briefly introduced in the following, thus highlighting starting points for further research.

3.2 Application scenarios

Generally, in terms of the exergy efficiency, industrial processes with a demand for process heat benefit from replacing the usage of electricity as a "high value energy currency" by "lower value energy currencies" such as steam produced from solar thermal energy [72]. The objective of this outlook is to outline first concepts of how the technology of combined TES and heat transformation could improve the exergy efficiency in the industrial sector using the example of three basic application scenarios.

3.2.1 TES without effective temperature gradient

In this first case, waste heat from an industrial process shall be stored without an effective temperature gradient between charging and discharging. An use case could be batch-processes in chemical process industries, with the storage being charged at the end of one batch, and discharged at the beginning of the subsequent batch (Fig. 3.1). Hereby, the discharge process could be driven by low-temperature waste heat or solar thermal energy to supply steam as reactive gas. In the depicted scenario, the reaction gas pressure difference between charging and discharging needs to only compensate for the temperature gradients for heat transfer. Since the thermal power of the developed storage module depends on the internal temperature gradient, the effective charging and discharging powers can be controlled by adjusting the steam pressure during charging and discharging, respectively. The investigation of such process control strategies could be achieved via the validated simulation tool developed in this thesis.

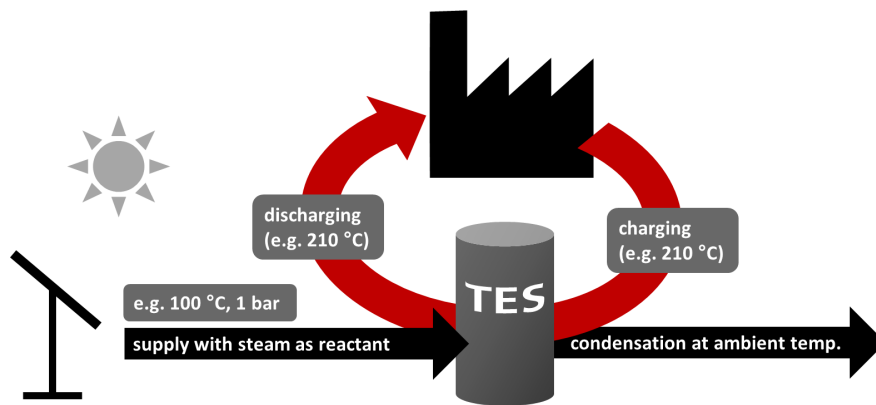


Figure 3.1: Application scenario of TES with no effective temperature difference between the charging and the discharging temperatures. The given temperatures are exemplarily chosen. Concerning the application-side, heat transfer fluid with a phase-change, e.g. condensing steam but also sensible heat transfer fluids are suitable to charge and discharge the storage.

Obviously, the Carnot efficiency of this isothermal TES is 1. However, from the operation characteristics of the 1 kW prototype, it is known that a temperature gradient of approximately 20 K needs to be taken into account for charging and discharging the storage with technically relevant thermal powers. Hence, the HT-process in this exemplary application effectively corresponds to a thermal upgrade from 190 °C (charging) to 230 °C (discharging). If thermal losses to the ambient are neglected, this results in an effective energy efficiency of 0.76 (Eq. (1.2), $T_0 = 298$ K, $T_C = 373$ K, $T_M = 463$ K, $T_H = 503$ K).

Alternatively, the system can be characterized by the exergy efficiency based on the reaction and evaporation enthalpies, which is 0.73 with the given values (Eq. (1.3), $T_0 = 298$ K, $T_C = 373$ K, $T_M = 483$ K, $T_H = 483$ K). For simplification, temperature-independent enthalpy values are assumed ($\Delta_R H = 72$ kJ/mol, $\Delta_E H = 44$ kJ/mol). Apart from the evaporation enthalpy, this estimation includes the energy needed to heat the water from T_0 to T_C (heat capacity: 4.2 kJ/(kg·K)).

3.2.2 TES combined with a thermal upgrade

After having discussed the basic storage scenario, it is clear that the stored thermal energy can also be upgraded to even higher output temperatures, depending on the temperature available for steam supply as gaseous reactant. Continuous operation could be achieved by the implementation of two separate storage units, which are separately charged and discharged. As depicted in the example in Fig. 3.2, such a heat transformer could also be integrated between two different processes – one emitting waste heat (“I”), and the other one demanding process heat at a higher temperature level. By adjusting the steam pressure during discharging, the required process-heat temperature profile of the other process (“II”) can be perfectly addressed.

For the given temperatures, the (ideal) Carnot energy efficiency is 0.77 (Eq. (1.2), $T_0 = 298$ K, $T_C = 393$ K, $T_M = 463$ K, $T_H = 513$ K). By analogy with the previous section, the effective Carnot efficiency is 0.65 when considering an internal gradient of 20 K for charging and discharging (Eq. (1.2), $T_0 = 298$ K, $T_C = 393$ K,

3 Discussion and Conclusions

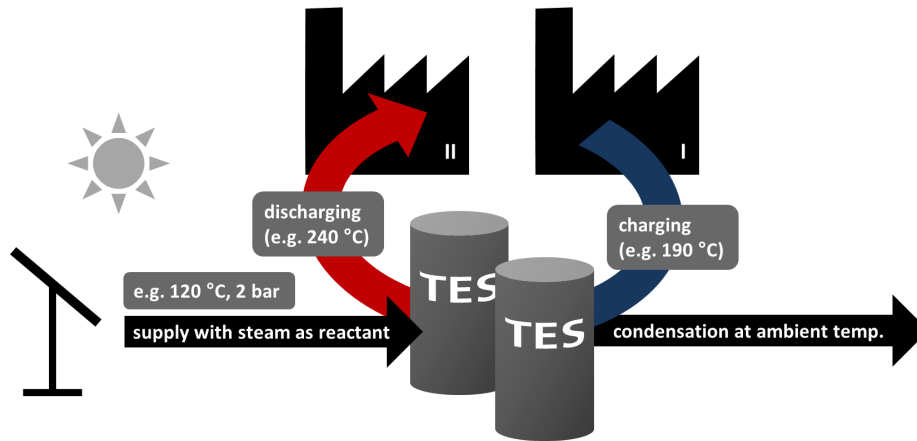


Figure 3.2: Application scenario of thermal upgrading of a process heat flow between two processes. To achieve continuous application, two separate storage units are required. Sensible thermal losses due to switching between the charging and discharging process could be reduced by implementing an internal heat exchanger.

$T_M = 443 \text{ K}$, $T_H = 533 \text{ K}$). The exergy efficiency is 0.79 (Eq. (1.3), $T_0 = 298 \text{ K}$, $T_C = 393 \text{ K}$, $T_M = 463 \text{ K}$, $T_H = 513 \text{ K}$). Note that the exergetic efficiency is higher than in the first example, as a parameter set with lower charging power was selected.

In a similar context of combined TES and thermal upgrade, an interesting approach is pursued by Ströhle et al. for high-temperature TES for power generation in concentrated solar power plants [73]. The authors suggest combining a sensible TES, e.g. rocks, with a thermochemical TES unit, e.g. based on the manganese oxide/oxygen working pair (600 – 1000 °C reaction temperatures). By adjusting the oxygen pressure during discharging the TES, the output temperature of the heat transfer fluid, e.g. air, can be adjusted to temperatures equal to or higher than the TES charging temperature.

3.2.3 Operation as high-temperature heat pump

The last application scenario focuses on the combination of concentrated solar power and waste heat recovery. It corresponds to a chemical heat pump operated at high sink temperatures. Here, the developed storage is used for the continuous upgrade of thermal energy driven by a high-temperature energy reservoir. The high-temperature heat source is required to charge the storage at high temperatures, and thus, high steam pressures (Fig. 3.3). The steam's enthalpy of condensation is supplied to the heat sink. In the discharge cycle, low-temperature waste heat drives the exothermic reaction, with the enthalpy of reaction being supplied to the heat sink, e.g. in form of process steam. The resulting coefficient of performance of this thermochemical heat pump yields $\epsilon = 2.3$ for the given temperatures (Eq. (1.1), $T_C = 363$ K, $T_M = 433$ K, $T_H = 573$ K). Within the scope of the present thesis, the dehydration reaction of monohydrous strontium bromide was not investigated at pressures high enough to enable such a heat pump mode (e.g. 600 kPa). However, this is part of ongoing work.

Although these application scenarios are very basic examples, they illustrate the vast operation range of the presented technology. Most importantly, the scalable TES reactor concept developed in this work can be adapted to all of the discussed generic use cases. Due to the flexibility in the charging and discharging temperatures, the TES device can cope with changing process requirements, e.g. varying synthesis temperatures in a chemical industries batch process, and thus may pay off not only ecologically, but also economically.

3 Discussion and Conclusions

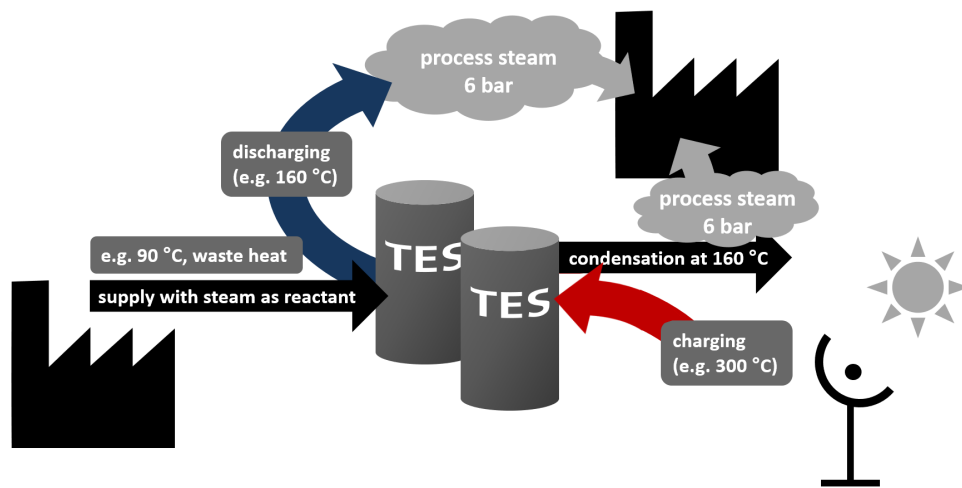


Figure 3.3: Application scenario of a high-temperature heat pump, which provides 160 °C output temperature to a heat sink. Instead of high-temperature heat, electrical energy could be used for the supply of thermal energy for charging the storage.

4

Chapter 4

Summary

In the present work, the fundamental research and development of a thermochemical TES system was conducted, starting from the given thermochemical working pair $\text{SrBr}_2/\text{H}_2\text{O}$, and finally achieving the operation and quantitative understanding of a proof-of-concept storage prototype. The basis for this research was a material screening which had identified the inorganic salt strontium bromide as a potential candidate for thermochemical TES and heat transformation [42]. The investigation at hand covers research results along the development path from the fundamental reactive material characterization and the design of a prototype, up to the experimental and numerical analysis of the operation characteristics of the combined TES and heat transformer:

- The pressure-dependent hydration reaction temperatures of anhydrous strontium bromide to its monohydrous phase and the dehydration temperatures of the latter were experimentally determined. These experiments were conducted in a measurement cell containing approximately 1 kg of the reactive material, and resulted in maximum reaction temperatures up to 260 °C at a steam pressure of 150 kPa.
- Based on thermogravimetric analysis, the pressure and temperature dependent rates of reaction of the endothermic and the exothermic reactions were investigated, and empirical rate models were determined.

4 Summary

- Over a course of 100 hydration/dehydration cycles, chemical cycling stability of the reaction was shown in TGA experiments with 15 mg sample mass. Although the rate of the endothermic reaction shows a slight decrease, this does not affect the usable energy density of the storage material.
- Based on the identified operation range of the $\text{SrBr}_2/\text{H}_2\text{O}$ reaction system (approximately 150 °C – 300 °C) and the expected reaction rates, a storage reactor was developed that is scalable for large industrial applications.
- A lab-scale infrastructure was designed, implemented and commissioned which allows for the investigation of steam-based reaction systems in a pressure range from 1 kPa – 600 kPa, and heat transfer fluid temperatures up to 320 °C.
- With a 1 kW prototype storage module, the experimental proof-of-concept study of combined TES and heat transformation was conducted. Maximum specific thermal powers of approximately 250 W/kg of the anhydrous salt were obtained.
- In the operation range from 180 °C charging temperature to 280 °C discharging temperature, the performance of the storage module was characterized in terms of the thermal powers and the effective thermal upgrade.
- From the comparison of the experimental results with a transient 2D FEM model, the single contributors to the overall performance characteristics of the storage, from the reactive bulk phase to the heat transfer fluid, were quantitatively analyzed.
- Characteristic curves were derived for the design and the operation of the combined TES and heat transformer as it could be used in pilot applications, leading to an outlook on several exemplary application scenarios, which highlight the operation range of the investigated storage system.

Luckily, the end of this thesis is not the end of research on the topic. Subsequent work included the scale-up of the storage prototype to a thermal power of 5 kW [74]. Besides, the investigation of the cycle stability in terms of macroscopic changes in the bulk phase over 1000 charging/discharging cycles is ongoing [74]. Apart from that, future work could include the analysis of the storage integration in application scenarios on system level, e.g. with regard to the overall exergy efficiency. In this context, the extension of the operating scenarios e.g. to sliding pressures and heat transfer fluid temperatures could be investigated for thermal power control, using the developed 2D model.

At least for the author of these lines, this raises the hope that the presented demonstration of combined TES and heat transformation increases the research interest for this technology and – on the long term – can thus contribute to its industrial implementation, and thereby to the increase of the industrial sector's energy efficiency.

Bibliography

- [1] *Renewables 2019. market analysis and forecast from 2019 to 2024*, 2019. [Online]. Available: <https://www.iea.org/reports/renewables-2019> (pages 11, 12).
- [2] M. Papapetrou, G. Kosmadakis, A. Cipollina, U. La Commare, and G. Micale, "Industrial waste heat: Estimation of the technically available resource in the EU per industrial sector, temperature level and country," *Applied Thermal Engineering*, vol. 138, pp. 207–216, 2018. DOI: 10.1016/J.APPLTHERMALENG.2018.04.043 (page 12).
- [3] A. Sharma, V. Tyagi, C. Chen, and D. Buddhi, "Review on thermal energy storage with phase change materials and applications," *Renewable and Sustainable Energy Reviews*, vol. 13, pp. 318–345, 2009. DOI: 10.1016/J.RSER.2007.10.005 (pages 14, 15).
- [4] J. Cot-Gores, A. Castell, and L. F. Cabeza, "Thermochemical energy storage and conversion: A-state-of-the-art review of the experimental research under practical conditions," *Renewable and Sustainable Energy Reviews*, vol. 16, pp. 5207–5224, 2012. DOI: 10.1016/j.rser.2012.04.007 (pages 14, 24).
- [5] J. Sunku Prasad, P. Muthukumar, F. Desai, D. N. Basu, and M. M. Rahman, "A critical review of high-temperature reversible thermochemical energy storage systems," *Applied Energy*, vol. 254, 2019, ISSN: 03062619. DOI: <https://doi.org/10.1016/j.apenergy.2019.113733> (page 14).

Bibliography

- [6] Y. Lin, Y. Jia, G. Alva, and G. Fang, "Review on thermal conductivity enhancement, thermal properties and applications of phase change materials in thermal energy storage," *Renewable and Sustainable Energy Reviews*, vol. 82, pp. 2730–2742, 2018. DOI: 10.1016/J.RSER.2017.10.002 (page 14).
- [7] A. Fopah Lele, K. E. N'Tsoukpoe, T. Osterland, F. Kuznik, and W. K. L. Ruck, "Thermal conductivity measurement of thermochemical storage materials," *Applied Thermal Engineering*, vol. 89, pp. 916–926, 2015, ISSN: 13594311. DOI: 10.1016/j.applthermaleng.2015.06.077 (page 14).
- [8] N. I. Ibrahim, F. A. Al-Sulaiman, S. Rahman, B. S. Yilbas, and A. Z. Sahin, "Heat transfer enhancement of phase change materials for thermal energy storage applications: A critical review," *Renewable and Sustainable Energy Reviews*, vol. 74, pp. 26–50, 2017. DOI: 10.1016/j.rser.2017.01.169 (page 14).
- [9] L. F. Cabeza, C. Sole, A. Castell, E. Oro, and A. Gil, "Review of solar thermal storage techniques and associated heat transfer technologies," *Proceedings of the IEEE*, vol. 100, pp. 525–538, 2012. DOI: 10.1109/JPROC.2011.2157883 (page 14).
- [10] J. Khodadadi and S. Hosseinizadeh, "Nanoparticle-enhanced phase change materials (NEPCM) with great potential for improved thermal energy storage," *International Communications in Heat and Mass Transfer*, vol. 34, pp. 534–543, 2007. DOI: 10.1016/J.ICHEATMASSTRANSFER.2007.02.005 (page 14).
- [11] Y. Tao and Y.-L. He, "A review of phase change material and performance enhancement method for latent heat storage system," *Renewable and Sustainable Energy Reviews*, vol. 93, pp. 245–259, 2018. DOI: 10.1016/J.RSER.2018.05.028 (page 14).
- [12] N. S. Dhaidan and J. M. Khodadadi, "Improved performance of latent heat energy storage systems utilizing high thermal conductivity fins: A review," *Journal of Renewable and Sustainable Energy*, vol. 9, p. 034 103, 2017. DOI: 10.1063/1.4989738 (pages 14, 24).

- [13] Y. E. Milián, A. Gutiérrez, M. Grágeda, and S. Ushak, "A review on encapsulation techniques for inorganic phase change materials and the influence on their thermophysical properties," *Renewable and Sustainable Energy Reviews*, vol. 73, pp. 983–999, 2017. DOI: 10.1016/j.rser.2017.01.159 (page 14).
- [14] J. Tombrink, H. Jockenhöfer, and D. Bauer, "Examination of the heat transfer potential of an active latent heat storage concept," in *Eurotherm Seminar n°112 - Advances in Thermal Energy Storage*, ISBN: 978-84-9144-155-7 (page 14).
- [15] H. Pointner and W.-D. Steinmann, "Experimental demonstration of an active latent heat storage concept," *Applied Energy*, vol. 168, pp. 661–671, 2016, ISSN: 03062619. DOI: 10.1016/j.apenergy.2016.01.113 (page 14).
- [16] N. C. Preisner and M. Linder, "A moving bed reactor for thermochemical energy storage based on metal oxides," *Energies*, vol. 13, no. 5, 2020, ISSN: 1996-1073. DOI: 10.3390/en13051232 (page 14).
- [17] M. Schmidt, M. Gollsch, F. Giger, M. Grün, and M. Linder, "Development of a moving bed pilot plant for thermochemical energy storage with CaO/Ca(OH)₂," *AIP Conference Proceedings*, vol. 1734, no. 1, p. 050041, 2016. DOI: <https://doi.org/10.1063/1.4949139> (page 14).
- [18] A. Cosquillo Mejia, S. Afflerbach, M. Linder, and M. Schmidt, "Experimental analysis of encapsulated CaO/Ca(OH)₂ granules as thermochemical storage in a novel moving bed reactor," *Applied Thermal Engineering*, vol. 169, 2020, ISSN: 13594311. DOI: 10.1016/j.applthermaleng.2020.114961 (page 14).
- [19] L. Farcot, N. Le Pierrès, and J.-F. Fourmigué, "Experimental investigation of a moving-bed heat storage thermochemical reactor with SrBr₂/H₂O couple," *Journal of Energy Storage*, vol. 26, 2019, ISSN: 2352152X. DOI: 10.1016/j.est.2019.101009 (page 14).

Bibliography

- [20] M. Angerer, M. Becker, S. Härzschel, K. Kröper, S. Gleis, A. Vandersickel, and H. Spliethoff, "Design of a MW-scale thermo-chemical energy storage reactor," *Energy Reports*, vol. 4, pp. 507–519, 2018, ISSN: 23524847. DOI: 10.1016/j.egyrs.2018.07.005 (page 14).
- [21] D. Hebecker, *Wärmetransformation*, 1995 (page 16).
- [22] P. Bittrich and D. Hebecker, "Classification and evaluation of heat transformation processes," *International Journal of Thermal Sciences*, vol. 38, pp. 465–474, 1999. DOI: 10.1016/S1290-0729(99)80019-2 (page 16).
- [23] Y. Yu, P. Zhang, J. Wu, and R. Wang, "Energy upgrading by solid–gas reaction heat transformer: A critical review," *Renewable and Sustainable Energy Reviews*, vol. 12, pp. 1302–1324, 2008. DOI: 10.1016/j.rser.2007.01.010 (pages 17, 19, 21).
- [24] M. Richter, M. Bouché, and M. Linder, "Heat transformation based on $\text{CaCl}_2/\text{H}_2\text{O}$ – Part A: Closed operation principle," *Applied Thermal Engineering*, vol. 102, pp. 615–621, 2016. DOI: 10.1016/j.applthermaleng.2016.03.076 (pages 17, 20, 23–25, 28).
- [25] A. Thess, *Das Entropieprinzip: Thermodynamik für Unzufriedene*. De Gruyter Oldenbourg, 2014, 2. Auflage, ISBN: 978-3486760453 (page 19).
- [26] G. Bisio, "Thermodynamic analysis of the main devices for thermal energy upgrading," *Energy Conversion and Management*, vol. 39, pp. 229–242, 1998. DOI: 10.1016/S0196-8904(96)00223-3 (page 19).
- [27] W. Wongsuwan, S. Kumar, P. Neveu, and F. Meunier, "A review of chemical heat pump technology and applications," *Applied Thermal Engineering*, vol. 21, pp. 1489–1519, 2001, ISSN: 6625245410. DOI: 10.1016/S1359-4311(01)00022-9 (page 19).
- [28] F. S. Yang, G. X. Wang, Z. X. Zhang, and V. Rudolph, "Investigation on the influences of heat transfer enhancement measures in a thermally driven metal hydride heat pump," *International Journal of Hydrogen Energy*, vol. 35,

- no. 18, pp. 9725–9735, 2010, ISSN: 03603199. DOI: 10.1016/j.ijhydene.2010.06.110 (page 19).
- [29] E. Willers and M. Groll, “Two-stage metal hydride heat transformer,” *International Journal of Hydrogen Energy*, vol. 24, pp. 269–276, 1999. DOI: 10.1016/S0360-3199(98)00058-5 (page 19).
- [30] W. G. Haije, J. B. Veldhuis, S. F. Smeding, and R. J. Grisel, “Solid/vapour sorption heat transformer: Design and performance,” *Applied Thermal Engineering*, vol. 27, pp. 1371–1376, 2007. DOI: 10.1016/j.applthermaleng.2006.10.022 (pages 20, 24).
- [31] M. van der Pal and R. E. Critoph, “Performance of CaCl₂-reactor for application in ammonia-salt based thermal transformers,” *Applied Thermal Engineering*, vol. 126, pp. 518–524, 2017. DOI: 10.1016/j.applthermaleng.2017.07.086 (page 20).
- [32] S. Spoelstra, W. G. Haije, and J. W. Dijkstra, “Techno-economic feasibility of high-temperature high-lift chemical heat pumps for upgrading industrial waste heat,” *Applied Thermal Engineering*, vol. 22, pp. 1619–1630, 2002. DOI: 10.1016/S1359-4311(02)00077-7 (page 20).
- [33] S. Wu, T. Li, T. Yan, and R. Wang, “Experimental investigation on a novel solid-gas thermochemical sorption heat transformer for energy upgrade with a large temperature lift,” *Energy Conversion and Management*, vol. 148, pp. 330–338, 2017. DOI: 10.1016/J.ENCONMAN.2017.05.041 (page 20).
- [34] A. Lubis, N. Giannetti, S. Yamaguchi, K. Saito, and N. Inoue, “Experimental performance of a double-lift absorption heat transformer for manufacturing-process steam generation,” *Energy Conversion and Management*, vol. 148, pp. 267–278, 2017. DOI: 10.1016/J.ENCONMAN.2017.05.074 (page 21).
- [35] P. Donkers, L. Sögütöglu, H. Huinink, H. Fischer, and O. Adan, “A review of salt hydrates for seasonal heat storage in domestic applications,” *Applied Energy*, vol. 199, pp. 45–68, 2017. DOI: 10.1016/J.APENERGY.2017.04.080 (page 21).

Bibliography

- [36] A. Fopah Lele, F. Kuznik, O. Opel, and W. K. Ruck, "Performance analysis of a thermochemical based heat storage as an addition to cogeneration systems," *Energy Conversion and Management*, vol. 106, pp. 1327–1344, 2015. DOI: 10.1016/j.enconman.2015.10.068 (page 21).
- [37] A. Fopah-Lele and J. G. Tamba, "A review on the use of $\text{SrBr}_2 \cdot 6\text{H}_2\text{O}$ as a potential material for low temperature energy storage systems and building applications," *Solar Energy Materials and Solar Cells*, vol. 164, pp. 175–187, 2017. DOI: 10.1016/J.SOLMAT.2017.02.018 (pages 21, 24).
- [38] H. Lahmidi, S. Mauran, and V. Goetz, "Definition, test and simulation of a thermochemical storage process adapted to solar thermal systems," *Solar Energy*, vol. 80, pp. 883–893, 2006, ISSN: 0038-092X. DOI: 10.1016/j.solener.2005.01.014 (page 21).
- [39] B. Michel, N. Mazet, and P. Neveu, "Experimental investigation of an innovative thermochemical process operating with a hydrate salt and moist air for thermal storage of solar energy: Global performance," *Applied Energy*, vol. 129, pp. 177–186, 2014. DOI: 10.1016/j.apenergy.2014.04.073 (pages 21, 24).
- [40] L. Glasser, "Thermodynamics of inorganic hydration and of humidity control, with an extensive database of salt hydrate pairs," *Journal of Chemical and Engineering Data*, vol. 59, pp. 526–530, 2014. DOI: 10.1021/je401077x (page 21).
- [41] S. Afflerbach and R. Trettin, "A systematic screening approach for new materials for thermochemical energy storage and conversion based on the Strunz mineral classification system," *Thermochimica Acta*, vol. 674, pp. 82–94, 2019. DOI: 10.1016/J.TCA.2019.02.010 (page 21).
- [42] M. Richter, E.-M. Habermann, E. Siebecke, and M. Linder, "A systematic screening of salt hydrates as materials for a thermochemical heat transformer," *Thermochimica Acta*, vol. 659, pp. 136–150, 2018. DOI: 10.1016/j.tca.2017.06.011 (pages 21, 22, 27, 94, 103).

- [43] J. Andersson, M. Azoulay, and J. de Pablo, "Chemical heat pumping — a rapid experimental procedure for investigating the suitability of salt hydrates under dynamic conditions," *International Journal of Energy Research*, vol. 12, pp. 137–145, 1988. DOI: 10.1002/er.4440120114 (page 22).
- [44] M. Molenda, J. Stengler, M. Linder, and A. Wörner, "Reversible hydration behavior of CaCl_2 at high H_2O partial pressures for thermochemical energy storage," *Thermochimica Acta*, vol. 560, pp. 76–81, 2013. DOI: <https://doi.org/10.1016/j.tca.2013.03.020> (page 22).
- [45] L.-C. Sögütöglu, M. Steiger, J. Houben, D. Biemans, H. R. Fischer, P. Donkers, H. Huinink, and O. C. G. Adan, "Understanding the hydration process of salts: The impact of a nucleation barrier," *Crystal Growth and Design*, vol. 19, no. 4, pp. 2279–2288, 2019, ISSN: 1528-7483 1528-7505. DOI: 10.1021/acs.cgd.8b01908 (page 22).
- [46] M. Wokon, T. Block, S. Nicolai, M. Linder, and M. Schmücker, "Thermodynamic and kinetic investigation of a technical grade manganese-iron binary oxide for thermochemical energy storage," *Solar Energy*, vol. 153, pp. 471–485, 2017. DOI: 10.1016/J.SOLENER.2017.05.045 (page 22).
- [47] M. M. Farid, A. M. Khudhair, S. A. K. Razack, and S. Al-Hallaj, "A review on phase change energy storage: Materials and applications," *Energy Conversion and Management*, vol. 45, no. 9-10, pp. 1597–1615, 2004, ISSN: 01968904. DOI: 10.1016/j.enconman.2003.09.015 (page 22).
- [48] R. A. Taylor, N. Tsafnat, and A. Washer, "Experimental characterisation of sub-cooling in hydrated salt phase change materials," *Applied Thermal Engineering*, vol. 93, pp. 935–938, 2016, ISSN: 13594311. DOI: 10.1016/j.applthermaleng.2015.10.032 (page 22).
- [49] Y. Kato, Y. Sasaki, and Y. Yoshizawa, "Magnesium oxide/water chemical heat pump to enhance energy utilization of a cogeneration system," *Energy*, vol. 30, no. 11-12, pp. 2144–2155, 2005, ISSN: 03605442. DOI: 10.1016/j.energy.2004.08.019 (page 22).

Bibliography

- [50] P. D'Ans, E. Courbon, M. Frère, G. Descy, T. Segato, and M. Degrez, "Severe corrosion of steel and copper by strontium bromide in thermochemical heat storage reactors," *Corrosion Science*, 2018. DOI: 10.1016/j.corsci.2018.04.020 (page 22).
- [51] "Aufwertung von Abwärme durch Einsatz Thermochemischer Speicher-materialien (TheSan). Abschlussbericht zum Teilvorhaben der Evonik Creavis GmbH: Anwendungskonzepte für industrielle Batchprozesse und Untersuchung von Nachhaltigkeitsaspekten der Reaktionsmaterialien," Report, 2018. DOI: <https://doi.org/10.2314/KXP:1678987441> (page 22).
- [52] D. Gilles, T. Segato, E. Courbon, M. Degrez, and P. D'Ans, "Affordable process for the production of strontium bromide used in low grade heat recovery applications," *Procedia CIRP*, vol. 69, pp. 383–388, 2018. DOI: 10.1016/j.procir.2017.11.056 (page 23).
- [53] C. Knoll, D. Müller, W. Artner, J. M. Welch, A. Werner, M. Harasek, and P. Weinberger, "Probing cycle stability and reversibility in thermochemical energy storage – $\text{CaC}_2\text{O}_4 \cdot \text{H}_2\text{O}$ as perfect match?" *Applied Energy*, vol. 187, pp. 1–9, 2017. DOI: 10.1016/j.apenergy.2016.11.053 (page 23).
- [54] S. Afflerbach, S. Sharma, and R. Trettin, "Synthesis, reversibility and mechanism of the dehydration of monoclinic $\text{CaZn}_2(\text{PO}_4)_2 \cdot 2\text{H}_2\text{O}$," *Journal of Solid State Chemistry*, vol. 265, pp. 274–284, 2018. DOI: 10.1016/J.JSSC.2018.06.022 (page 23).
- [55] Y. I. Aristov, "Challenging offers of material science for adsorption heat transformation: A review," *Applied Thermal Engineering*, vol. 50, pp. 1610–1618, 2013. DOI: 10.1016/J.APPLTHERMALENG.2011.09.003 (page 23).
- [56] A. Solé, I. Martorell, and L. F. Cabeza, "State of the art on gas–solid thermochemical energy storage systems and reactors for building applications," *Renewable and Sustainable Energy Reviews*, vol. 47, pp. 386–398, 2015. DOI: 10.1016/j.rser.2015.03.077 (page 23).

- [57] A. H. Abedin and M. Rosen, "Closed and open thermochemical energy storage: Energy- and exergy-based comparisons," *Energy*, vol. 41, pp. 83–92, 2012, ISSN: 0360-5442. DOI: 10.1016/j.energy.2011.06.034 (page 23).
- [58] M. Bouché, M. Richter, and M. Linder, "Heat transformation based on CaCl₂/H₂O – Part B: Open operation principle," *Applied Thermal Engineering*, vol. 102, pp. 641–647, 2016. DOI: 10.1016/J.APPLTHERMALENG.2016.03.102 (page 23).
- [59] M. Dieterich, I. Bürger, and M. Linder, "Open and closed metal hydride system for high thermal power applications: Preheating vehicle components," *International Journal of Hydrogen Energy*, vol. 42, no. 16, pp. 11469–11481, 2017, ISSN: 03603199. DOI: 10.1016/j.ijhydene.2017.03.024 (page 24).
- [60] C. Weckerle, M. Nasri, R. Hegner, I. Bürger, and M. Linder, "A metal hydride air-conditioning system for fuel cell vehicles – functional demonstration," *Applied Energy*, vol. 259, 2020, ISSN: 03062619. DOI: 10.1016/j.apenergy.2019.114187 (page 24).
- [61] T. Esaki, M. Yasuda, and N. Kobayashi, "Experimental evaluation of the heat output/input and coefficient of performance characteristics of a chemical heat pump in the heat upgrading cycle of CaCl₂ hydration," *Energy Conversion and Management*, vol. 150, pp. 365–374, 2017. DOI: 10.1016/J.ENCONMAN.2017.08.013 (page 24).
- [62] A. M. Abdulateef, S. Mat, J. Abdulateef, K. Sopian, and A. A. Al-Abidi, "Geometric and design parameters of fins employed for enhancing thermal energy storage systems: A review," *Renewable and Sustainable Energy Reviews*, vol. 82, pp. 1620–1635, 2018. DOI: 10.1016/J.RSER.2017.07.009 (page 24).
- [63] S. Riahi, W. Y. Saman, F. Bruno, M. Belusko, and N. Tay, "Performance comparison of latent heat storage systems comprising plate fins with different shell and tube configurations," *Applied Energy*, vol. 212, pp. 1095–1106, 2018. DOI: 10.1016/J.APENERGY.2017.12.109 (page 24).

Bibliography

- [64] S. Wu, T. Li, T. Yan, and R. Wang, "Advanced thermochemical resorption heat transformer for high-efficiency energy storage and heat transformation," *Energy*, vol. 175, pp. 1222–1233, 2019. DOI: 10.1016/J.ENERGY.2019.03.159 (page 24).
- [65] A. Fopah Lele, F. Kuznik, H. U. Rammelberg, T. Schmidt, and W. K. Ruck, "Thermal decomposition kinetic of salt hydrates for heat storage systems," *Applied Energy*, vol. 154, pp. 447–458, 2015. DOI: 10.1016/j.apenergy.2015.02.011 (page 24).
- [66] Z. Pan and C. Zhao, "Gas–solid thermochemical heat storage reactors for high-temperature applications," *Energy*, vol. 130, pp. 155–173, 2017. DOI: 10.1016/J.ENERGY.2017.04.102 (page 24).
- [67] M. Schmidt, C. Szczukowski, C. Roßkopf, M. Linder, and A. Wörner, "Experimental results of a 10 kw high temperature thermochemical storage reactor based on calcium hydroxide," *Applied Thermal Engineering*, vol. 62, pp. 553–559, 2014. DOI: 10.1016/j.applthermaleng.2013.09.020 (page 24).
- [68] M. Molenda, "Chemische Speicherung und Transformation thermischer Energie mit Calciumchlorid und Wasserdampf," Thesis, 2015 (page 25).
- [69] M. Schmidt and M. Linder, "Power generation based on the $\text{Ca}(\text{OH})_2/\text{CaO}$ thermochemical storage system – experimental investigation of discharge operation modes in lab scale and corresponding conceptual process design," *Applied Energy*, vol. 203, pp. 594–607, 2017. DOI: 10.1016/J.APENERGY.2017.06.063 (page 94).
- [70] M. Johnson, J. Vogel, M. Hempel, B. Hachmann, and A. Dengel, "Design of high temperature thermal energy storage for high power levels," *Sustainable Cities and Society*, vol. 35, pp. 758–763, 2017. DOI: 10.1016/J.SCS.2017.09.007 (page 95).

- [71] J. Vogel, M. Keller, and M. Johnson, "Numerical modeling of large-scale finned tube latent thermal energy storage systems," *Journal of Energy Storage*, vol. 29, 2020, ISSN: 2352152X. DOI: 10.1016/j.est.2020.101389 (page 95).
- [72] M. A. Rosen and I. Dincer, "A study of industrial steam process heating through exergy analysis," *International Journal of Energy Research*, vol. 28, pp. 917–930, 2004. DOI: 10.1002/er.1005 (page 97).
- [73] S. Ströhle, A. Haselbacher, Z. R. Jovanovic, and A. Steinfeld, "Upgrading sensible-heat storage with a thermochemical storage section operated at variable pressure: An effective way toward active control of the heat-transfer fluid outflow temperature," *Applied Energy*, vol. 196, pp. 51–61, 2017, ISSN: 03062619. DOI: 10.1016/j.apenergy.2017.03.125 (page 100).
- [74] "Aufwertung von Abwärme durch Einsatz Thermochemischer Speicher-materialien (TheSan): Abschlussbericht," Report, 2020. DOI: <https://doi.org/10.2314/KXP:1737565803> (page 105).